NAUSIVIOS CHORA

A Journal in Naval Sciences and Technology

PART C:
NATURAL SCIENCES AND MATHEMATICS

Volume 4/2012

ΝΑΥΣΙΒΙΟΣ ΧΩΡΑ

Περιοδική Έκδοση Ναυτικών Επιστημών

ΜΕΡΟΣ C:
ΦΥΣΙΚΕΣ ΕΠΙΣΤΗΜΕΣ ΚΑΙ ΜΑΘΗΜΑΤΙΚΑ

Τεύχος 4/2012

«ΝΑΥΣΙΒΙΟΣ ΧΩΡΑ» 2012
Περιοδική Έκδοση Ναυτικών Επιστημών
Σχολή Ναυτικών Δοκίμων,
Τέρμα Χατζηκυριακού, Χατζηκυριάκειο,
Πειραιάς 18539, Ελλάδα
http://nausivios.snd.edu.gr
ΤΗΛ+302104581382/FAX+302104581604
nausivios@snd.edu.gr

"NAUSIVIOS CHORA" 2012
Journal in Naval Sciences and Technology
Hellenic Naval Academy
Hatzikiriakio, 18539 Piraeus, Greece
http://nausivios.snd.edu.gr
Tel +302104581382/fax +302104581604
nausivios@snd.edu.gr

ISSN: 1791-4469

TABLE OF CONTENTS

Χαιρετισμός Διοικητή Σχολής Ναυτικών Δοκίμων

Καλωσορίζουμε το 4ο τεύχος της «Ναυσιβίου Χώρας» που αναδεικνύει το έργο που επιτελείται στη ΣΝΔ όσον αφορά τις Ναυτικές Επιστήμες.

Σήμερα, σε μια εποχή οικονομικών και κοινωνικών προβλημάτων η έκδοση της «Ναυσιβίου Χώρας» σηματοδοτεί την προσπάθεια των καθηγητών της ΣΝΔ και άλλων εκπαιδευτικών ιδρυμάτων να δημιουργήσουν με το έργο τους θετικές προσδοκίες και εμπλουτισμό γνώσεων τόσο στους φοιτούντες στα Ανώτατα Στρατιωτικά Εκπαιδευτικά Ιδρύματα όσο και σε όλες τις Πανεπιστημιακές Σχολές που ασχολούνται με τον κλάδο των Ναυτικών Επιστημών. Στόχος τους είναι να ενημερώσουν και να προβάλλουν νέες μεθόδους και εξελιγμένες τεχνικές βασισμένες σε προσωπικές έρευνες και αναλύσεις, με αποτέλεσμα την καλύτερη εκπαίδευση και επιμόρφωση των νέων επιστημόνων.

Ως εκ τούτου, χαιρετίζω την τέταρτη έκδοση της «Ναυσιβίου Χώρας» με την ευχή να αποτελέσει ένα νέο κίνητρο για την εξέλιξη και την πρόοδο της Ναυτικής Επιστήμης τόσο στην Ελλάδα όσο και στο εξωτερικό.

Υποναύαρχος Ι. Μαΐστρος ΠΝ, Διοικητής ΣΝΔ

Welcome Address by the Commandant of the Hellenic Naval Academy

We welcome the 4th edition of the “Nausivios Chora” which illustrates the work of the Hellenic Naval Academy concerning the Naval Sciences.

Nowadays, at a time of economic and social problems, the edition of the “Nausivios Chora” underlines the effort of the staff of the Hellenic Navy Academy and other Institutes to create with their work positive expectations and knowledge enrichment both to the students of the Higher Military Educational Institutions and to other Universities that are engaged with Naval Sciences. They are targeting to inform and display new methods and sophisticated techniques based on personal research and analysis, in order to educate and train the new scientists.

Therefore, I wellcome the fourth edition of the “Nausivios Chora” with the wish for it to be a motive for the development and progress of the Naval Science not only in Greece but also abroad.

Rear-Admiral I. Maistros HN, Commandant of the Hellenic Naval Academy

International Advisory Committee

Editorial Board

Editor's Note

"Nausivios Chora" is a scientific journal published since 2006 by the Hellenic Naval Academy, the Institution that provides academic and professional training to the future officers of the Hellenic Navy. The faculty members of the Hellenic Naval Academy are devoted to the promotion of research and education on a broad range of scientific disciplines.

"Nausivios Chora" is a biannual, peer-reviewed, open access journal that publishes original articles in areas of scientific research and applications directly or indirectly related to the naval sciences and technology. The scope of the Journal is to provide a basis for the communication and dissemination of scientific results obtained in Hellenic or International academic and research institutions that may present a relevance to the sea element.

"Nausivios Chora" hosts articles belonging to various scientific disciplines and is divided in five parts, namely *Mechanical and Marine Engineering*, *Electrical Engineering and Computer Science*, *Natural Sciences and Mathematics*, *Humanities and Political Sciences* and *Naval Operations*. The present 2012 Edition Issue contains 24 articles.

The International Advisory Committee members and the Body of Reviewers, all acknowledged experts in their field of interests, cover a wide range of scientific disciplines ensuring the integrity of the peer-review process and the academic excellence of the published articles in a way that best represents the aims and scope of the Journal.

Prof Dr Elias Ar Yfantis
Editor in chief

Acknowledgments

I wish to express my special thanks to Dr Antonis Tsapalis for his excellent work as the administrator of the “Nausivios Chora” website.
Special thanks to Dr Evangelia Karagianni for her creative work on the “Nausivios Chora” 2012 Edition.

E.Ar.Yfantis

PART C:

NATURAL SCIENCES AND MATHEMATICS

Μέθοδοι Μετασχηματισμού του Ελλειψοειδούς εκ Περιστροφής σε Σφαιρική Επιφάνεια

Αθανάσιος Παλληκάρης

Σχολή Ναυτικών Δοκίμων, Εργαστήριο Ναυτιλίας και Θαλλασίων Επιστημών, Λεωφόρος Χατζηκυριακού, Χατζηκυριάκειο, Πειραιάς, ΤΚ 18539, palikaris@snd.edu.gr

Περίληψη. Στην παρούσα μελέτη παρουσιάζονται και αξιολογούνται μέθοδοι μετασχηματισμού του ελλειψοειδούς εκ περιστροφής σε σφαιρική επιφάνεια. Παρουσιάζονται συναρτήσεις για τον ευθύ μετασχηματισμό «ελλειψοειδές δε σφαίρα» και για τον αντίστροφο μετασχηματισμό «σφαίρα σε ελλειψοειδές» για τις επόμενες τέσσερις περιπτώσεις: μετασχηματισμός σε «σφαίρα συμμορφίας» χωρίς γωνιακές παραμορφώσεις, σε «ισοδύναμη σφαίρα» χωρίς επιφανειακές παραμορφώσεις, σε «ισαπέχουσα στη διεύθυνση των μεσημβρινών σφαίρα» και σε «ισαπέχουσα στη διεύθυνση ενός παραλλήλου πλάτους σφαίρα». Η αξιολόγηση των μεθόδων μετασχηματισμού βασίστηκε στον υπολογισμό και στην ανάλυση της κατανομής των γραμμικών, επιφανειακών και γωνιακών παραμορφώσεων. Τα αποτελέσματα της αξιολόγησης μπορούν να αξιοποιηθούν στην επιλογή της καταλληλότερης μεθόδου για την χαρτογραφική απεικόνιση ολόκληρης, ή τμήματος της επιφάνειας της γης σύμφωνα με τις κατά περίπτωση επιθυμητές ιδιότητες, όπως μηδενισμός των γωνιακών ή των επιφανειακών παραμορφώσεων, ανάλογα με τον σκοπό για τον οποίο προορίζεται η χαρτογραφική απεικόνιση.

Λέξεις-Κλειδιά: χαρτογραφικές προβολές, παραμορφώσεις, διπλή απεικόνιση ελλειψοειδούς

Methods of Transforming the Ellipsoid of Revolution onto the Surface of a Sphere

Athanasios Pallikaris

Hellenic Naval Academy, Sea Sciences and Navigation Laboratory, Terma Hatzikyriakou Ave, Pireas Greece, TK 18539, palikaris@snd.edu.gr

Abstract. Methods of transformation of the surface of the ellipsoid of revolution onto the surface of a sphere are presented and evaluated. The methods can be used for the double projection of the ellipsoid onto a plane (ellipsoid to sphere, then sphere to plane) by the employment of map projections for which map transformation functions exist only for the sphere. Direct and inverse map transformation functions are presented and evaluated for four cases: transformation onto a “conformal sphere” without angle distortion, onto an “equivalent sphere” without area distortion, onto an “equidistant along the meridians sphere” and onto an “equidistant along a certain parallel sphere”. The assessment of the transformations has been conducted by numerical tests based on the calculation and analysis of the linear, angular and area distortions for each transformation.

Keywords: map projections, map distortion, double projection, ellipsoid

ΕΙΣΑΓΩΓΗ - ΜΕΘΟΔΟΙ ΑΠΕΙΚΟΝΙΣΗΣ ΤΗΣ ΕΠΙΦΑΝΕΙΑΣ ΤΟΥ ΕΛΛΕΙΨΟΕΙΔΟΥΣ ΕΚ ΠΕΡΙΣΤΡΟΦΗΣ ΣΕ ΕΠΙΠΕΔΟ

Η απεικόνιση της επιφάνειας του Ελλειψοειδούς εκ Περιστροφής (ΕΕΠ) σε επίπεδο πραγματοποιείται συνήθως με χρήση των συναρτήσεων f_1 και f_2 των (1) και (2), με τις οποίες πραγματοποιείται ο μετασχηματισμός των ελλειπτικών γεωδαιτικών συντεταγμένων (φ_i, λ_i) των σημείων της επιφάνειας του ΕΕΠ στις καρτεσιανές συντεταγμένες (x_i, y_i) του επιπέδου απεικόνισης (Σχ. 1). Ο μετασχηματισμός αυτός $[(\varphi_i,\lambda_i)\rightarrow(x_i,y_i)]$ αποτελεί το ευθύ πρόβλημα της αναλυτικής χαρτογραφίας, το οποίο αποτελεί βασικό εργαλείο της επιστημονικής έρευνας τόσο για την ανάλυση και αξιολόγηση των γνωστών χαρτογραφικών απεικονίσεων όσο για τη δημιουργία νέων χαρτογραφικών απεικονίσεων (χαρτογραφικών προβολών) ολόκληρης, ή μέρους της επιφάνειας της γης.

$$x_i = f_1(\varphi_i,\lambda_i) \quad (1)$$

$$y_i = f_2(\varphi_i,\lambda_i) \quad (2)$$

Ο αντίστροφος μετασχηματισμός των συντεταγμένων (x_i, y_i), των σημείων του επιπέδου απεικόνισης στις ελλειπτικές γεωδαιτικές συντεταγμένες (φ_i, λ_i) των αντίστοιχων σημείων της επιφάνειας του ΕΕΠ $[(x_i,y_i)\rightarrow(\varphi_i,\lambda_i)]$ αποτελεί το αντίστροφο πρόβλημα της αναλυτικής χαρτογραφίας, στο οποίο χρησιμοποιούνται οι συναρτήσεις του αντίστροφου μετασχηματισμού g_1 και g_2 των (3) και (4).

$$\varphi_i = g_1(x_i, y_i) \quad (3)$$

$$\lambda_i = g_2(x_i, y_i) \quad (4)$$

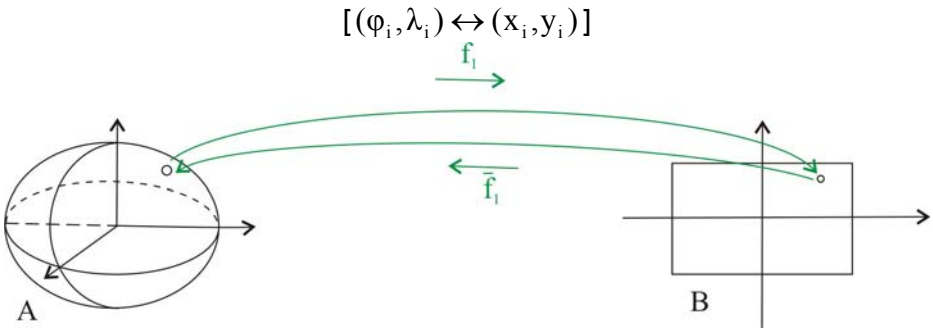

Σχήμα 1. Μετασχηματισμός της επιφάνειας του ΕΕΠ σε επίπεδο

Σε ορισμένες χαρτογραφικές απεικονίσεις συνηθίζεται να χρησιμοποιούνται οι απλούστερες συναρτήσεις χαρτογραφικού μετασχηματισμού της σφαίρας. Η απλοποίηση αυτή έχει χρησιμοποιηθεί εκτενώς σε παραδοσιακούς έντυπους γεωγραφικούς άτλαντες για την απεικόνιση γεωγραφικών περιοχών πολύ μεγάλης έκτασης, οι οποίες καλύπτουν ένα ημισφαίριο ή και ολόκληρη την υδρόγειο σε πολύ μικρές κλίμακες, για τις οποίες δεν παρατηρούνται αξιόλογες διαφορές με τις αντίστοιχες απεικονίσεις του ΕΕΠ. Για τις σύγχρονες εφαρμογές σε περιβάλλον Συστήματος Γεωγραφικών Πληροφοριών (GIS), στις οποίες λόγω της δυνατότητας δυναμικής αλλαγής της κλίμακας απεικόνισης απαιτείται μεγαλύτερη ακρίβεια απεικόνισης, ο μετασχηματισμός της επιφάνειας του ΕΕΠ σε επίπεδο είναι δυνατό να υλοποιηθεί με την εκτέλεση ενός ενδιάμεσου μετασχηματισμού της επιφάνειας του ΕΕΠ σε μια βοηθητική σφαίρα και στη συνέχεια με την απεικόνιση της σφαίρας σε επίπεδο (Σχ. 2) [Παλληκάρης 2010].

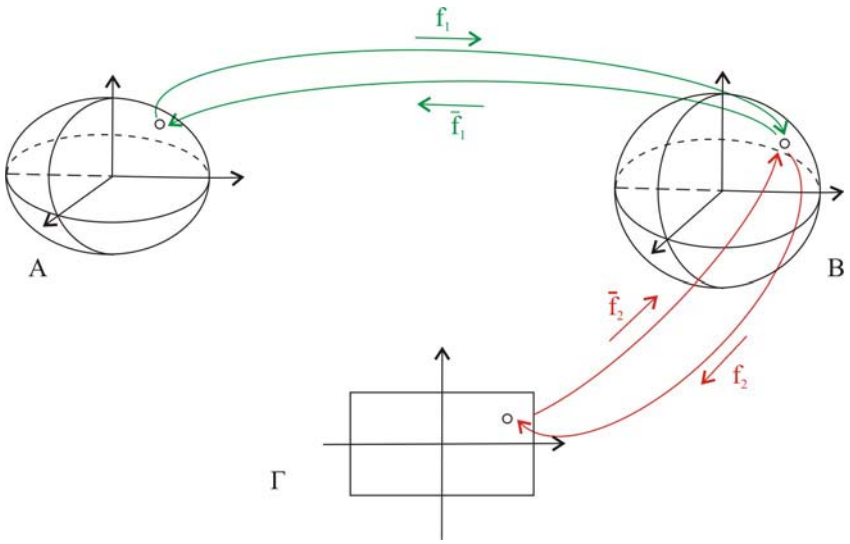

Σχήμα 2. Μετασχηματισμός της επιφάνειας του ΕΕΠ σε επίπεδο με ενδιάμεση απεικόνιση σε βοηθητική σφαίρα

Κατά τον ενδιάμεσο μετασχηματισμό της επιφάνειας του ΕΕΠ σε σφαίρα και ανάλογα με τις απαιτήσεις της εξεταζόμενης εφαρμογής, είναι δυνατό να εξασφαλιστεί η διατήρηση κάποιας βασικής ιδιότητας, όπως: μηδενισμός των γωνιακών παραμορφώσεων, μηδενισμός των επιφανειακών (εμβαδικών) παραμορφώσεων, μηδενισμός των γραμμικών παραμορφώσεων σε μία καθορισμένη διεύθυνση. Με τον τρόπο αυτό είναι δυνατό να προκύψουν διάφορες ενδιάμεσες σφαίρες με διαφορετικά χαρακτηριστικά εκάστη, όπως:

- Σφαίρα συμμορφίας, η οποία προκύπτει από το μετασχηματισμός της επιφάνειας του ελλειψοειδούς χωρίς γωνιακές παραμορφώσεις.
- Ισοδύναμη σφαίρα, η οποία προκύπτει από το μετασχηματισμός της επιφάνειας του ελλειψοειδούς χωρίς επιφανειακές (εμβαδικές) παραμορφώσεις, δηλαδή το εμβαδόν της επιφάνειας απεικόνισης (ισοδύναμης σφαίρας) είναι ‘ίσο με το εμβαδόν της επιφάνειας αναφοράς (ελλειψοειδούς)
- Ισαπέχουσα στη διεύθυνση των μεσημβρινών σφαίρα, η οποία προκύπτει από το μετασχηματισμός της επιφάνειας του ελλειψοειδούς χωρίς γραμμικές παραμορφώσεις στη διεύθυνση των μεσημβρινών
- Ισαπέχουσα στη διεύθυνση των παραλλήλων σφαίρα, η οποία προκύπτει από το μετασχηματισμός της επιφάνειας του ελλειψοειδούς χωρίς γραμμικές παραμορφώσεις στη διεύθυνση των παραλλήλων

Στις προαναφερθείσες μεθόδους μετασχηματισμού της επιφάνειας του ΕΕΠ σε σφαίρα, η αντιστοιχία των ελλειπτικών γεωδαιτικών συντεταγμένων (φ, λ) ενός σημείου της επιφάνειας του ΕΕΠ και των σφαιρικών συντεταγμένων (φ΄, λ΄) του σημείου αυτού στη σφαίρα, δίνεται από τις (4) και (5). Ο αντίστροφος μετασχηματισμός των γεωγραφικών συντεταγμένων (φ΄, λ΄) ενός σημείου της επιφάνειας της βοηθητικής σφαίρας στις αντίστοιχες γεωδαιτικές συντεταγμένες (φ, λ) στην επιφάνεια του ΕΕΠ πραγματοποιείται με τις (5) και (6).

$$\varphi' = \varphi - A_2 \sin 2\varphi - A_4 \sin 4\varphi - A_6 \sin 6\varphi - A_8 \sin 8\varphi \quad (4)$$

$$\lambda = \lambda' \quad (5)$$

$$\varphi = \varphi' + B_2 \sin 2\varphi' + B_4 \sin 4\varphi' + B_6 \sin 6\varphi' + B_8 \sin 8\varphi' \quad (6)$$

όπου:

φ, λ: είναι το γεωδαιτικό πλάτος και το γεωδαιτικό μήκος ενός σημείου στην επιφάνεια του ΕΕΠ

φ΄, λ΄: είναι το (σφαιρικό) γεωγραφικό πλάτος και το (σφαιρικό) γεωγραφικό μήκος ενός σημείου στην επιφάνεια της σφαίρας

Οι τιμές των συντελεστών A_2, A_4, A_6, A_8, B_2, B_4, B_6 και B_8 εξαρτώνται από την χρησιμοποιούμενη βοηθητική σφαίρα (σφαίρα συμμορφίας, ισοδύναμη σφαίρα, ισαπέχουσα σφαίρα).

ΠΑΡΑΜΟΡΦΩΣΕΙΣ ΜΕΤΑΣΧΗΜΑΤΙΣΜΟΥ ΕΠΙΦΑΝΕΙΩΝ

Βασικές έννοιες και ορισμοί

Σύμφωνα με τις βασικές αρχές της θεωρίας των παραμορφώσεων των επιφανειών της διαφορικής γεωμετρίας, όπως αυτές εφαρμόζοντα στην αναλυτική χαρτογραφία[1], κατά τον μετασχηματισμό μιας επιφάνειας αναφοράς (π.χ., του ΕΕΠ) σε μία επιφάνεια απεικόνισης δημιουργούνται γραμμικές, επιφανειακές και γωνιακές παραμορφώσεις. Για την αξιολόγηση των παραμορφώσεων αυτών χρησιμοποιούνται καταρχήν οι επόμενες παράμετροι, οι οποίες παρουσιάζονται σε όλα τα κλασσικά συγγράμματα της αναλυτικής χαρτογραφίας[2].

Η **τοπική κλίμακα γραμμικής παραμόρφωσης μ** (local linear scale), ή απλά γραμμική παραμόρφωση κατά μήκος μιας διεύθυνσης σε ένα σημείο της επιφάνειας απεικόνισης είναι το κλάσμα του μήκους μιας στοιχειώδους γραμμής ds στο επίπεδο απεικόνισης προς το μήκος ds' της αντίστοιχης στοιχειώδους γραμμής στην επιφάνεια αναφοράς (ΕΕΠ ή σφαίρα). Για την ποσοτική μέτρηση της γραμμικής παραμόρφωσης συνήθως χρησιμοποιείται ο συντελεστής γραμμικής κλίμακας. Ο **συντελεστής γραμμικής κλίμακας** (linear scale factor) κατά μήκος μιας διεύθυνσης σε ένα σημείο της επιφάνειας απεικόνισης είναι το κλάσμα της τοπικής κλίμακας γραμμικής παραμόρφωσης προς την κύρια κλίμακα. Η **κύρια κλίμακα μ_o** (principal scale), γνωστή και ως συντελεστής απεικόνισης (representation factor) είναι η κλίμακα του σμικρυμένου γεωμετρικού μοντέλου της γης (ΕΕΠ ή σφαίρας) και ορίζεται ως το κλάσμα των αντίστοιχων ακτίνων του ισημερινού (για το σμικρυμένο και για το αρχικό μοντέλο).

Για την αποτελεσματικότερη ανάλυση των παραμορφώσεων, ο συντελεστής γραμμικής κλίμακας προσδιορίζεται θεωρώντας ότι η τιμή της κύριας κλίμακας είναι ίση με ένα. Με τον τρόπο αυτό η τιμή του συντελεστή γραμμικής κλίμακας είναι ίση με την τοπική κλίμακα γραμμικής παραμόρφωσης. Ο ***συντελεστής γραμμικής κλίμακας στη διεύθυνση του μεσημβρινού*** συμβολίζεται με **h** και ο ***συντελεστής γραμμικής κλίμακας στη διεύθυνση του παραλλήλου*** με **k**. Πολλές φορές οι συντελεστές αυτοί χρησιμοποιούνται με τη μορφή του σφάλματος γραμμικής κλίμακας, το οποίο υπολογίζεται από τις διαφορές: (h-1) και (k-1).

Η **τοπική κλίμακα επιφανειακής παραμόρφωσης** (local area scale), ή απλά επιφανειακή παραμόρφωση σε ένα σημείο του επιπέδου απεικόνισης είναι το κλάσμα του εμβαδού dE ενός στοιχειώδους τετραπλεύρου στο επίπεδο απεικόνισης προς το εμβαδό dE' του αντίστοιχου στοιχειώδους τετραπλεύρου στην επιφάνεια αναφοράς (ΕΕΠ ή σφαίρα). Για την ποσοτική μέτρηση της επιφανειακής παραμόρφωσης συνήθως χρησιμοποιείται ο συντελεστής επιφανειακής κλίμακας.

Ο **συντελεστής επιφανειακής κλίμακας p** (area scale factor) είναι το κλάσμα της τοπικής κλίμακας επιφανειακής παραμόρφωσης προς την κλίμακα επιφανειακής παραμόρφωσης στη **κεντρική γραμμή**, ή το **κεντρικό σημείο** της απεικόνισης. Μία γραμμή/ένα σημείο ονομάζεται

[1] (Richardus and Adler 1972), (Pearson 1990), (Bugayevskiy and Snyder 1995), (Yang. Snyder and Tobler 2000), (Grafarend and Krumm 2006).

[2] (Maling, 1973), (Snyder 1987), (Νάκος 2006).

κεντρική/ό, όταν οι γραμμικές, οι επιφανειακές και οι γωνιακές παραμορφώσεις στη γραμμή αυτή/(στο σημείο αυτό) έχουν τις ελάχιστες τιμές.

Πολλές φορές ο συντελεστής επιφανειακής κλίμακας χρησιμοποιείται με τη μορφή του σφάλματος επιφανειακής κλίμακας το οποίο υπολογίζεται από τη διαφορά: (p-1).

Η γωνιακή παραμόρφωση, ορίζεται αποτελεσματικότερα με την αναφορά στις βασικές αρχές του θεωρήματος του Tissot και σε παραμέτρους της έλλειψης παραμόρφωσης. Σύμφωνα με το θεώρημα του Tissot (Richardus and Adler 1973):

- Κάθε στοιχειώδης κύκλος στην επιφάνεια της σφαίρας (ή του ΕΕΠ) απεικονίζεται στο επίπεδο ως έλλειψη γνωστή ως έλλειψη παραμόρφωσης, ή **δείκτρια Tissot** (Σχ. 3).
- Σε κάθε σημείο της σφαίρας (ή του ΕΕΠ) υπάρχουν δύο διευθύνσεις που τέμνονται με γωνία 90° οι οποίες απεικονίζονται στο επίπεδο με γραμμές που τέμνονται επίσης με γωνία 90°. Οι διευθύνεις αυτές λέγονται **κύριες διευθύνσεις**.
- Οι κύριες διευθύνσεις, ανάλογα με τη χρησιμοποιούμενη χαρτογραφική απεικόνιση, δεν αντιστοιχούν απαραίτητα στις διευθύνσεις του μεσημβρινού και του παραλλήλου.
- Η μέγιστη και η ελάχιστη τοπική κλίμακα γραμμικής παραμόρφωσης σε ένα σημείο, εμφανίζονται στις κύριες διευθύνσεις του μεγάλου και μικρού ημιάξονα της έλλειψης παραμόρφωσης αντιστοίχως.
- Όταν οι μεσημβρινοί και οι παράλληλοι στην επιφάνια απεικόνισης σχηματίζουν γωνία 90°, η τοπική κλίμακα γραμμικής παραμόρφωσης στη διεύθυνση του μεσημβρινού είναι ίση με τη μέγιστη τοπική κλίμακα γραμμικής παραμόρφωσης a και η τοπική κλίμακα γραμμικής παραμόρφωσης στη διεύθυνση του παραλλήλου είναι ίση με την ελάχιστη τοπική κλίμακα γραμμικής παραμόρφωσης b.

Γωνιακή παραμόρφωση ω, κατά μήκος μιας διεύθυνσης σε ένα σημείο του επιπέδου απεικόνισης είναι η διαφορά μεταξύ των γωνιών u και u', [ω = u - u'] οι οποίες ορίζονται ως εξής:

α.) Η γωνία u (Σχ. 3.α), αντιστοιχεί στη γωνία μεταξύ μιας τυχαίας διεύθυνσης Χ και της κύριας διεύθυνσης Ι της μέγιστης γραμμικής παραμόρφωσης στην επιφάνεια αναφοράς (ΕΕΠ, ή σφαίρα).

β.) Η γωνία u' (Σχ. 3.β), αντιστοιχεί στη γωνία μεταξύ της απεικόνισης Χ' της τυχαίας διεύθυνσης (γραμμής) και της απεικόνισης της κύριας διεύθυνσης της μέγιστης γραμμικής παραμόρφωσης Ι'' στην επιφάνεια απεικόνισης (στο επίπεδο).

Εξισώσεις παραμορφώσεων

Κατά την απεικόνιση μιας τυχαίας επιφάνειας αναφοράς, τα σημεία της οποίας προσδιορίζονται με τις παραμέτρους (φ, λ), οι οποίες δεν αναφέρονται απαραίτητα στο γεωγραφικό πλάτος και στο γεωγραφικό μήκος, σε μία επιφάνεια απεικόνισης (όχι κατ' ανάγκη σε επίπεδο), η γενική σχέση υπολογισμού της γραμμικής παραμόρφωσης μ σε οποιαδήποτε διεύθυνση ενός σημείου στην επιφάνεια απεικόνισης είναι:

$$\mu = \sqrt{\frac{E'd\varphi^2 + 2F'd\varphi\,d\lambda + G'd\lambda^2}{Ed\varphi^2 + 2Fd\varphi\,d\lambda + Gd\lambda^2}} \qquad (7)$$

Όπου:

- οι παράμετροι E΄, F΄, G΄ είναι τα βασικά θεμελιώδη μεγέθη πρώτης τάξης του Gauss για κάθε σημείο της επιφάνειας απεικόνισης που δίνονται από τις σχέσεις (8) έως (10) [Πολυράκης 2008].
- οι παράμετροι E, F, G είναι τα αντίστοιχα βασικά θεμελιώδη μεγέθη πρώτης τάξης για την επιφάνεια αναφοράς (datum surface).

$$E' = \left(\frac{\partial x}{\partial \varphi}\right)^2 + \left(\frac{\partial y}{\partial \varphi}\right)^2 \quad (8)$$

$$F' = \left(\frac{\partial x}{\partial \varphi}\right)\left(\frac{\partial y}{\partial \lambda}\right) + \left(\frac{\partial y}{\partial \varphi}\right)\left(\frac{\partial y}{\partial \lambda}\right) \quad (9)$$

$$G' = \left(\frac{\partial x}{\partial \lambda}\right)^2 + \left(\frac{\partial y}{\partial \lambda}\right)^2 \quad (10)$$

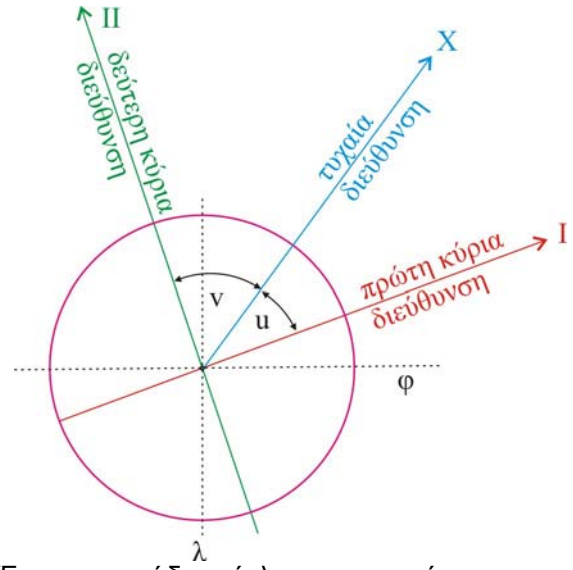

Ένας στοιχειώδης κύκλος στην επιφάνεια αναφοράς, θεωρείται ότι είναι επίπεδο σχήμα

α. Επιφάνεια αναφοράς (σφαίρα ή ΕΕΠ)

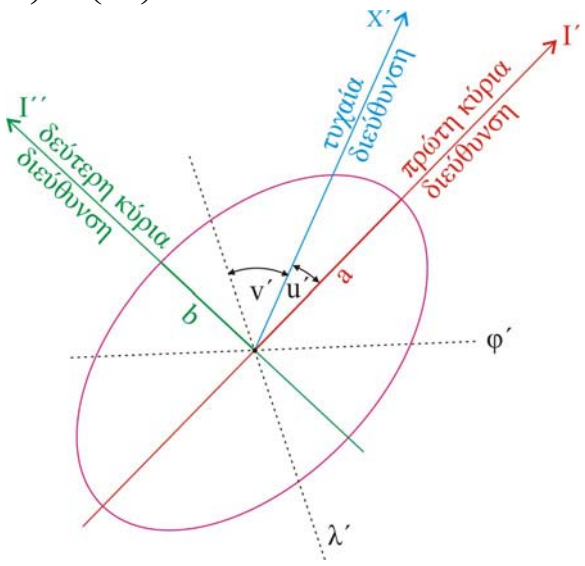

Η απεικόνιση του στοιχειώδους κύκλου στην επιφάνεια απεικόνισης είναι έλλειψη

β. Επιφάνεια απεικόνισης
(Σφαίρα, ή επίπεδο χαρτογραφικής απεικόνισης)

Σχήμα 3: Έλλειψη παραμόρφωσης

Στην κλασσική περίπτωση χρησιμοποίησης των χαρτογραφικών απεικονίσεων για την απευθείας απεικόνιση της επιφάνειας του ΕΕΠ σε επίπεδο (Σχ. 1), η επιφάνεια αναφοράς είναι η επιφάνεια του ΕΕΠ, η επιφάνεια απεικόνισης είναι το επίπεδο. Κατά το μετασχηματισμό της επιφάνειας του ΕΕΠ σε σφαιρική επιφάνεια (Σχ. 2), η επιφάνεια αναφοράς είναι η επιφάνεια του ΕΕΠ και η επιφάνεια απεικόνισης είναι η επιφάνεια της χρησιμοποιούμενης βοηθητικής σφαίρας.

Για την επιφάνεια του ΕΕΠ οι τιμές των μεγεθών E, F, G δίνονται από τις (11), (12) και 13).

$$E = R_M{}^2 = \frac{a^2(1-e^2)^2}{(1-e^2\sin^2\varphi)^3} \quad (11)$$

$$F = 0 \quad (12)$$

$$G = R_N{}^2\cos^2\varphi = \frac{a^2}{1-e^2\sin^2\varphi}\cos^2\varphi \quad (13)$$

Όπου:

R_M και R_N είναι οι ακτίνες καμπυλότητας ενός σημείου στη επιφάνεια του ΕΕΠ στις διευθύνσεις του μεσημβρινού και της πρώτης καθέτου αντιστοίχως.

Από τη γενική σχέση (7) με αντικατάσταση των τιμών των μεγεθών E, F και G σύμφωνα με τις (11), (12) και (13), προκύπτει η (14) για τον υπολογισμό της τοπικής γραμμικής παραμόρφωσης μ σε ένα σημείο του επιπέδου απεικόνισης οποιασδήποτε χαρτογραφικής απεικόνισης σε μία τυχαία διεύθυνση α .

$$\mu^2 = \frac{E'd\varphi^2 + 2F'd\varphi\, d\lambda + G'd\lambda^2}{R_M^2 d\varphi^2 + R_P^2 d\lambda^2} =$$

$$\mu^2 = \frac{E'}{R_M^2}\cos^2\alpha + \frac{F'}{R_M R_P}\sin 2\alpha + \frac{G'}{R_P^2}\sin^2\alpha \qquad (14)$$

Από τη (14) που δίνει την τιμή της γραμμικής παραμόρφωσης μ σε μία διεύθυνση α , προκύπτουν οι (15) και (16) για τον υπολογισμό της γραμμικής παραμόρφωσης h στη διεύθυνση του μεσημβρινού (α=0°) και για τον υπολογισμό της τοπικής γραμμικής παραμόρφωσης k στη διεύθυνση του παραλλήλου (α=90°).

$$h = \frac{\sqrt{E'}}{R_M} \qquad (15)$$

$$k = \frac{\sqrt{G'}}{R_P} \qquad (16)$$

Για τον υπολογισμό της μέγιστης τοπικής κλίμακας γραμμικής παραμόρφωσης a και της ελάχιστης τοπικής κλίμακας γραμμικής παραμόρφωσης b, χρησιμοποιούνται οι (17) και (18).

$$a = \frac{1}{2}\left(\sqrt{h^2 + 2hk\cos\varepsilon + k^2} + \sqrt{h^2 - 2hk\cos\varepsilon + k^2}\right) \qquad (17)$$

$$b = \frac{1}{2}\left(\sqrt{h^2 + 2hk\cos\varepsilon + k^2} - \sqrt{h^2 - 2hk\cos\varepsilon + k^2}\right) \qquad (18)$$

Όπου:

ε : είναι η συμπληρωματική γωνία της γωνίας τομής του μεσημβρινού και παραλλήλου i $(\varepsilon = 90^\circ - i)$, που δίνεται από τη (19).

$$\varepsilon = \arctan\left(-\frac{F'}{H'}\right) \qquad (19)$$

Όπου:

Η είναι η διακρίνουσα της επιφάνειας αναφοράς σε ένα σημείο του επιπέδου απεικόνισης που δίνεται από την (20).

$$H = \sqrt{E'G' - F'^2} \qquad (20)$$

Ο υπολογισμός της τοπικής κλίμακας επιφανειακής παραμόρφωσης p, πραγματοποιείται με τη (21).

$$p = hk\cos\varepsilon = ab \qquad (21)$$

Η μέγιστη γωνιακή παραμόρφωση ω σε κάθε σημείο του επιπέδου απεικόνισης δίνεται από την (22).

$$\omega = \frac{|h - k|}{h + k} \qquad (22)$$

Από την ανωτέρω συνοπτική παρουσίαση προκύπτει ότι για τον υπολογισμό των γραμμικών, των επιφανειακών και των γωνιακών παραμορφώσεων με τις (14) έως (22) απαιτείται ο προσδιορισμός των μεγεθών:

- E, F, G και H για την επιφάνεια αναφοράς.
- E΄, F΄, G΄ και H΄ σε ένα σημείο της επιφάνειας απεικόνισης.

Για τον προσδιορισμό των μεγεθών E, F, H και G στα σημεία της επιφάνειας της σφαίρας χρησιμοποιούνται οι (11) έως (13) με τιμή της πρώτης εκκεντρότητας e ίση με μηδέν (e=0) και αντικατάσταση της παραμέτρου a με την τιμή της ακτίνας R της σφαίρας (συνήθως χρησιμοποιείται σφαίρα μοναδιαίας ακτίνας, R=1). Στη συνέχεια προσδιορίζονται τα μεγέθη E΄, F΄, H΄ και G΄ με τις (8) έως (10) από τα οποία προκύπτουν τύποι προσδιορισμού των γραμμικών, επιφανειακών και γωνιακών παραμορφώσεων.

ΜΕΤΑΣΧΗΜΑΤΙΣΜΟΣ ΤΗΣ ΕΠΙΦΑΝΕΙΑΣ ΤΟΥ ΕΛΛΕΙΨΟΕΙΔΟΥΣ ΣΕ ΣΥΜΜΟΡΦΗ ΣΦΑΙΡΑ

Οι συναρτήσεις του μετασχηματισμού της επιφάνειας του ΕΕΠ σε σύμμορφη σφαίρα, προκύπτουν από την εφαρμογή της συνθήκης συμμορφίας (h = k) με την οποία εξασφαλίζεται ότι κατά τον μετασχηματισμό δεν δημιουργούνται γωνιακές παραμορφώσεις (Bugayevskiy and Snyder 1995). Ανάλογα με τα επιθυμητά χαρακτηριστικά της χρησιμοποιουμένης σύμμορφης σφαίρας, οι (4) και (6) λαμβάνουν διαφορετικές τιμές. Οι κυριότερες μέθοδοι μετασχηματισμού της επιφάνειας του ΕΕΠ σε σφαίρα συμμορφίας είναι:

- Ο μετασχηματισμός με μηδενισμό των γραμμικών παραμορφώσεων στον ισημερινό που προτάθηκε αρχικά από τον Mollweide το έτος 1807,
- ο μετασχηματισμός με μηδενισμό των γραμμικών παραμορφώσεων στο βασικό παράλληλο που προτάθηκε αρχικά από τον Gauss το έτος 1822 και
- ο μετασχηματισμός με μηδενισμό των γραμμικών παραμορφώσεων στον κεντρικό μεσημβρινό που προτάθηκε αρχικά από τον Gauss το έτος 1844.

Στο μετασχηματισμό της επιφάνειας του ΕΕΠ σε σύμμορφη σφαίρα με μηδενισμό των γραμμικών παραμορφώσεων στον ισημερινό, η ακτίνα R_c της σύμμορφης σφαίρας έχει σταθερή τιμή ίση με την τιμή του μεγάλου ημιάξονα του ΕΕΠ (R_c=a).

Στο μετασχηματισμό της επιφάνειας του ΕΕΠ σε σύμμορφη σφαίρα με μηδενισμό των γραμμικών παραμορφώσεων στον κεντρικό μεσημβρινό η ακτίνα R_c της σύμμορφης σφαίρας δεν είναι σταθερή αλλά εξαρτάται από το γεωγραφικό πλάτος και το γεωγραφικό μήκος του κεντρικού σημείου.

Στο μετασχηματισμό που εξασφαλίζει μηδενισμό των γραμμικών παραμορφώσεων στο βασικό παράλληλο η ακτίνα R_c της σύμμορφης σφαίρας δεν είναι σταθερή αλλά εξαρτάται από το γεωγραφικό πλάτος του βασικού παραλλήλου.

Για το σκοπό της εκτελεσθείσας έρευνας επιλέχτηκε για αξιολόγηση ο μετασχηματισμός που εξασφαλίζει μηδενισμό των γραμμικών παραμορφώσεων στον ισημερινό επειδή: i) στο μετασχηματισμό αυτό χρησιμοποιείται σύμμορφη σφαίρα σταθερής ακτίνας, ii) οι δημιουργουμένες γραμμικές παραμορφώσεις κατά μήκος των μεσημβρινών είναι πρακτικά αμελητέες για τις εφαρμογές χαρτογραφικής απεικόνισης σε περιβάλλον ΣΓΠ (GIS) [Παλληκάρης 2010].

Με την εφαρμογή της συνθήκης συμμορφίας (h=k), στο μετασχηματισμό της επιφάνειας του ΕΕΠ σε σύμμορφη σφαίρα με μηδενική γραμμική παραμόρφωση στον ισημερινό, προκύπτουν οι (23) έως (30), οι οποίες δίνουν τους συντελεστές A_2, A_4, A_6, A_8, B_2, B_4, B_6 και B_8 των συναρτήσεων μετασχηματισμού (4) και (6) [Yang, Snyder and Tobler 2000].

$$A_2 = \frac{1}{2}e^2 + \frac{5}{24}e^4 + \frac{3}{32}e^6 + \frac{1399}{53760}e^8 \qquad (23)$$

$$A_4 = -\left(\frac{5}{48}e^4 + \frac{7}{80}e^6 + \frac{689}{17920}e^8\right) \qquad (24)$$

$$A_6 = \frac{13}{480}e^6 + \frac{1363}{17920}e^8 \quad (25)$$

$$A_8 = -\left(\frac{677}{107520}e^8\right) \quad (26)$$

$$B_2 = A_2 - A_2A_4 - A_4A_6 - \frac{1}{2}A_2^3 - A_2A_4^2 + \frac{1}{2}A_2^2A_6 - 18{,}3A_2^3A_4 \quad (27)$$

$$B_4 = A_4 + A_2^2 - 2A_2A_6 - 4A_2^2A_4 - 1{,}3A_2^4 \quad (28)$$

$$B_6 = A_6 + 3A_2A_4 - 3A_2A_8 + \frac{3}{2}A_2^3 - \frac{9}{2}A_2A_4^2 - 9A_2^2A_6 - 12{,}5A_2^3A_4 \quad (29)$$

$$B_8 = A_8 + 2A_4^2 + 4A_2A_6 + 8A_2^2A_4 + 2{,}7A_2^4 \quad (30)$$

Με την εφαρμογή των (15), (16) και (21), προκύπτουν (31) και (32), οι οποίες δίνουν τις τιμές της γραμμικής και της επιφανειακής παραμόρφωσης.

$$h = k = \frac{R}{a}\left(1 + \frac{1}{2}e^2\sin^2\varphi\right) \quad (31)$$

$$p = h^2 = \frac{R^2}{a^2}\left(1 + \frac{1}{2}e^2\sin^2\varphi\right)^2 \quad (32)$$

όπου: R = a = 6378137m *(για το ΕΕΠ WGS-84).*

ΜΕΤΑΣΧΗΜΑΤΙΣΜΟΣ ΤΗΣ ΕΠΙΦΑΝΕΙΑΣ ΤΟΥ ΕΛΛΕΙΨΟΕΙΔΟΥΣ ΣΕ ΙΣΟΔΥΝΑΜΗ ΣΦΑΙΡΑ

Οι συναρτήσεις του μετασχηματισμού της επιφάνειας του ΕΕΠ σε σύμμορφη σφαίρα, προκύπτουν από την εφαρμογή της συνθήκης συμμορφίας (m=1) με την οποία εξασφαλίζεται ότι κατά τον μετασχηματισμό δεν δημιουργούνται επιφανειακές (εμβαδικές) παραμορφώσεις, δηλαδή το εμβαδόν της επιφάνειας της ισοδύναμης σφαίρας είναι ίσο με το εμβαδόν της επιφάνειας του ελλειψοειδούς. Από την ανάλυση και επεξεργασία της συνθήκης αυτής), προσδιορίζεται, τόσο η ακτίνα R_a της ισοδύναμης σφαίρας, όσο και οι συντελεστές A_2, A_4, A_6, A_8, B_2, B_4, B_6 και B_8 των συναρτήσεων μετασχηματισμού (4) και (6) [Pearson 1990].

Η ακτίνα R_a της ισοδύναμης σφαίρας δίνεται από την (33). Οι συντελεστές A_2, A_4, A_6 , A_8, της συνάρτησης μετασχηματισμού (4), δίνονται από τις (34) έως (37). Οι συντελεστές B_2, B_4, B_6 και B_8 δίνονται από τις (27) έως (30) στις οποίες, όμως χρησιμοποιούνται οι τιμές των συντελεστών A_2, A_4, A_6 και A_8 των (34) έως (37).

$$R^2 = a^2(1-e^2)\left(1 + \frac{2}{3}e^2 + \frac{3}{5}e^4 + \frac{4}{7}e^6 + \frac{5}{9}e^8\right) \quad (33)$$

Κατά το μετασχηματισμό της επιφάνειας του ΕΕΠ σε ισοδύναμη σφαίρα στις συναρτήσεις των (4) και (6) οι συντελεστές A_2, A_4, A_6 , ι A_8, B_2, B_4, B_6 και B_8 είναι ίσοι με :

$$A_2 = \frac{1}{3}e^2 + \frac{31}{180}e^4 + \frac{59}{560}e^6 + \frac{126853}{518400}e^8 \quad (34)$$

$$A_4 = -\left(\frac{17}{360}e^4 + \frac{61}{1260}e^6 + \frac{3622447}{94089600}e^8\right) \quad (35)$$

$$A_6 = \frac{383}{45360}e^6 + \frac{6688039}{658627200}e^8 \quad (36)$$

$$A_8 = -\frac{27787}{23522400}e^8 \quad (37)$$

Με την εφαρμογή των (15), (16) και (22), προκύπτουν (38), (39) και (40), οι οποίες δίνουν τις τιμές της γραμμικής και της γωνιακής παραμόρφωσης.

$$h = 1 + \frac{e^2}{6}cos^2\varphi \quad (38)$$

$$k = 1 - \frac{e^2}{6}cos^2\varphi \quad (39)$$

$$\sin\frac{\omega}{2} = \frac{e^2}{6}cos^2\varphi \quad (40)$$

ΜΕΤΑΣΧΗΜΑΤΙΣΜΟΣ ΤΗΣ ΕΠΙΦΑΝΕΙΑΣ ΤΟΥ ΕΛΛΕΙΨΟΕΙΔΟΥΣ ΣΕ ΙΣΑΠΕΧΟΥΣΑ ΣΤΗ ΔΙΕΥΘΥΝΣΗ ΤΩΝ ΜΕΣΗΜΒΡΙΝΩΝ ΣΦΑΙΡΑ

Οι συναρτήσεις του μετασχηματισμού της επιφάνειας του ΕΕΠ σε ισαπέχουσα στη διεύθυνση των μεσημβρινών σφαίρα, προκύπτουν από την εφαρμογή της συνθήκης μηδενισμού των γραμμικών παραμορφώσεων στη διεύθυνση του μεσημβρινού (m=1). Από την ανάλυση και επεξεργασία της συνθήκης αυτής προσδιορίζεται, τόσο η ακτίνα R_d της βοηθητικής σφαίρας, όσο και οι συντελεστές A_2, A_4, A_6 , ι A_8, B_2, B_4, B_6 και B_8 των συναρτήσεων μετασχηματισμού (4) και (6) [Yang, Snyder and Tobler 2000].

Η ακτίνα R_a της ισαπέχουσας στη διεύθυνση των μεσημβρινών σφαίρας δίνεται από την (41). Οι συντελεστές A_2, A_4, A_6 , A_8, της συνάρτησης μετασχηματισμού (4), δίνονται από τις (42) έως (51). Οι συντελεστές B_2, B_4, B_6 και B_8 δίνονται από τις (27) έως (30) στις οποίες, όμως χρησιμοποιούνται οι τιμές των συντελεστών A_2, A_4, A_6 και A_8 των (42) έως (45).

$$R_d = a^2(1-e^2)\left(1 + \frac{3}{4}e^2 + \frac{45}{64}e^4 + \frac{175}{256}e^6 + \frac{11\,025}{16\,384}e^8\right) \quad (41)$$

$$A_2 = \frac{B'}{2A'} \quad (42)$$

$$A_4 = -\frac{C'}{4A'} \quad (43)$$

$$A_6 = \frac{D'}{6A'} \quad (44)$$

$$A_8 = -\frac{E'}{8A'} \quad (45)$$

$$A' = 1 + \frac{3}{4}e^2 + \frac{45}{64}e^4 + \frac{175}{256}e^6 + \frac{11\,025}{16\,384}e^8 \quad (46)$$

$$B' = \frac{3}{4}e^2 + \frac{15}{16}e^4 + \frac{525}{512}e^6 + \frac{2205}{2048}e^8 \quad (47)$$

$$C' = \frac{15}{16}e^4 + \frac{105}{256}e^6 + \frac{2205}{4096}e^8 \quad (48)$$

$$C' = \frac{15}{16}e^4 + \frac{105}{256}e^6 + \frac{2205}{4096}e^8 \quad (49)$$

$$D' = \frac{35}{512}e^6 + \frac{315}{2048}e^8 \quad (50)$$

$$E' = \frac{315}{16384}e^8 \quad (51)$$

Με την εφαρμογή των (15), (16) και (22), προκύπτουν οι (52) και (53), οι οποίες δίνουν τις τιμές της γραμμικής παραμόρφωσης στη διεύθυνση των παραλλήλων, της επιφανειακής παραμόρφωσης και της γωνιακής παραμόρφωσης.

$$k = p = 1 - \frac{e^4}{4}cos2\varphi \quad (52)$$

$$\omega' = 8482\ e^2 cos2\varphi \quad (53)$$

ΜΕΤΑΣΧΗΜΑΤΙΣΜΟΣ ΤΗΣ ΕΠΙΦΑΝΕΙΑΣ ΤΟΥ ΕΛΛΕΙΨΟΕΙΔΟΥΣ ΣΕ ΣΦΑΙΡΑ ΙΣΑΠΕΧΟΥΣΑ ΣΤΗ ΔΙΕΥΘΥΝΣΗ ΕΝΟΣ ΠΑΡΑΛΛΗΛΟΥ

Οι συναρτήσεις του μετασχηματισμού της επιφάνειας του ΕΕΠ σε ισαπέχουσα στη διεύθυνση των παραλλήλων σφαίρα, προκύπτουν από την εφαρμογή της συνθήκης μηδενισμού των γραμμικών παραμορφώσεων στη διεύθυνση των παραλλήλων (k=1). Από την ανάλυση και επεξεργασία της συνθήκης αυτής προσδιορίζεται, τόσο η ακτίνα R_p της βοηθητικής σφαίρας, όσο και οι συντελεστές A_2, A_4, A_6 , A_8, B_2, B_4, B_6 και B_8 των συναρτήσεων μετασχηματισμού (4) και (6) [Yang, Snyder and Tobler 2000]. Εν τούτοις η υλοποίηση της συνθήκης αυτής είναι δυνατό να πραγματοποιηθεί με διάφορους τρόπους, από τους οποίους είναι δυνατό να προκύψουν διάφορες ισαπέχουσες στη διεύθυνση των παραλλήλων σφαίρες με διαφορετικά χαρακτηριστικά εκάστη. Για παράδειγμα, τα απεικονιζόμενα στη βοηθητική σφαίρα σημεία του ΕΕΠ είναι δυνατό να έχουν το ίδιο γεωγραφικό μήκος και διαφορετικό γεωγραφικό πλάτος με τα αντίστοιχα σημεία του ΕΕΠ, ή να έχουν το ίδιο πλάτος και διαφορετικό μήκος. Ο συνηθέστερος τρόπος μετασχηματισμού της επιφάνειας του ΕΕΠ σε ισαπέχουσα στη διεύθυνση των παραλλήλων σφαίρα ικανοποιεί τις επόμενες συνθήκες:

- Το γεωδαιτικό πλάτος φ και το σφαιρικό γεωγραφικό πλάτος φ΄ έχουν τις ίδιες τιμές στον ισημερινό [$\varphi_0 = \varphi'_0 = 0$] και στους πόλους [$\varphi_{90} = \varphi'_{90} = 90$].
- Το γεωδαιτικό μήκος λ είναι ίσο με το σφαιρικό γεωγραφικό μήκος [λ= λ΄].

Η τιμή της ακτίνας R_p της ισαπέχουσας στη διεύθυνση των παραλλήλων σφαίρας δίνεται από την (54). Οι συντελεστές A_2, A_4, A_6 , A_8, της συνάρτησης μετασχηματισμού (4), δίνονται από τις (55) έως (59). Οι συντελεστές B_2, B_4, B_6 και B_8 δίνονται από τις (27) έως (30) στις οποίες, όμως χρησιμοποιούνται οι τιμές των συντελεστών A_2, A_4, A_6 και A_8 των (55) έως (58).

Το σφαιρικό πλάτος φ΄ στην ισαπέχουσα στη διεύθυνση ενός παραλλήλου βοηθητική σφαίρα, είναι ίσο με το χρησιμοποιούμενο στη γεωμετρική γεωδαισία ανηγμένο πλάτος u (60) [Bugayevskiy and Snyder 1995].

$$R_p = a \tag{54}$$

$$A_2 = n_o \tag{55}$$

$$A_4 = \frac{n_o^2}{2} \tag{56}$$

$$A_6 = \frac{n_o^3}{3} \tag{57}$$

$$A_8 = \frac{n_o^4}{4} \tag{58}$$

$$n_o = \frac{1 - \sqrt{1 - e^2}}{1 + \sqrt{1 - e^2}} \tag{59}$$

Οι συντελεστές B_2, B_4, B_6 και B_8 δίνονται από τις (27) έως (30) στις οποίες, όμως χρησιμοποιούνται οι τιμές των συντελεστών A_2, A_4, A_6 και A_8 των σχέσεων (55) έως (58).

Με την εφαρμογή των (15), (16) και (22), προκύπτουν οι (60) και (61), οι οποίες δίνουν τις τιμές της γραμμικής παραμόρφωσης στη διεύθυνση των μεσημβρινών, της επιφανειακής παραμόρφωσης και της γωνιακής παραμόρφωσης.

$$h = p = 1 + \frac{e^2}{2}cos^2\varphi + \frac{e^4}{8}(3 - 2\sin^2\varphi - 4\sin^4\varphi) \tag{60}$$

$$\omega' = 16965\, e^2 cos^2\varphi \tag{61}$$

ΑΞΙΟΛΟΓΗΣΗ ΜΕΘΟΔΩΝ ΜΕΤΑΣΧΗΜΑΤΙΣΜΟΥ ΤΗΣ ΕΠΙΦΑΝΕΙΑΣ ΤΟΥ ΕΛΛΕΙΨΟΕΙΔΟΥΣ ΣΕ ΣΦΑΙΡΑ

Η αξιολόγηση των μεθόδων μετασχηματισμού της επιφάνειας του ελλειψοειδούς εκ περιστροφής σφαίρα έγινε σε δύο στάδια. Κατά το πρώτο στάδιο έγινε αξιολόγηση των σχέσεων μετατροπής του γεωδαιτικού πλάτους σε σφαιρικό γεωγραφικό πλάτος, καθώς και της αντίστροφης μετατροπής του σφαιρικού γεωγραφικού πλάτους σε γεωδαιτικό πλάτος με τις (4) και (6) για τη σφαίρα συμμορφίας, την ισοδύναμη σφαίρα, την ισαπέχουσα στους μεσημβρινούς σφαίρα και την ισαπέχουσα στους παραλλήλους σφαίρα. Κατά το δεύτερο στάδιο έγινε υπολογισμός και ανάλυση των γραμμικών, των επιφανειακών και των γωνιακών παραμορφώσεων, οι οποίες δημιουργούνται κατά τους μετασχηματισμούς σε σύμμορφη σφαίρα, σε ισοδύναμη σφαίρα, σε ισαπέχουσα στους μεσημβρινούς σφαίρα και σε ισαπέχουσα στους παραλλήλους σφαίρα.

Αξιολόγηση των σχέσεων μετατροπής γεωδαιτικού πλάτους σε σφαιρικό

Τα βασικά αποτελέσματα της αξιολόγησης των τύπων των σχέσεων μετατροπής του γεωδαιτικού πλάτους σε σφαιρικό γεωγραφικό πλάτος παρουσιάζονται στο διάγραμμα του σχήματος 4. Από τη μελέτη και ανάλυση των αποτελεσμάτων αυτών προκύπτουν οι επόμενες διαπιστώσεις:

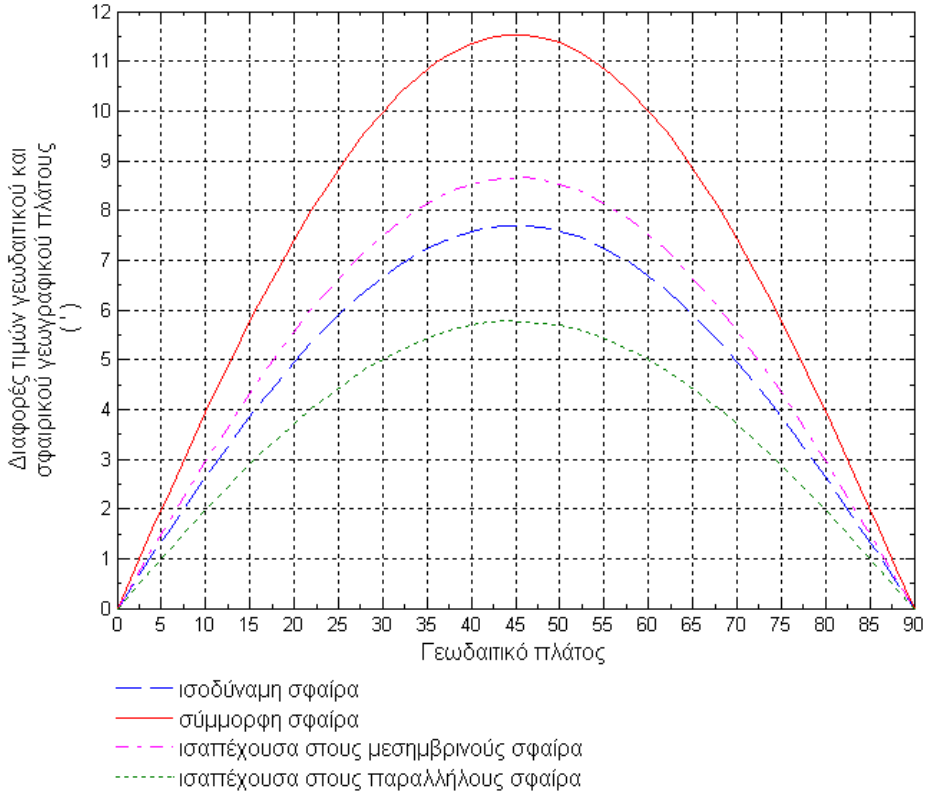

Σχήμα 4: Διαφορές γεωδαιτικού πλάτους και σφαιρικού γεωγραφικού πλάτους για τέσσερις βοηθητικές σφαίρες

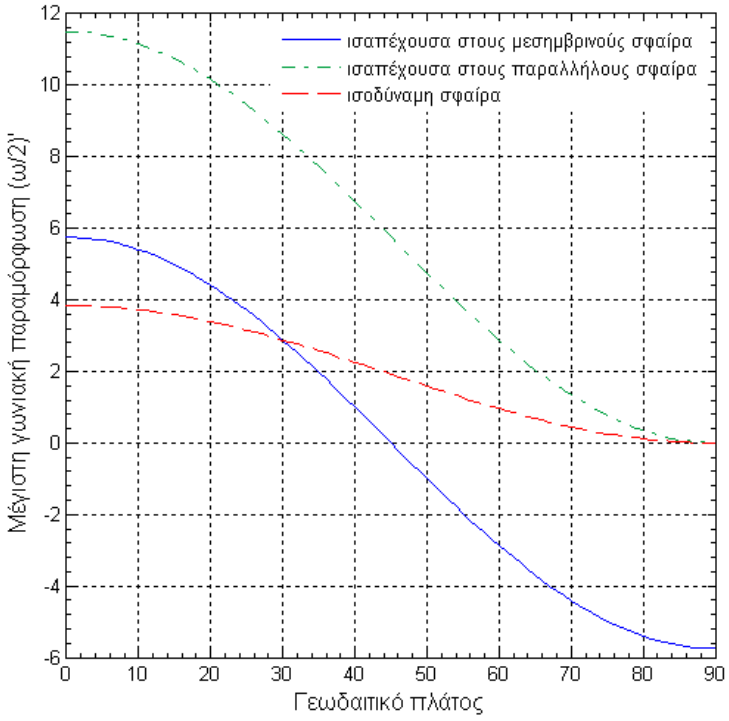

Σχήμα 5: Γωνιακές παραμορφώσεις μετασχηματισμού επιφάνειας ΕΕΠ σε σφαίρα

- Οι μέγιστες αποκλίσεις μεταξύ του γεωδαιτικού πλάτους και του σφαιρικού γεωγραφικού πλάτους δημιουργούνται σε πλάτος περίπου 45° και είναι περίπου 11΄,54 για τη σφαίρα συμμορφίας, 7΄,7 για την ισοδύναμη σφαίρα, 8΄,8 για την ισαπέχουσα στους μεσημβρινούς σφαίρα και 5΄,77 για την ισαπέχουσα στους παραλλήλους σφαίρα.
- Οι ελάχιστες αποκλίσεις του γεωδαιτικού πλάτους και του σφαιρικού γεωγραφικού πλάτους παρατηρούνται σε μικρά και σε μεγάλα γεωγραφικά πλάτη. Οι αποκλίσεις μηδενίζονται στον ισημερινό και στους πόλους.
- Ο μετασχηματισμός του γεωδαιτικού πλάτους φ σε σφαιρικό γεωγραφικό πλάτος φ_σ ($\varphi \rightarrow \varphi_\sigma$) καθώς και ο αντίστροφος μετασχηματισμός ($\varphi_\sigma \rightarrow \varphi$) με τις (4) και (6), προσαρμοσμένες για τις τέσσερις εξετασθείσες σφαίρες, παρέχει απόλυτη ταύτιση των αποτελεσμάτων για τον ευθύ και για τον αντίστροφο μετασχηματισμό. Οι τιμές του φ_σ που προσδιορίζονται με τους τύπους (4), όταν χρησιμοποιηθούν στη (5) δίνουν ακριβώς τις ίδιες τιμές του αρχικού γεωδαιτικού πλάτους που χρησιμοποιήθηκε στον ευθύ μετασχηματισμό.

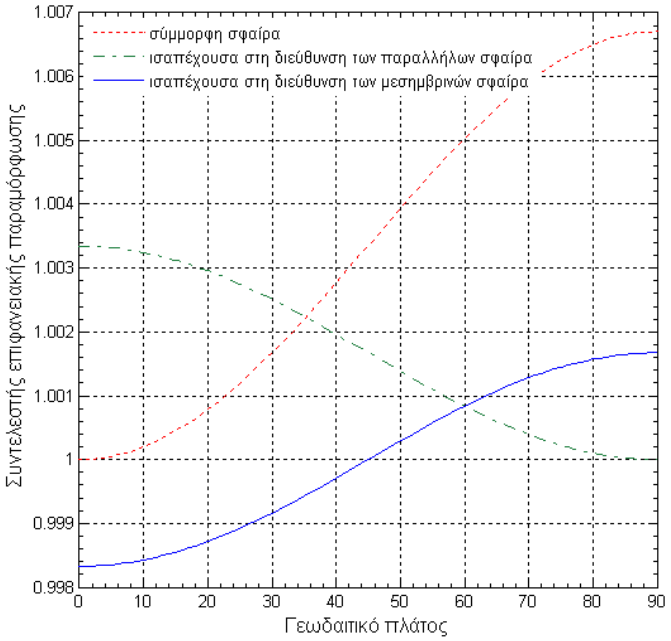

Σχήμα 6: Επιφανειακές παραμορφώσεις μετασχηματισμού επιφάνειας ΕΕΠ σε σφαίρα

Υπολογισμός και ανάλυση παραμορφώσεων

Τα αποτελέσματα των υπολογισμών αυτών παρουσιάζονται συνοπτικά στα διαγράμματα των σχημάτων 5 και 6. Από την ανάλυση των στοιχείων αυτών, προκύπτει:

- Κατά το μετασχηματισμό της επιφάνειας του ΕΕΠ σε οποιαδήποτε από τις ανωτέρω τέσσερις βοηθητικές σφαίρες (σφαίρα συμμορφίας, ισοδύναμη σφαίρα, ισαπέχουσα στους μεσημβρινούς σφαίρα και ισαπέχουσα στους παραλλήλους σφαίρα), οι δημιουργούμενες γραμμικές, γωνιακές και επιφανειακές παραμορφώσεις είναι πρακτικά αμελητέες για το σκοπό της εκτελεσθείσας έρευνας (χαρτογραφική απεικόνιση ολόκληρης, ή τμήματος της επιφάνειας της γης).
- Η μέγιστη γραμμική παραμόρφωση είναι περίπου 0.33%. Η παραμόρφωση αυτή παρατηρείται στους πόλους της σύμμορφης σφαίρας και της ισαπέχουσας στους παραλλήλους

σφαίρας. Η ελάχιστη γραμμική παραμόρφωση (πλην της σύμμορφης σφαίρας) είναι περίπου 0.12%. Η παραμόρφωση αυτή παρατηρείται στον ισημερινό της ισοδύναμης σφαίρας.

- Η μέγιστη γωνιακή παραμόρφωση είναι περίπου 11΄.5. Η παραμόρφωση αυτή παρατηρείται στον ισημερινό της ισαπέχουσας στους παραλλήλους σφαίρας. Η ελάχιστη γωνιακή παραμόρφωση (πλην της σύμμορφης σφαίρας) είναι περίπου 3΄.8. Η παραμόρφωση αυτή παρατηρείται στον ισημερινό και τους πόλους της ισοδύναμης σφαίρας.
- Η μέγιστη επιφανειακή παραμόρφωση είναι περίπου 0.69%. Η παραμόρφωση αυτή παρατηρείται στους πόλους της σύμμορφης σφαίρας. Η ελάχιστη επιφανειακή παραμόρφωση είναι περίπου 0.57%. Η παραμόρφωση αυτή παρατηρείται στον ισημερινό της ισαπέχουσας στους παραλλήλους σφαίρας.
- Η ισαπέχουσα στους μεσημβρινούς σφαίρα δεν εμφανίζει μεγάλες τιμές γραμμικών ή γωνιακών παραμορφώσεων, όπως η σύμμορφη και η ισοδύναμη σφαίρα αντιστοίχως. Επίσης η ισαπέχουσα στους μεσημβρινούς σφαίρα εμφανίζει μικρότερες γωνιακές και επιφανειακές παραμορφώσεις από την ισαπέχουσα στους παραλλήλους σφαίρα.

ΣΥΝΟΨΗ - ΣΥΜΠΕΡΑΣΜΑΤΑ

Στο παρόν άρθρο παρουσιάστηκαν και αξιολογήθηκαν τέσσερις μέθοδοι μετασχηματισμού της επιφάνειας του ελλειψοειδούς σε σφαιρική επιφάνεια με σκοπό τον περαιτέρω μετασχηματισμό της σφαιρικής αυτής επιφάνειας σε επίπεδο με τη χρήση χαρτογραφικών προβολών για τις οποίες δεν υπάρχουν εξισώσεις μετασχηματισμού του ελλειψοειδούς. Πιο συγκεκριμένα παρουσιαστήκαν και αξιολογηθήκαν συναρτήσεις για τον ευθύ και για τον αντίστροφο μετασχηματισμό των γεωδαιτικών συντεταγμένων (φ, λ) των σημείων του ελλειψοειδούς (επιφάνειας αναφοράς) στις σφαιρικές συντεταγμένες (φ΄, λ΄) των σημείων της σφαίρας (επιφάνειας απεικόνισης) για τις επόμενες περιπτώσεις:

- μετασχηματισμός της επιφάνειας του ελλειψοειδούς σε σφαίρα χωρίς γωνιακές παραμορφώσεις (σφαίρα συμμορφίας)
- μετασχηματισμός της επιφάνειας του ελλειψοειδούς σε σφαίρα χωρίς επιφανειακές (εμβαδικές) παραμορφώσεις (ισοδύναμη σφαίρα)
- μετασχηματισμός της επιφάνειας του ελλειψοειδούς σε σφαίρα χωρίς γραμμικές παραμορφώσεις στη διεύθυνση των μεσημβρινών (σφαίρα ισαπέχουσα στη διεύθυνση των μεσημβρινών)
- μετασχηματισμός της επιφάνειας του ελλειψοειδούς σε σφαίρα χωρίς γραμμικές παραμορφώσεις στη διεύθυνση ενός παραλλήλου πλάτους (σφαίρα ισαπέχουσα στη διεύθυνση ενός παραλλήλου πλάτους)

Για την αξιολόγηση των παραπάνω μεθόδων μετασχηματισμού της επιφάνειας του ελλειψοειδούς σε σφαιρική επιφάνεια έγινε υπολογισμός και ανάλυση της κατανομής των παραμορφώσεων (γραμμικών, επιφανειακών και γωνιακών) που δημιουργούνται κατά τους μετασχηματισμούς αυτούς. Τα αποτελέσματα αυτής της αξιολόγησης μπορούν να αξιοποιηθούν στην επιλογή της καταλληλότερης μεθόδου μετασχηματισμού για την χαρτογραφική απεικόνιση ολόκληρης, ή τμήματος της επιφάνειας της γης με βάση τις κατά περίπτωση επιθυμητές ιδιότητες (π.χ. μηδενισμός των γωνιακών παραμορφώσεων, μηδενισμός των γραμμικών παραμορφώσεων σε μία καθορισμένη διεύθυνση κλπ.), ανάλογα με τον σκοπό για τον οποίο προορίζεται κάθε χαρτογραφική απεικόνιση.

ΒΙΒΛΙΟΓΡΑΦΙΚΕΣ ΑΝΑΦΟΡΕΣ

1. Bugayevskiy, L. M. and J. P Snyder. *Map Projections – A Reference Manual*, Taylor & Francis, London 1995.

2. Grafarend, E. W. and F. Krumm. 2006. *Map projections - Cartographic Information Systems*. Springer Verlag.
3. Maling, D. H. 1973. *Coordinate Systems and Map Projections*. George Philip and Son Ltd., 2nd ed., Pergamon Press, Oxford.
4. Νάκος Β. *Αναλυτική Χαρτογραφία*. ΕΜΠ. 2006
5. Παλληκάρης, Α. 2010. *Διερεύνηση και Επίλυση Προβλημάτων Ναυσιπλοΐας και Οπτικοποίηση Δρομολογίων Πλου Μεγάλων Αποστάσεων σε Συστήματα Ηλεκτρονικού Χάρτη*. Διδακτορική Διατριβή. ΕΜΠ.
6. Πολυράκης Ι. *Στοιχειώδης Διαφορική Γεωμετρία.* Αθήνα 2008. ISBN-9789609090315.
7. Pearson, F, II. 1990. *Map Projections: Theory and Applications*. CRC Press. ISBN 0-8493-6888-X.
8. Richardus, P. Adler, R. K. 1972. *Map projections for Goedesists, Cartographers and Geographers*. North-Holland Pub. Co. Amsterdam.
9. Snyder, J. P. *Map Projections: A Working Manual*. U. S. Geological Survey Professional Paper 1395, Washington, DC: U. S. Government Printing Office.
10. Yang, Q. Snyder, J. P. Tobler, W. R. 2000. *Map Projection Transformation, Principles and Applications*. Taylor & Francis, London.

ISSN: 1791-4469 Copyright © 2012 Hellenic Naval Academy

Foundations of Newtonian Dynamics: An Axiomatic Approach for the Thinking Student

C. J. Papachristou [3]

Department of Physical Sciences, Naval Academy of Greece, Piraeus 18539, Greece

Abstract. Despite its apparent simplicity, Newtonian Mechanics contains conceptual subtleties that may cause some confusion to the deep-thinking student. These subtleties concern fundamental issues such as, e.g., the number of independent laws needed to formulate the theory, or, the distinction between genuine physical laws and derivative theorems. This article attempts to clarify these issues for the benefit of the student by revisiting the foundations of Newtonian Dynamics and by proposing a rigorous axiomatic approach to the subject. This theoretical scheme is built upon two fundamental postulates, namely, conservation of momentum and superposition property for interactions. Newton's Laws, as well as all familiar theorems of Mechanics, are shown to follow from these basic principles.

1. Introduction

Teaching introductory Mechanics can be a major challenge, especially in a class of students that are not willing to take anything for granted! The problem is that, even some of the most prestigious textbooks on the subject may leave the student with some degree of confusion, which manifests itself in questions like the following:

1. Is Newton's First Law a law of motion (of free bodies) or is it a statement of existence (of inertial reference frames)?
2. Are the first two Newton's Laws independent of each other? It seems that the First Law is but a special case of the Second!
3. Is the Second Law a true law or just a definition (of force)?
4. Is the Third Law more fundamental than conservation of momentum, or is it the other way around?
5. And, finally, how many *independent* laws are really needed in order to build a complete theoretical basis for Mechanics?

[3] papachristou@snd.edu.gr

In this article we describe an axiomatic approach to introductory Mechanics that is both rigorous and pedagogical. It purports to clarify issues like the ones mentioned above, at an early stage of the learning process, thus aiding the student to acquire a deep understanding of the basic ideas of the theory. It is not the purpose of this article, of course, to present an outline of a complete course of Mechanics! Rather, we will focus on the most fundamental concepts and principles, those that are taught at the early chapters of Dynamics (we will not be concerned with Kinematics, since this subject confines itself to a description of motion rather than investigating the physical laws governing this motion).

The axiomatic basis of our approach consists of two fundamental postulates, presented in Section 2. The first postulate (*P1*) embodies both the existence of *inertial reference frames* and the *conservation of momentum*, while the second one (*P2*) expresses a *superposition principle for interactions*. The *Law of Inertia* is deduced from *P1*.

In Sec.3, the concept of *force* on a particle subject to interactions is defined (as in *Newton's Second Law*) and *P2* is used to show that a composite interaction of a particle with others is represented by a vector sum of forces. Then, *P1* and *P2* are used to derive the *Law of Action and Reaction*. Finally, a generalization to systems of particles subject to external interactions is made.

For completeness of presentation, certain derivative concepts such as *angular momentum* and *work* are discussed in Sec.4. To make the article self-contained, proofs of all theorems are included.

2. The Fundamental Postulates

We begin with some basic definitions.

Definition 1. A *frame of reference* (or *reference frame*) is a coordinate system (or set of axes) used by an observer to measure the position, orientation, etc., of objects in space. The position of the observer him/herself is assumed *fixed* relative to his/her own frame.

Definition 2. An *isolated system of particles* is a system of particles subject only to their mutual interactions, i.e., subject to no *external* interactions. Any system of particles subject to external interactions that somehow cancel one another in order to make the system's motion identical to that of an isolated system will also be considered an "isolated" system. An isolated system consisting of a single particle is called a *free particle*.

Our first fundamental postulate of Mechanics is stated as follows:

Postulate 1. A class of frames of reference (*inertial frames*) exists such that, for any *isolated* system of particles, a vector equation of the following form is valid:

$$\sum_i m_i \vec{v}_i = \text{constant in time} \tag{1}$$

where $\vec{v}_i$ is the velocity of the particle indexed by *i* ($i = 1, 2, \cdots$) and m_i is a constant quantity associated with this particle, which quantity is independent of the number or nature of interactions the particle is subject to.

We call m_i the *mass* and $\vec{p}_i = m_i \vec{v}_i$ the *momentum* of this particle. Also, we call

$$\vec{P} = \sum_i m_i \vec{v}_i = \sum_i \vec{p}_i \tag{2}$$

the *total momentum* of the system, relative to the considered reference frame. Postulate 1, then, expresses the *principle of conservation of momentum*: the total momentum of an isolated system of particles, relative to an inertial reference frame, is constant in time. (The same is true, in particular, for a free particle.)

Corollary 1. A free particle moves with constant velocity (i.e., with no acceleration) relative to any *inertial* reference frame.

Corollary 2. Any two free particles move with constant velocities relative to each other.

Corollary 3. The position of a free particle may define the origin of an inertial frame of reference.

We note that Corollaries 1 and 2 constitute alternate expressions of the *Law of Inertia* (*Newton's First Law*).

Consider now an isolated system of two particles of masses m_1 and m_2. Assume that the particles are allowed to interact for some time interval *Δt*. By conservation of momentum,

$$\Delta(\vec{p}_1 + \vec{p}_2) = 0 \;\Rightarrow\; \Delta\vec{p}_1 = -\Delta\vec{p}_2 \;\Rightarrow\; m_1 \Delta\vec{v}_1 = -m_2 \Delta\vec{v}_2 \;.$$

We note that the changes in the velocities of the two particles within the (arbitrary) time interval *Δt* must be in opposite directions, a fact that is verified experimentally. Moreover,

$$\frac{|\Delta\vec{v}_1|}{|\Delta\vec{v}_2|} = \frac{m_2}{m_1} = \text{constant} \tag{3}$$

regardless of the kind of interaction or the time *Δt* (which also is an experimentally verified fact). These demonstrate, in practice, the validity of the first postulate. Moreover, Eq.(3) allows us to specify the mass of a particle numerically, relative to the mass of any other particle, by letting the two particles interact for some time.

So far we have examined the case of isolated systems and, in particular, free particles. Consider now a particle subject to interactions with the rest of the world. Then, in general (unless these interactions somehow cancel one another), the particle's momentum will not remain constant relative to an *inertial* reference frame, i.e., will be a function of time. Our second postulate, which expresses the *superposition principle for interactions*, asserts that external interactions act on a particle independently of one another and their effects are superimposed:

Postulate 2. If a particle of mass *m* is subject to interactions with particles $m_1, m_2, \cdots$, then, at each instant *t*, the rate of change of its momentum is equal to

$$\frac{d\vec{p}}{dt} = \sum_i \left(\frac{d\vec{p}}{dt}\right)_i \tag{4}$$

where $\left(d\vec{p}/dt\right)_i$ is the rate of change of the particle's momentum due solely to its interaction with particle m_i (i.e., the rate of change of $\vec{p}$ if the particle *m* interacted only with m_i).

3. The Concept of Force

We now *define* the concept of force, in a manner similar to *Newton's Second Law*:

Definition 3. Consider a particle of mass *m* that is subject to interactions. Let $\vec{p}(t)$ be the particle's momentum as a function of time, as measured relative to an *inertial* reference frame. The vector quantity

$$\vec{F} = \frac{d\vec{p}}{dt} \tag{5}$$

is called the *total force* acting on the particle at time *t*.

Taking into account that, for a single particle, $\vec{p} = m\vec{v}$ with fixed *m*, we may rewrite Eq.(5) in the equivalent form,

$$\vec{F} = m\vec{a} = m\frac{d\vec{v}}{dt} \tag{6}$$

where $\vec{a}$ is the particle's acceleration at time *t*.

Corollary 4. Consider a particle of mass *m* subject to interactions with particles $m_1, m_2, \cdots$. Let $\vec{F}$ be the total force on *m* at time *t*, and let $\vec{F}_i$ be the force on *m* due solely to its interaction with m_i . Then, by the superposition principle for interactions (Postulate 2) as expressed by Eq.(4), we have:

$$\vec{F} = \sum_i \vec{F}_i \tag{7}$$

Theorem 1. Consider two particles *1* and *2*. Let $\vec{F}_{12}$ be the force on particle *1* due to its interaction with particle *2* at time *t*, and let $\vec{F}_{21}$ be the force on particle *2* due to its interaction with particle *1* at the same instant. Then,

$$\vec{F}_{12} = -\vec{F}_{21} \tag{8}$$

Proof. By the superposition principle, the forces $\vec{F}_{12}$ and $\vec{F}_{21}$ are independent of the presence or not of other particles in interaction with particles *1* and *2*. Thus, without loss of generality, we may assume that the system of the two particles is isolated. Then, by conservation of momentum and by using Eq. (5),

$$\frac{d}{dt}\left(\vec{p}_1+\vec{p}_2\right)=0 \;\Rightarrow\; \frac{d\vec{p}_1}{dt}=-\frac{d\vec{p}_2}{dt} \;\Rightarrow\; \vec{F}_{12}=-\vec{F}_{21}\ .$$

Equation (8) expresses the *Law of Action and Reaction* (*Newton's Third Law*).

Theorem 2. The rate of change of the total momentum $\vec{P}(t)$ of a system of particles, relative to an inertial frame of reference, equals the total *external* force acting on the system at time *t*.

Proof. Consider a system of particles of masses $m_i\ (i=1,2,\cdots)$. Let $\vec{F}_i$ be the total *external* force on m_i (due to its interactions with particles *not belonging* to the system), and let $\vec{F}_{ij}$ be the *internal* force on m_i due to its interaction with m_j (by convention, $\vec{F}_{ij}=0$ when *i=j*). Then, by Eq.(5) and by taking into account Eq. (7),

$$\frac{d\vec{p}_i}{dt}=\vec{F}_i+\sum_j \vec{F}_{ij}\ .$$

By using Eq.(2) for the total momentum, we have:

$$\frac{d\vec{P}}{dt}=\sum_i \frac{d\vec{p}_i}{dt}=\sum_i \vec{F}_i+\sum_{ij}\vec{F}_{ij}\ .$$

But,

$$\sum_{ij}\vec{F}_{ij}=\sum_{ji}\vec{F}_{ji}=\frac{1}{2}\sum_{ij}\left(\vec{F}_{ij}+\vec{F}_{ji}\right)=0\,,$$

where the action-reaction law (8) has been taken into account. So, finally,

$$\frac{d\vec{P}}{dt}=\sum_i \vec{F}_i=\vec{F}_{ext} \tag{9}$$

where $\vec{F}_{ext}$ represents the *total external force* on the system.

4. Derivative Concepts and Theorems

Having presented the most fundamental concepts of Mechanics, we now turn to some useful derivative concepts and related theorems, such as those of angular momentum and its relation to torque, work and its relation to kinetic energy, and conservative force fields and their association with mechanical-energy conservation.

Definition 4. Let *O* be the origin of an *inertial* reference frame, and let $\vec{r}$ be the position vector of a particle of mass *m*, relative to *O*. The vector quantity

$$\vec{L}=\vec{r}\times\vec{p}=m\left(\vec{r}\times\vec{v}\right) \tag{10}$$

(where $\vec{p} = m\vec{v}$ is the particle's momentum in the considered frame) is called the *angular momentum* of the particle relative to *O*.

Theorem 3. The rate of change of the angular momentum of a particle, relative to *O*, is given by

$$\frac{d\vec{L}}{dt} = \vec{r} \times \vec{F} \equiv \vec{T} \tag{11}$$

where $\vec{F}$ is the *total* force on the particle at time *t*, and $\vec{T}$ is the *torque* of this force relative to *O*, at this instant.

Proof. Equation (11) is easily proven by differentiating Eq.(10) with respect to time, and by using Eq.(5).

Corollary 5. If the torque of the total force on a particle, relative to some point *O*, vanishes, then the angular momentum of the particle relative to *O* is constant in time (*principle of conservation of angular momentum*).

Under appropriate conditions, the above conservation principle can be extended to the more general case of a system of particles (see, e.g., [1-5]).

Definition 5. Consider a particle of mass *m* in a *force field* $\vec{F}(\vec{r})$, where $\vec{r}$ is the particle's position vector relative to the origin *O* of an inertial reference frame. Let *C* be a curve representing the trajectory of the particle from point *A* to point *B* in this field. Then, the line integral

$$W_{AB} = \int_A^B \vec{F}(\vec{r}) \cdot d\vec{r} \tag{12}$$

represents the *work* done by the force field on *m* along the path *C*. (*Note:* This definition is valid independently of whether or not additional forces, not related to the field, are acting on the particle; i.e., regardless of whether or not $\vec{F}(\vec{r})$ represents the total force on *m*.)

Theorem 4. Let $\vec{F}(\vec{r})$ represent the *total* force on a particle of mass *m* in a force field. Then, the work done on the particle along a path *C* from *A* to *B* is equal to

$$W_{AB} = \int_A^B \vec{F}(\vec{r}) \cdot d\vec{r} = E_{k,B} - E_{k,A} = \Delta E_k \tag{13}$$

where

$$E_k = \frac{1}{2} m v^2 = \frac{p^2}{2m} \tag{14}$$

is the *kinetic energy* of the particle.

Proof. By using Eq.(6), we have:

$$\vec{F}\cdot d\vec{r} = m\frac{d\vec{v}}{dt}\cdot d\vec{r} = m\vec{v}\cdot d\vec{v} = \frac{1}{2}m\,d(\vec{v}\cdot\vec{v}) = \frac{1}{2}m\,d(v^2) = mvdv\,,$$

from which Eq.(13) follows immediately.

Definition 6. A force field $\vec{F}(\vec{r})$ is said to be *conservative* if a scalar function $E_p(\vec{r})$ (*potential energy*) exists, such that the work on a particle along *any* path from *A* to *B* can be written as

$$W_{AB} = \int_A^B \vec{F}(\vec{r})\cdot d\vec{r} = E_{p,A} - E_{p,B} = -\Delta E_p \tag{15}$$

Theorem 5. If the total force $\vec{F}(\vec{r})$ acting on a particle *m* is conservative, with an associated potential energy $E_p(\vec{r})$, then the quantity

$$E = E_k + E_p = \frac{1}{2}mv^2 + E_p(\vec{r}) \tag{16}$$

(*total mechanical energy* of the particle) remains constant along any path traced by the particle (*conservation of mechanical energy*).

Proof. By combining Eq.(13) (which is generally valid for *any* kind of force) with Eq.(15) (which is valid for *conservative* force fields) we find:

$$\Delta E_k = -\Delta E_p \;\Rightarrow\; \Delta(E_k + E_p) = 0 \;\Rightarrow\; E_k + E_p = const.$$

Theorems 4 and 5 are readily extended to the case of a system of particles [1-5].

5. Summary and Concluding Remarks

Newtonian Mechanics is the first subject in Physics an undergraduate student is exposed to. It continues to be important even at the intermediate and advanced levels, despite the predominant role played there by the more general formulations of Lagrangian and Hamiltonian dynamics.

It is this author's experience as a teacher that, despite its apparent simplicity, Newtonian Mechanics contains certain conceptual subtleties that may leave the deep-thinking student with some degree of confusion. The average student, of course, is happy with the idea that the whole theory is built upon three rather simple laws attributed to Newton's genius. In the mind of the more demanding student, however, puzzling questions often arise, such as, e.g., how many *independent* laws we really need to fully formulate the theory, or, which ones should be regarded as truly fundamental laws of Nature, as opposed to others that can be *derived* as theorems.

This article suggested an axiomatic approach to introductory Mechanics based on two fundamental, empirically verifiable laws, namely, the *principle of conservation of momentum* and

the *principle of superposition for interactions*. We showed that all standard ideas of Mechanics (including, of course, Newton's Laws) naturally follow from these basic principles. To make our formulation as economical as possible, we expressed the first principle in terms of a system of particles and treated the single-particle situation as a special case. To make the article self-contained for the benefit of the student, explicit proofs of all theorems were given.

By no means do we assert, of course, that this particular approach is unique or pedagogically superior to other established methods that adopt different viewpoints regarding the axiomatic basis of Classical Mechanics (see, e.g., a historical overview of these viewpoints in the first chapter of [6]). Moreover, this approach suffers from the usual theoretical problems inherent in Newtonian Mechanics (see, e.g., [7,8]), most serious of which is the following: To test whether a given reference frame is inertial or not, one needs to check the constancy or not of the velocity of a free particle, relative to this frame. However, an absolutely "free" particle is only a theoretical conception, for the following reasons: (1) Every particle is subject to the long-range gravitational interaction with the rest of the world. (2) To observe a particle, one necessarily has to somehow interact with it. Thus, no matter how weak this interaction may be, the particle can no longer be considered free during the observation process.

In any case, it looks like Classical Mechanics remains a subject open to discussion and re-interpretation, and more can always be said about things that are usually taken for granted by most students (this is not exclusively their fault, of course!). Happily, some of my own students do not fall into this category. I honestly appreciate the hard time they enjoy giving me in class!

References

1. M. Alonso, E. J. Finn, *Fundamental University Physics*, Volume I: *Mechanics* (Addison-Wesley, 1967).
2. K. R. Symon, *Mechanics*, 3rd Edition (Addison-Wesley, 1971).
3. J. B. Marion, S. T. Thornton, *Classical Dynamics of Particles and Systems*, 4th Edition (Saunders College, 1995).
4. H. Goldstein, *Classical Mechanics*, 2nd Edition (Addison-Wesley, 1980).
5. C. J. Papachristou, *Introduction to Mechanics of Particles and Systems* (in Greek) (Naval Academy of Greece Publications, 2010) http://openeclass.snd.edu.gr/openeclass-2.6.1/modules/document/file.php/TOM6103/Mechanics%20Volume%20PDF.pdf
6. N. C. Rana, P. S. Joag, *Classical Mechanics* (Tata McGraw-Hill, 1991).
7. C.-E. Khiari, *Newton's Laws of Motion Revisited: Some Epistemological and Didactic Problems*, Lat. Am. J. Phys. Educ. **5** (2011) 10-15.
8. A. E. Chubykalo, A. Espinoza, B. P. Kosyakov, *The Inertial Property of Approximately Inertial Frames of Reference*, Eur. J. Phys. **32** (2011) 1347-1356.

A Study On Radioactive Source Imaging By Using A Pixelated CdTe Radiation Detector

K. Zachariadou[a,c], K. Karafasoulis[b,c], S. Seferlis[c], I. Papadakis[d], D. Loukas[d], C. Lambropoulos[e] , C. Potiriadis[c],

a. Technological Educational Institute of Piraeus, Department of Physics, Chemistry & Material Technology, P. Ralli & Thivon 250, 12244, Greece
b. Hellenic Army Academy, 16673 Vari, Greece
c. Greek Atomic Energy Commission, Patriarxou Grigoriou & Neapoleos, 15310 Athens, Greece
d. National Centre for Scientific Research "Demokritos" , Institute of Nuclear Physics, 15310 Athens, Greece
e. Technological Educational Institute of Chalkida, Psachna Evias 34400, Greece

Abstract. We present simulation studies on the ability of a proposed portable radiation detecting instrument to reconstruct images of radioactive sources. The instrument is a stack of ten CdTe layers placed 2 cm apart, consisting of 10000 pixels in a two-dimensional arrangement, occupying an area of 4cmx4cm. The image reconstruction is performed using LM-MELM, an imaging algorithm based on the Compton imaging technique. Point-like radioactive sources emitting gamma-rays in a broad energy range, located at various distances and orientations with respect to the detector's symmetry axis have been simulated in order to estimate the ability of the instrument to reconstruct the source images. Results on the reconstructed image resolution are presented.

Keywords: Monte Carlo simulations, Semiconductor detectors, Gamma-ray spectroscopy, Compton camera.
PACS: 24.10.Lx, 29.40.Wk, 29.30.Kv, 42.79.Pw

INTRODUCTION

Radiation detectors that use gamma-ray imaging technologies in order to identify radioactive sources are of great scientific interest because of their wide range of applications, including nuclear medicine, astrophysics, waste monitoring and counter terrorism. One of the best known such imaging technologies is the Compton imaging [1], based on the interactions of the emitted gamma-rays with the detector's sensitive elements via the Compton scattering process Although research in the Compton imaging technique's applications have begun in the 1990s, the growing global interest for accurate detection of radioactive sources combined with the rapid advances in detector technologies (both in terms of material fabrication and electronics), have nowadays given great impetus to the research and development of Compton imaging detectors with enhanced detection capability.

In this framework, the main objective of the current research paper is to evaluate the imaging performance of a Compton imaging instrument under development (COCAE) [2].

COCAE consists of ten parallel planar layers made of pixelated Cadmium Telluride (CdTe) crystals occupying an area of 4cmx4cm, placed 2cm apart from each other. Each detector's layer has 10,000 pixels arranged in two dimensions (100x100) bump-bonded on a two-dimensional array of silicon readout CMOS circuits. Both pixels and readout arrays are on top of an Al_2O_3 supporting printed circuit board layer.

The most important parameters in the design of a Compton imaging detector such as COCAE are the efficiency in detecting gamma-rays and the energy resolution, which affects the evaluation of the Compton scattering angle. COCAE is made of CdTe semiconductor crystals, thus it is expected to achieve an enhanced detection efficiency compared to Germanium (Ge) and Sodium Iodide (NaI) detectors, due to the higher atomic number of Cd and Te, resulting into a higher absorption of gamma-rays via the photoelectric effect. In order to achieve even better efficiency, a thick CdTe detector of several mm would be needed but such an increase of the crystal's thickness would deteriorate the detector energy resolution (due to the effect of incomplete charge collection of CdTe semiconductors). To bypass this restriction, COCAE instrument has been designed as a system of many thin stacked CdTe crystals instead of one thick mono-crystal. As to the energy resolution parameter, the challenge for COCAE is to achieve a high energy resolution without the need of cryogenics (CdTe semiconductors can be operated at room temperature due to their high energy bandwidth), which is important when considering a portable instrument.

In order to study its performance, the COCAE instrument is modelled (Figure 1) by an open-source object-oriented software library (MEGAlib [3] which provides an interface to Geant4 [4], a toolkit that simulates the passage of particles through matter. The radioactive sources are modelled as point-like mono-energetic gamma sources located at various distances and orientations with respect to the detector, emitting gamma-rays having energies in the range from 100keV to 2000keV. The simulated energy depositions are blurred according to Gaussian distributions with a FWHM that varies from 3.5% at energies around 100keV down to 1% at energies above 662keV, assumed to be in accordance with realistic energy measurements. At least one billion of gamma rays are emitted from the radioactive sources for each simulation condition.

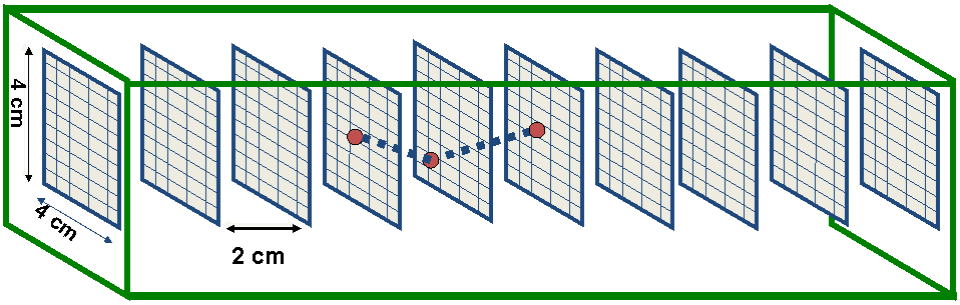

FIGURE 1. A simulated gamma-ray interacts with the COCAE detector. Three energy depositions are recorded.

Important performance parameters of the COCAE instrument such as its detecting efficiency and angular resolution have been studied by Monte Carlo in our previous work [5] as well as various techniques for the determination of the correct sequence of multiple Compton scattering interactions of the gamma rays with the detector's sensitive materials, in a wide range of incident gamma-ray energies [6], [7], [8].

The current research work aims to study the ability of the COCAE instrument to reconstruct the image of point-like radioactive sources located at different orientations and source-to-detector distances, emitting gamma-rays in a wide range of energies. Described in the following

sections is the image reconstruction algorithm used as well as the resolution of the reconstructed images.

SOURCE IMAGE RECONSTRUCTION

The process of Compton imaging refers to the generation of the image of a radioactive source by using the recorded information of the energy depositions and the positions of the interactions of many incident gamma rays with the sensitive materials of the detector. There are several algorithms that yield Compton images. For the current research work the selected imaging algorithm is the List Mode Maximum Likelihood Expectation Maximization (LM-MLEM). This technique has been originally developed for medical imaging [9] and has been wide-spread in the field of Compton imaging [6].

LM-MLEM is an iterative algorithm that converges to the source image with the highest likelihood of having produced the recorded data. It is a list mode based algorithm (LM); the data fed to the algorithm is a mere list of events (energy depositions and positions of interactions of the incident gamma rays via the Compton scattering). The list mode methods are appealing in image reconstruction because the total number of data in the list is significantly smaller than the number of possible combination of position and energy measurements.

The imaging algorithm starts the reconstruction of the image for each event at a time by using the back projection method illustrated in Figure 2, which is an algorithm that projects the Compton cone of each event onto an imaging plane. The Compton cone refers to the well known Compton scattering process: When an emitted gamma-ray interacts with the detecting materials via the Compton scattering effect, a recoil electron and a scattered photon are created in a such way so both the energy and the momentum of the scattering is conserved. The energy (E_e) and the position ($\vec{r}_1$) of the recoil electron can be quickly measured while the scattered photon ideally deposits all its energy (E_g) in the detecting materials in a series of one or more interactions before it is finally absorbed via a photoelectric interaction. (The position of an interaction is assumed to be the center of a CdTe pixel). The scattering angle (θ) is related to the energy depositions both of the recoil electron and of the scattered photon via the well known Compton formula:

$$\cos\theta = 1 - m_0c^2\left(\frac{1}{E_g} - \frac{1}{E_g + E_e}\right) \quad (1)$$

where m_0c^2 is the rest energy of the electron.

Moreover, the scattering angle is geometrically related to the direction ($\hat{r}_0$) of the incident gamma-ray via the formula:

$$\cos\theta = \hat{r}_0 \cdot \hat{u} \quad (2)$$

where $\hat{u} = \dfrac{\vec{r}_2 - \vec{r}_1}{|\vec{r}_2 - \vec{r}_1|}$

Thus, by recording the positions of the interactions ($\vec{r}_1, \vec{r}_2$) and the energy depositions (E_e, E_g), the incident direction (r_o) of the primary gamma-ray is constrained to lie on a cone (Compton cone). The Compton cone's central axis is defined by the vector u given by equation (2) connecting the two interactions whereas the cone's opening angle is equal to the Compton scattering angle defined by equation (1). The apex of the Compton cone is located at the CdTe crystal pixel in which the gamma-ray have scattered.

Since the incident gamma ray could have originated from any point on the surface of the Compton cone, during the image reconstruction, the back projection algorithm samples randomly the azimuthal angle (φ) over the full range [0,2π]. Then, each of the vectors

corresponding to a specific value of φ directed towards to the apex of the cone is projected onto multiple planes at different source-to-detector distances (z). For any given projection imaging plane, the pixels intersected by the cone form a circle scribed onto the projection plane.

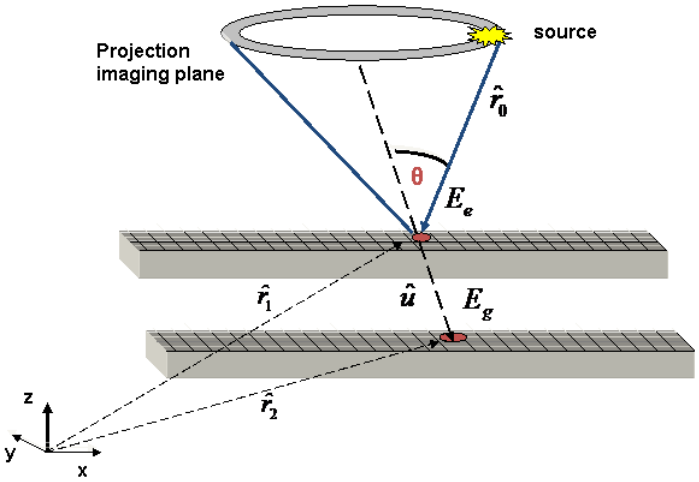

FIGURE 2. The Back projection imaging algorithm

All back projected Compton circles (each one corresponding to a different incident gamma-ray emitted by the radioactive source) intersect at a common point that determines the source location. In principle three Compton cones should be enough to reconstruct the image of a point-like radioactive source but in practice (due to measurement errors and to incomplete absorption of the scattered photon) a large number of reconstructed Compton cones are needed to derive the source location accurately (Figure 3).

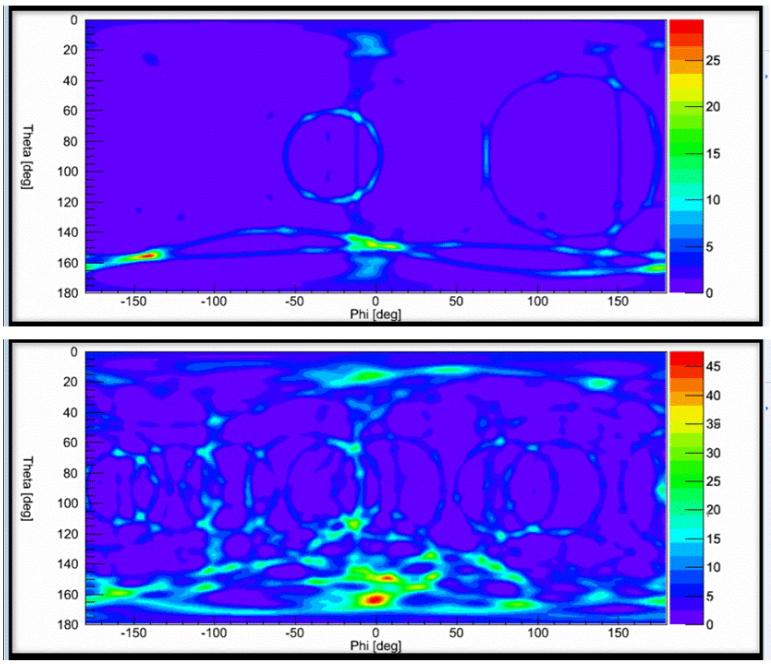

FIGURE 3. The back projected image process: as the number of events and the number of iterations increase (from top to bottom), the source image converges.

The back projected image serves as the initial estimation of the image to start the iteration procedure of the LM-MLEM algorithm. For each pixel in the image all the events having a Compton cone that touched that pixel are recorded and the pixel's sensitivity is calculated, representing the probability that a gamma ray originated by the pixel is detected anywhere in the detector. This information is fed to the LM-MLEM algorithm that uses an iterative reconstruction equation for calculating the amplitude of each pixel of the image in order to find the reconstructed image distribution with the highest likelihood of having produced the recorded data.

Figure 4 depicts the reconstructed image for the case of an 800keV point-like radioactive source using 50 iterations of the LM-MLEM imaging algorithm. The simulated source is located 50 cm from the detector's center at inclination angle $\theta=26.56^0$ and azimuth angle $\varphi=0^o$ (where $\theta=0^o$ corresponds to the detector's symmetry axis), in spherical coordinates.

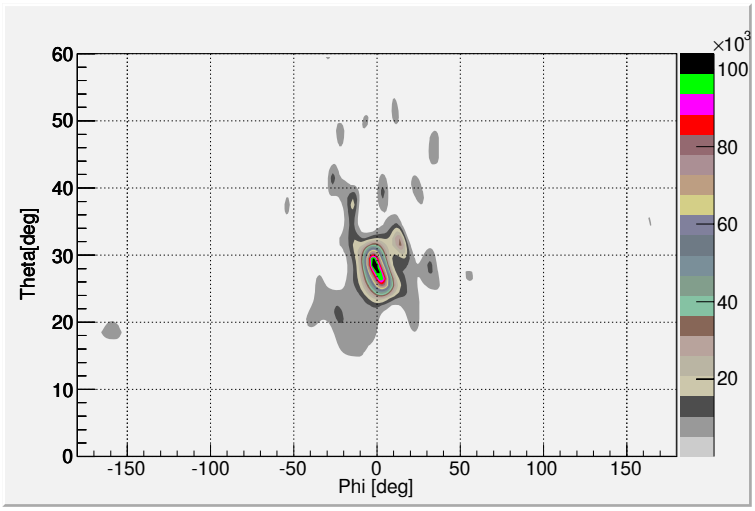

FIGURE 4. Reconstructed image using 50 iterations of LM-MLEM imaging algorithm, for the case of z simulated point-like radioactive source (800 keV) located at (θ=26.56°, φ=0°).

RECONSTRUCTED IMAGE RESOLUTION

The ability of the COCAE instrument to estimate the orientation of radioactive sources depends largely on its resolution of reconstructing radioactive sources' images. The reconstructed image resolution is defined as the combined FWHM of the azimuth (φ) and inclination (θ) profiles of the source's reconstructed image measured in steradian (sr).

We have studied the reconstructed image resolution of the COCAE instrument by considering two case conditions: point-like radioactive sources located a) on the detector's symmetry axis (z) and b) off the detector's symmetry axis.

For the evaluation of the reconstructed image resolution for various gamma-ray energies, source-to-detector distances and orientations, the same number of interactions of incident gamma rays with the detector has been assumed. This assumption can be achieved experimentally by increasing the acquisition time as a function of the source-to-detector distance.

Shown in Figure 5a and 5b are the azimuth and inclination distributions respectively (measured in degrees), for the case of an 800keV point-like radioactive source located 50 cm from the detector's center at azimuth angle $\theta=26.56^0$ and inclination angle $\varphi=0^o$.

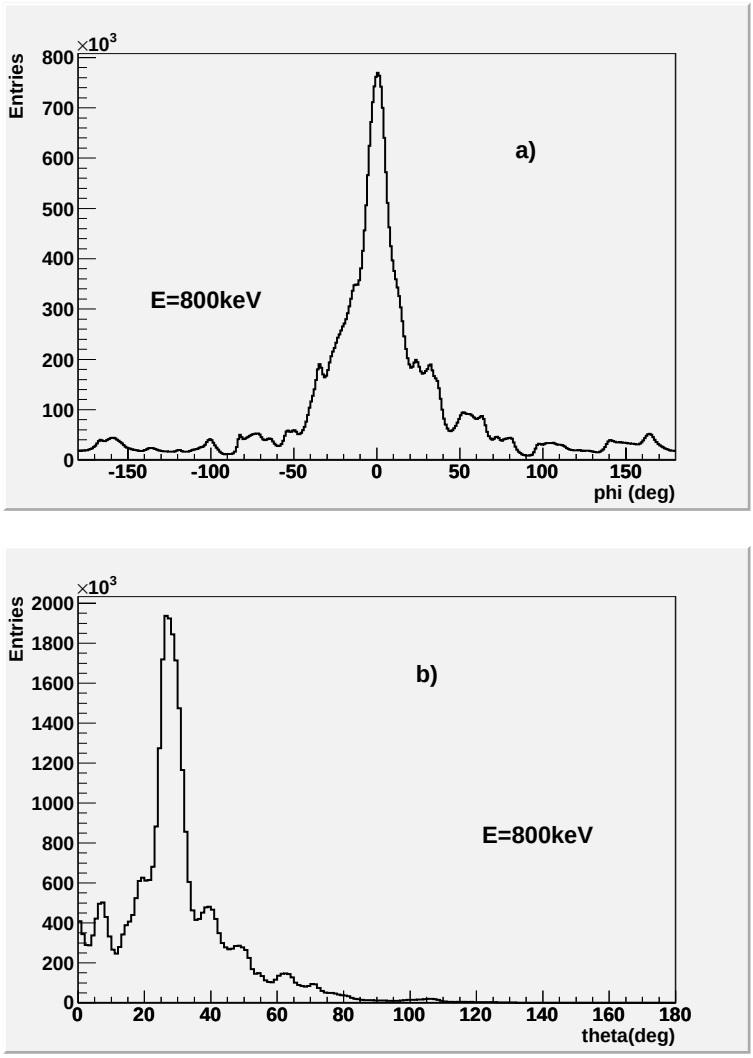

FIGURE 5. a) azimuth and b) inclination profiles of the reconstructed image of an 800keV point-like source located at (θ=26.56°, φ=0°), in spherical coordinates.

Radioactive sources located on the detector's symmetry axis

For the case of on-axis radioactive sources, our studies have been performed by simulating radioactive sources emitting gamma rays in an energy range from 100keV to 2MeV located at distances up to 2m from the detector's centre.

Presented in Figure 6 is the reconstructed image resolution (measured in steradian (sr) as a function of the source-to-detector distance for three cases of point-like radioactive sources emitting 400keV, 1000keV and 2000keV gamma rays. It can be noticed that the reconstructed image resolution increases as the source-to-detector distance is reduced; it varies from less than 2.5×10^{-3} sr (for source-to-detector distances ~50cm) down to about 0.5×10^{-3} sr (for point-like sources located at distances greater than ~1m).

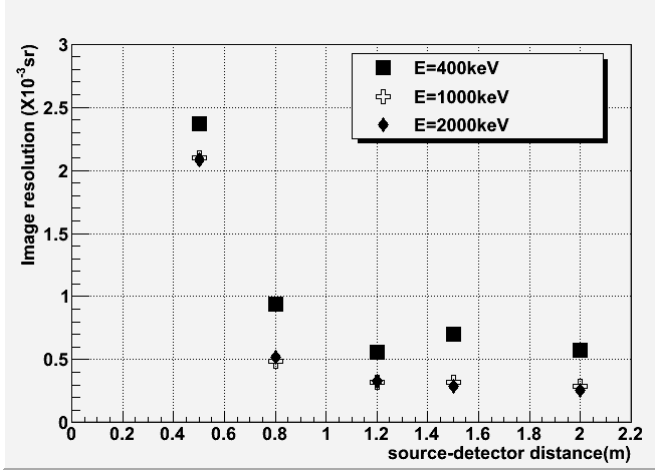

FIGURE 6. Reconstructed image resolution for point-like 400 keV, 1000 keV and 2000 keV radioactive sources located on the detector's symmetry axis, as a function of source-to-detector distance.

Furthermore, it can be seen from Figure 7 that for an arbitrary source-to-detector distance (z=80cm) and for point-like radioactive sources emitting gamma rays with energies in the range from 400keV to 2000keV, the reconstructed image resolution is less than 1x10^{-3}sr.

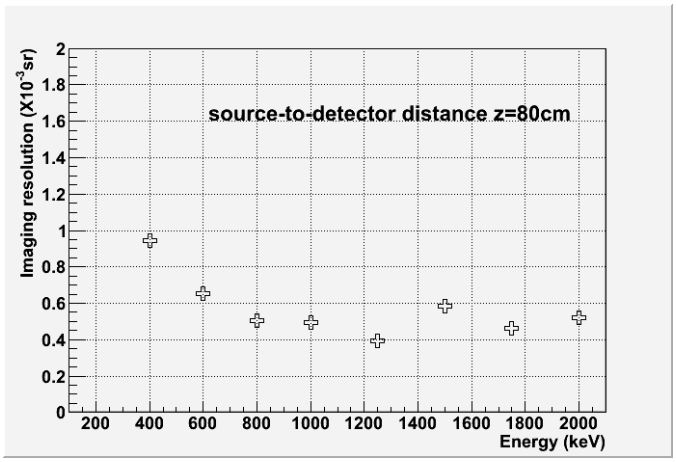

FIGURE 7. Reconstructed image resolution for point like radioactive sources located on the detector's symmetry axis as a function of the incident gamma ray energy, for an arbitrary source-to-detector distance (z=80cm).

Moreover, we have studied the dependence of the COCAE's image resolution on the number of the reconstructed events. (It has to be noticed that for the reconstruction of the source's image only a fraction of the reconstructed events is used, corresponding only to those events that interact with the COCAE's detecting elements via the Compton scattering process). Figure 8a and 8b show the azimuth (φ) and the inclination (θ) coordinate respectively of the reconstructed image, as a function of the number of reconstructed events. The simulated point-like radioactive sources emit gamma rays in the energy range from 400keV to 1250keV and they are located at an arbitrary source-to-detector distance (z=120cm), on the detector's symmetry axis (φ=180^o, θ=90^o). The solid line in Figure 8a and 8b represents the real azimuth and inclination coordinate of the simulated sources respectively, whereas the error bars correspond to the estimated FWHM of the image distributions, measured in degrees (deg). It

can be seen that a minimum number of about $5x10^3$ reconstructed events is required for a successful image reconstruction.

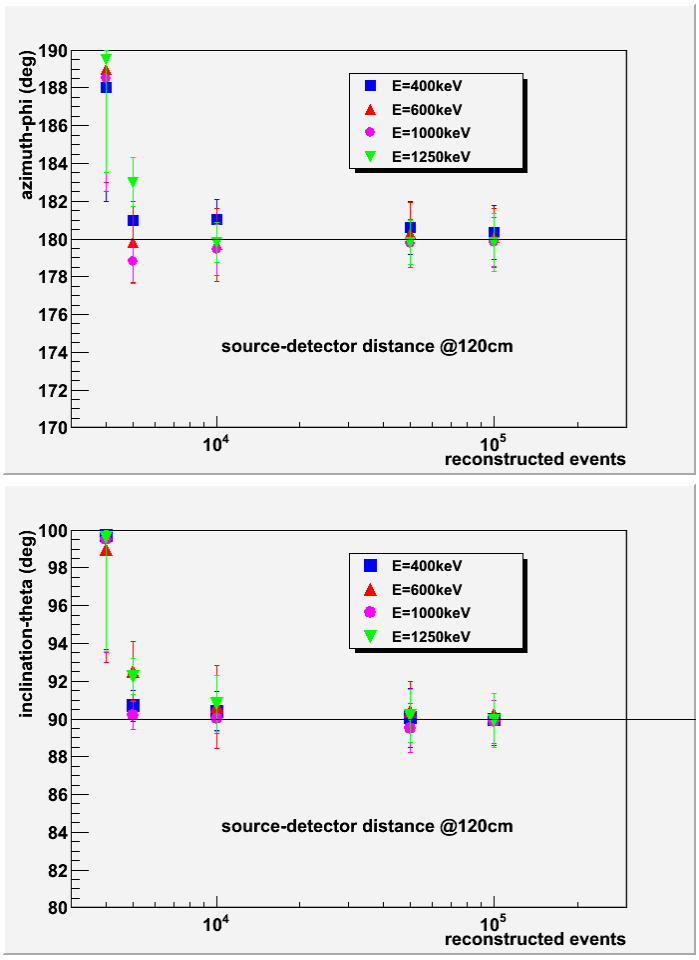

FIGURE 8: The azimuth (top) and inclination (bottom) image coordinate of point-like radioactive sources located on the detector's symmetry axis (solid line), as a function of the number of reconstructed events.

Radioactive sources located off the detector's symmetry axis

For the case of point-like radioactive sources located off the detector's symmetry axis (defined at $\varphi=0^o,\theta=0^o$) we have performed Monte Carlo studies, by simulating radioactive sources emitting gamma rays in the energy range from 100keV to 2MeV. The sources are located at 50 cm from the detector's center at azimuth angle $\varphi=0^o$ and inclination angles up to 90^o.

Figure 9 illustrates the evaluated reconstructed image resolution as a function of the incident gamma ray energy, for the case of point-like radioactive sources located at various inclination angles whereas Figure 10 shows the reconstructed imaging resolution versus the inclination angle, for 600keV, 1000keV and 2000keV radioactive sources.

It can be noticed that the reconstructed image resolution is worse compared to the case of on-axis sources being less than ~$4x10^{-3}$sr, for point-like radioactive sources emitting gamma rays with energies from 600keV to 2000keV.

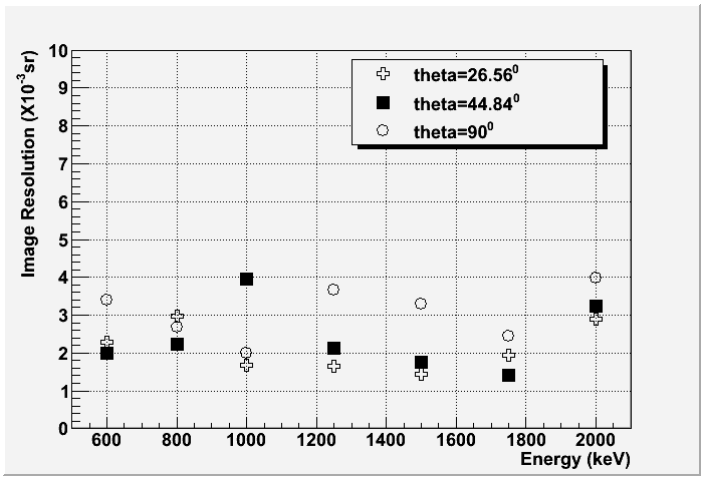

FIGURE 9. Reconstructed image resolution for point-like radioactive sources located off the detector's symmetry axis (φ=0°, θ=0°), as a function of the incident gamma-ray energy.

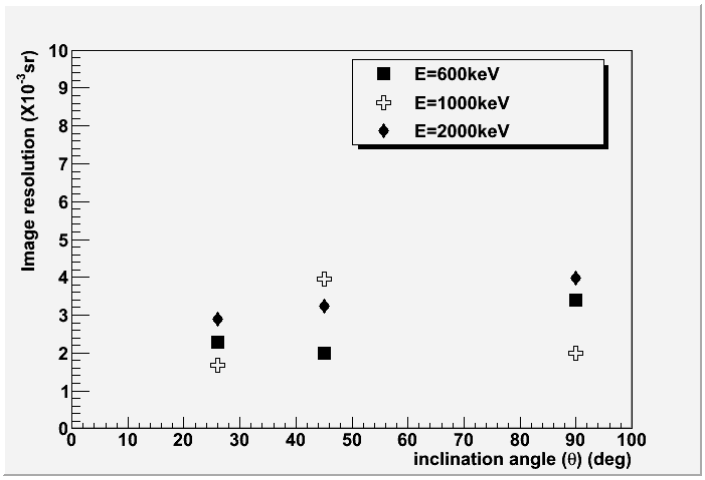

FIGURE 10. Reconstructed image resolution for point-like radioactive sources located off the detector's symmetry axis (φ=0°, θ=0°), as a function of the inclination angle (θ).

CONCLUDING REMARKS

The reconstructed image resolution of a portable pixelated CdTe detector (COCAE) has been studied by applying the LM-MLEM imaging algorithm on a large number of simulated gamma rays. The radioactive sources are modelled as point-like mono-energetic gamma sources located at various distances and orientations with respect to the detector's symmetry axis, emitting gamma-rays having energies in a broad energy range from 100keV to 2000keV.

Our studies have shown that for radioactive sources placed on the detector's symmetry axis at least five thousand reconstructed events are needed for a successful reconstruction of the source's image. Using fifty iterations of the LM-MLEM imaging algorithm, the reconstructed image resolution has been estimated to be less than ~2.5x10^{-3} sr (for source-to-detector distances ~50cm) down to ~0.5x10^{3} sr (for point-like sources located at distances greater than ~1m).

Moreover, simulation studies performed for radioactive sources placed off the detector's symmetry axis have showed that the ability of the instrument to reconstruct the image is worse than in the case of on-axis sources, being less than about $4x10^{-3}$ sr.

ACKNOWLEDGMENTS

This work was supported by the European Community's Seventh Framework Program FP7-SEC-2007-01.

REFERENCES

1. T. Kamae, R. Enomoto and N. Hanada, *Nucl. Instr. Meth. Phys. Res.* A **260**, 254-257 (1987).
2. C. Lambropoulos et al., "The COCAE Detector: An instrument for localization - identification of radioactive sources" in IEEE NSS-MIC, 17th Temperature Semiconductor Detector (RTSD) Workshop, 30 October-6 November 2010, Knoxville, Tennessee, USA.
3. Zoglauer, R. Andritschke and F. Schopper, *New Astronomy Reviews* **50**(7-8), 629-632 (2006).
4. "GEANT4. A toolkit for the simulation of the passage of particles through matter," http://geant4.web.cern.ch/geant4/.
5. K. Karafasoulis et al., "Simulated performance of a position sensitive radiation detecting system (COCAE)" in eRA-5-The SynEnergy Forum, 2010, e-Print: arXiv:1101.3881.
6. Andreas Christian Zoglauer, "First Light for the Next Generation of Compton and Pair Telescopes," Ph.D. Thesis, Max-Planck-Institute, 2005.
7. K. Karafasoulis et al., "Evaluation of Compton scattering sequence reconstruction algorithms for a portable position sensitive radioactivity detector based on pixelated Cd(Zn)Te crystals" in *Nausivios Chora* 2010, paper NCH-2010-D3, Copyright 2006-2010: Hellenic Naval Academy.
8. K. Karafasoulis et al., "Simulated performance of a position sensitive radiation detecting system (COCAE)" in IEEE 2010 Nuclear Science Symposium October 30-November 6, Knoxville Tennessee, preprint: arXiv:1101.3881.
9. S. Wilderman et al., "List-mode Maximum Likelihood Reconstruction of Compton Scatter Camera Images in Nuclear Medicine", *IEEE Trans*. Nucl. Sci. **45,** 957 (1988).

A Gamma Spectroscopic Radiation Detector for Security Purposes

K. Karafasoulis[a,b], K. Zachariadou[c,b], S. Seferlis[b], I. Kaissas[b], I. Papadakis[d], D. Loukas[d], C. Lambropoulos[e] , C. Potiriadis[b],

a. Hellenic Army Academy, 16673 Vari, Greece
b. Greek Atomic Energy Commission, Patriarxou Grigoriou & Neapoleos, 15310 Athens, Greece
c. Technological Educational Institute of Piraeus, Department of Physics, Chemistry & Material Technology, P. Ralli & Thivon 250, 12244, Greece
d. National Centre for Scientific Research "Demokritos" , Institute of Nuclear Physics, 15310 Athens, Greece
e. Technological Educational Institute of Chalkida, Psachna Evias 34400, Greece

Abstract. We present the development of a stacked gamma radiation detecting system, consisting of three layers of pixelated Cadmium Telluride detectors (PID350). A high speed (120 frames/s) data acquisition system has been developed in order the system being able to compete with high flux of gamma rays. The PID350 detector's photo-peak energy resolution ranges from 1.73 keV to 2.15 keV (FWHM) at 59.5 KeV. Spectroscopic measurements performed have shown that the stacked detecting system is able to accurately evaluate the position of a 140.5 keV radioactive source located at distances in the range from 30 cm to 1 m.

Keywords: Semiconductor detectors, Gamma-ray spectroscopy, CdTe diode detector
PACS: 29.40.Wk, 29.30.Kv

INTRODUCTION

The last decades, the world's growing interest in homeland security has given new impetus to the efforts of the scientific community to improve gamma radiation detection technologies. Within this research field, the current work aims to explore the ability of a radiation detecting system under development to identify both the energy and the source-to-detector distance of gamma radioactive sources. The system consists of three planar pixelated Cadmium Telluride (CdTe) semiconductor detectors (PID350) stacked together.

Pixelated detectors have the advantage of providing accurate information on both the energy deposition and the position of each interaction of gamma radiation with the detecting materials. Moreover, by choosing the geometry of a stacked detector (in which thin layers are stacked together), the efficiency of detecting the gamma rays is increased and more information about the original gamma radiation can be extracted (since successive interactions with the detecting layers are recorded).

Described in the following sections is the general structure of a PID350 radiation detector, its calibration procedure as well as the high speed readout system developed so that the detector

being able to compete with high flux of gamma rays. A prototype stacked system consisting of three PID350 detectors is presented as well as results on its ability of estimating the position of point-like gamma sources.

THE PID350 DETECTOR

For the development of the gamma radiation stacked system, PID350 detectors provided by AJAT [1] have been used. PID350 is a pixelated detector based on CdTe-CMOS technology, suitable for gamma and X-ray detection (Figure 1). Its active area is 4.5 cm x 4.5 cm and consists of eight CdTe-CMOS hybrid elements. Each hybrid element has 2048 radiation sensing pixels of 350μm size, thus a PID350 detector consists of 16384 pixels. Each pixel is capable of recording the energy deposited of every detected interaction. The maximum energy deposited in each detector pixel during two successive readout cycles is stored into a specific address in a local memory.

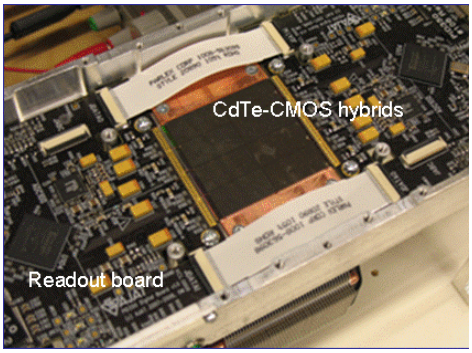

FIGURE 1. The PID350 pixelated detector.

The eight CdTe-CMOS hybrid elements of a PID350 detector are grouped into two modules each one connected to a digital control board having individual power supply and data readout (Figure 2). During one readout cycle, the contents of all the 8192 pixels of one PID350 module are read and stored in the computer forming a frame. The data are transferred from the control board of each module directly to a PC station through a Serial Peripheral Interface (SPI) bus.

In the present work three PID350 detectors have been used for spectroscopic measurements and their performance has been evaluated in order to be used in a stacked prototype system under development. The detectors are labeled as PID350#1, PID350#2 and PID350#3. The two modules of each detector are labeled with a subscript (e.g. the PID350#1 detector consists of the PID350#1_1 and PID350#1_2 modules).

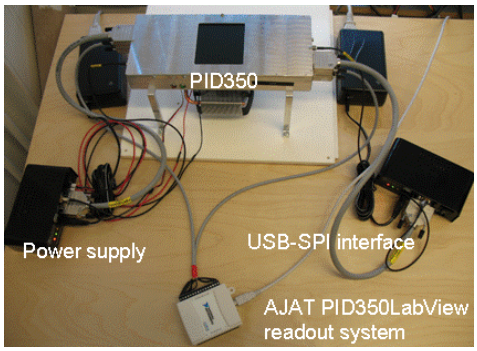

FIGURE 2. The PID350 system.

CALIBRATION

The hardware calibration procedure of a PID350 detector concerns the adjustment of both the offset and the gain parameters of each pixel. The calibration has been performed by using the PID350 standard data acquisition system provided by AJAT, having a maximum data rate transfer of 2 frames/s and a graphical user interface based on LabView.

For the offset adjustment, noise data have been collected in order to locate the noise peak of each pixel. Several iterations are needed in order to reduce the width of the noise peak to no more than two channels.

For the gain adjustment, data have been collected for each PID350 detector using a ^{241}Am radioactive source. The gain adjustment procedure searches for the gamma peak location and corrects the gain parameters in order to align the gamma peaks of all pixels. Several iterations have been performed in order to squeeze the distribution width of the gamma peak positions (centroids) of each pixel to no more than two channels.

Since the offset and gain adjustments are not completely independent, they have been repeated iteratively several times, in order to reduce the FWHM of the cumulative gamma ray spectrum.

The cumulative spectrum of ^{241}Am radioactive source calibration is shown in Figure 3 before and after the hardware calibration, for the case of the detector PID350#3. Similar spectra have been obtained for PID350#1 and PID350#2 detectors.

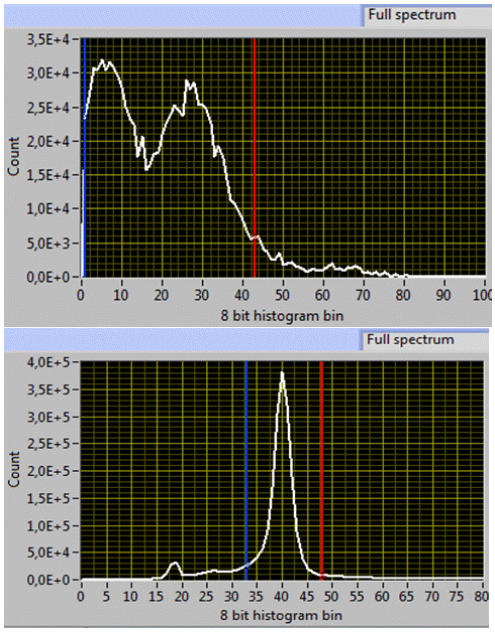

FIGURE 3. Cumulative spectrum of a ^{241}Am radioactive source recorded by the PID350#3 detector, before (up) and after (down) the adjustment of the offset and gain parameters of all its pixels.

.

A HIGH SPEED READOUT SYSTEM

The read out of the PID350 detector, provided by AJAT is slow compared to the internal memory writing speed resulting to data loss during the collection of data. In order to reduce the data loss we have developed a new high speed readout system (Figure 4) consisting of an

FPGA SPI, a High Speed USB and a user interface software written in VHDL and C languages. This system manages to increase the data transfer speed to the PC from 2 frames/s, which was the data transfer speed of the standard PID350 readout system to 120 frames/s.

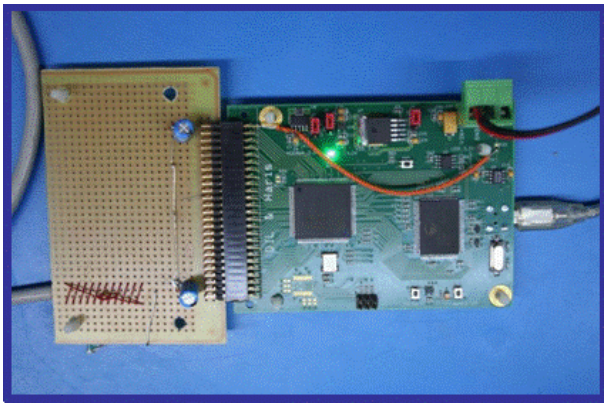

Figure 4. The high speed PID350 readout system.

The user interface software of the high speed readout system checks the PID350 status, uploads the offset and gain parameters derived by the hardware calibration procedure described in the previous section and starts the data gathering.

The raw data recorded are stored in binary data files in a stream of bytes which are grouped in 8-byte packets. Each packet stores the content of a single pixel from every PID350 module. This leads to a high data rate of 112.5 Mbytes/min. In order to manipulate the raw data with greater flexibility a software package has been developed under the ROOT framework [2]. The software transforms the raw data packets into usable frames and stores them in ROOT format. A frame holds an identification number for the frame (ID), the signal amplitude collected by each pixel, the spatial coordinates of each pixel and a sequence number which carries an estimation of the time when the interaction occurs. Furthermore, the software checks the energy resolution, the number of bad pixels and the upper channel limit of the noise peak.

ENERGY RESOLUTION

Although the width of the distribution of the photo-peak centroids has been adjusted to be no more than two bins during the hardware calibration of the PID350 by using a ^{241}Am source (as described previously), it becomes much wider when the detector is irradiated by a different mono-energetic gamma source. This is evident in Figures 5a and 5b illustrating the photo-peak centroid distributions of all pixels of the PID350#3 detector, when irradiated by an ^{241}Am and ^{109}Cd radioactive source respectively (the bad pixels are excluded). The broad distribution of the photo-peak centroids results to a broad energy peak in the energy spectrum, since the energy peak is the convolution of the width of each pixel's photo-peak with the distribution of the photo-peak centroids.

In order to improve the energy resolution of the cumulative spectra, the PID350 detectors have been irradiated by two known energy sources and a software energy calibration procedure has been developed. According to this procedure, a total of 8192 histograms (one per each pixel) are created dynamically and are filled with the content of the corresponding pixel, creating in this way the spectrum of each pixel. Then, the peaks of every single pixel spectrum above the dc level are searched and two calibration constants are determined for each pixel based on the position of the two peaks.

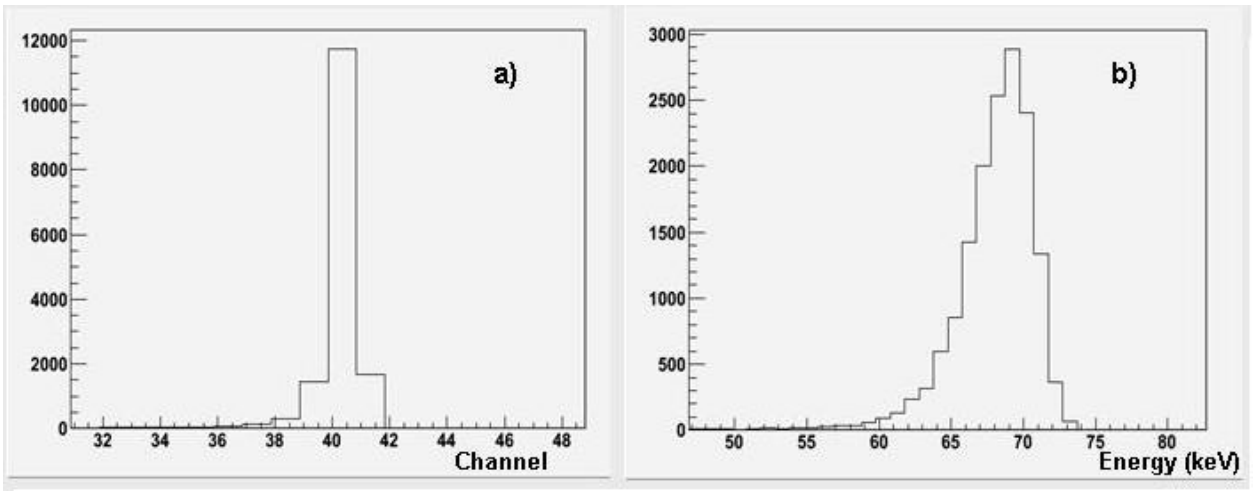

FIGURE 5.. The PID350#3 centroid channel distribution for (a) ^{241}Am and (b) ^{109}Cd sources.

To improve further the energy resolution, the software does not use in the energy calculation process the "bad" pixels. The bad pixels are defined as those pixels for which the energy calibration procedure either fails (the calibration algorithm can't find two peaks in order to calibrate the pixel), or the pixel is noisy (it has noisy channels above the upper edge of the dc level).

The energy calibration has been performed for each PID350 detector, using two low energy gamma ray standard isotopes: ^{241}Am (59.5keV) and ^{109}Cd (88keV). Figure 6 illustrates the spectrum of the PID350#3 detector before and after the software energy calibration.

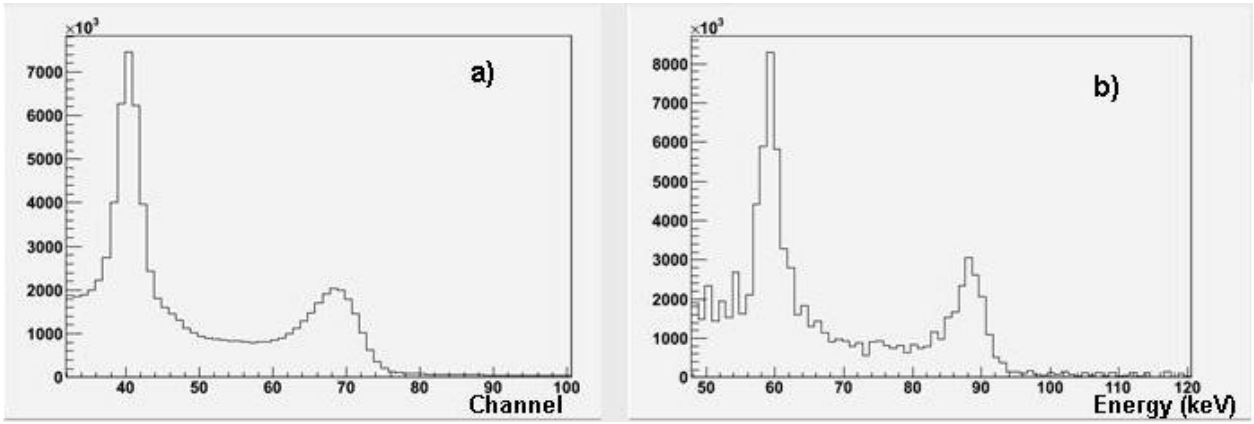

FIGURE 6. a) The un-calibrated spectrum of the PID350#3 detector (b) The calibrated spectrum after a pixel by pixel adjustment.

Moreover, the calibrated ^{241}Am photo-peak of each PID350 detector after the software calibration is shown in Figure 7. The archived energy resolution at 59.5 KeV ranges 1.73 keV to 2.15 keV (FWHM)

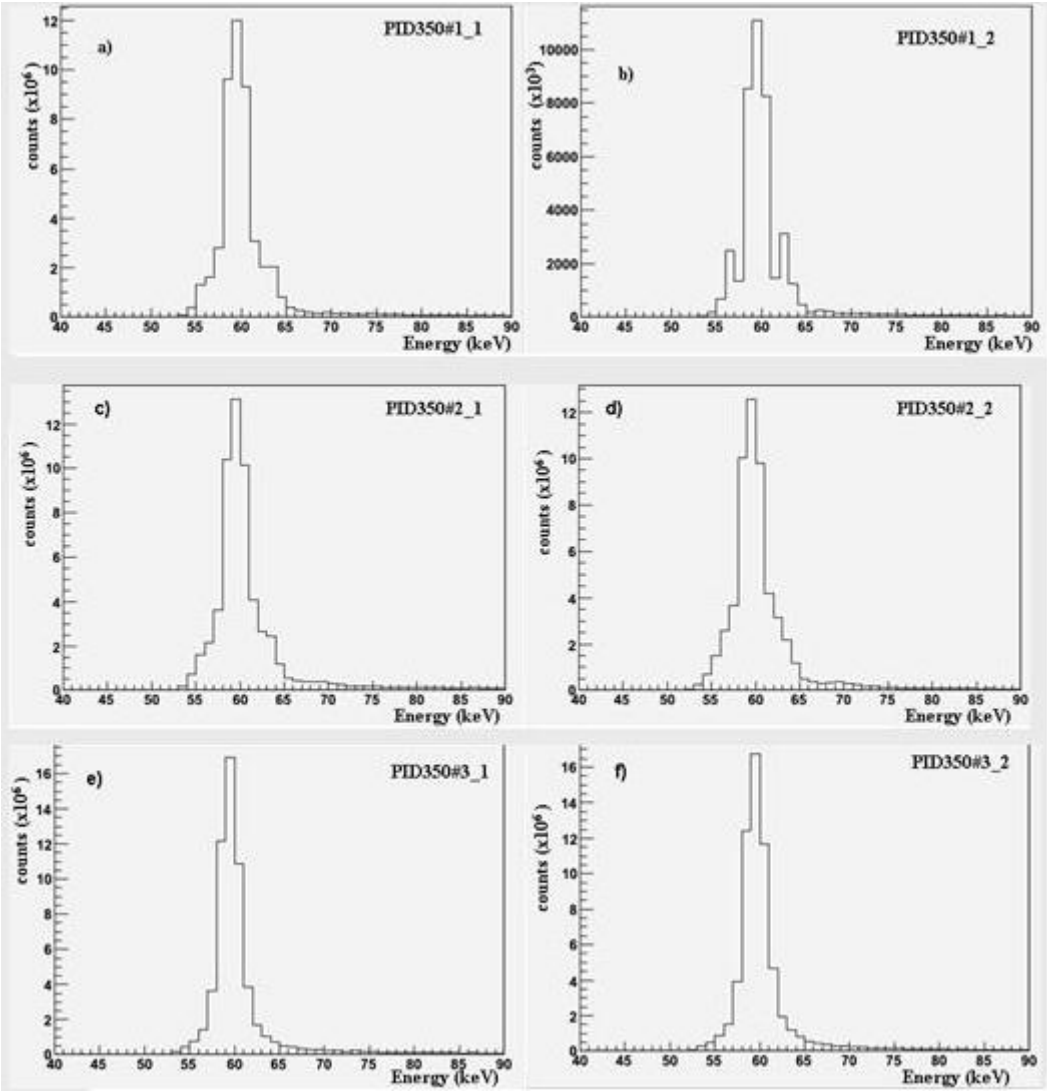

FIGURE 7. Calibrated photo-peaks of ^{241}Am radioactive source acquired with a) PID350#1_1, b) PID350#1_2, c) PID350#2_1, d) PID350#2_2 e) PID350#3_1 and f) PID350#3_2 detector modules.

THE STACKED PROTOTYPE SYSTEM

The Structure of the System

We have assembled a prototype system as a stack of three PID350 detectors. The ordering of the PID350 layers in the stacked system reflects the performance of each layer, i.e. the PID350s are stacked from the top to bottom with decreasing quality. The quality is defined by three parameters: the energy resolution, the number of bad pixels and the upper channel limit of the noise peak. The experimental setup used to test the performance of the prototype system is shown in Figure 8. For the data acquisition the system described in the previous section has been used.

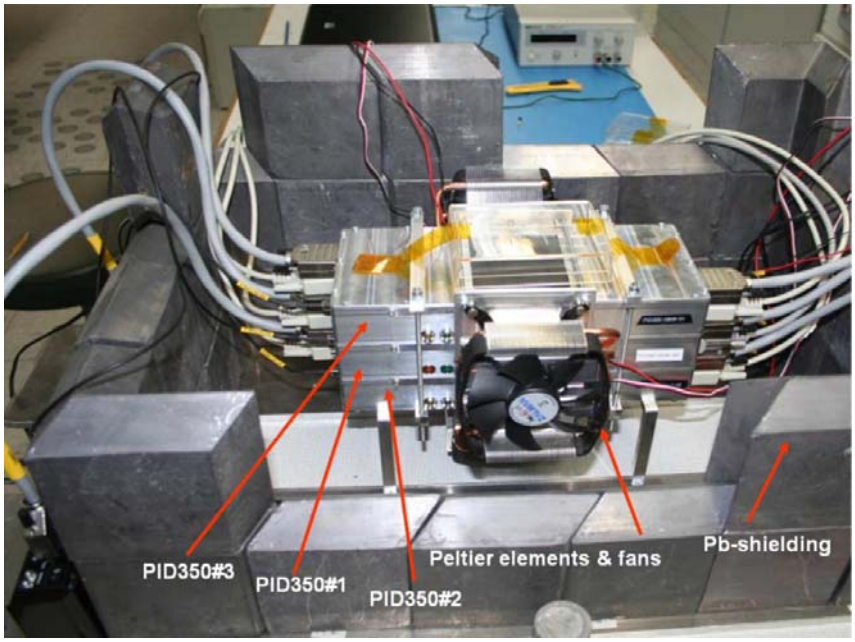

FIGURE 8. Experimental setup with the PID350 stacked prototype.

Simulation Studies

The response of both the PID350 detector and of the stacked system has been modeled using an open-source object oriented software library (MEGAlib [3]) providing interface to the GEant4 [4] toolkit that simulates the passage of particles through matter.

A large number of gamma rays (~10^9) emitted from point-like isotropic sources placed on the detector's axis of symmetry and at different distances interact with the PID350 detector model and the deposited energy is smeared using a Gaussian distribution of 7keV FWHM [1]. Shown in Figure 9 is the case of a simulated event of a 10keV gamma ray that interacts with the model of the stacked system creating two energy depositions (hits).

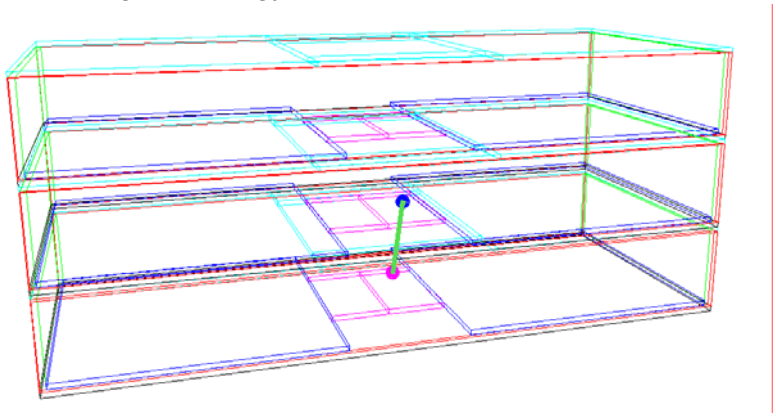

FIGURE 9. An 140 keV gamma ray interacts with the stacked system creating two hits (energy depositions).

Shown in Figure 10 is the simulated energy deposition of all hits for the case of 60 keV incident gamma rays. The peak (59.5 keV) due to interactions of the gamma rays with the detecting materials via the photoelectric effect process, the Ka x-ray from Cadmium (23 keV)

and the escape peak (26.5 keV), broadened due to the smearing, are visible.

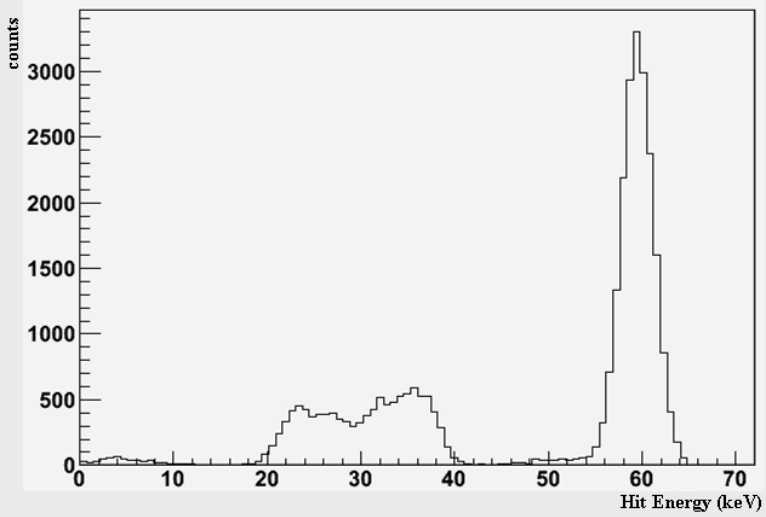

FIGURE 10. Simulated spectrum of the energy deposited in each PID350 detector pixel, for 60 keV incident gamma rays

Source-to-detector distance Estimation

The ability of the stacked detector to estimate the distance of a radioactive source has been tested by using a ^{99m}Tc (140.5 keV) source placed at various distances from the system's upper detecting layer. The estimation of the source-to-detector distance is based on the distribution of the fully absorbed photons (via a photoelectric effect) in each detecting layer [5].

The distance (d) of a radioactive source from the first detecting layer of the stacked system is evaluated by fitting the following function on the distribution of the photo-peak counts (N_i) of each PID350 detector layer (i):

$$N_i \propto \exp\left(-(i-1)\left(\sum_j \mu_j t_j\right)+a\right)\cdot\frac{\sin^{-1}\left(\dfrac{k^2}{[d+(i-1)g]^2+k^2}\right)}{\sin^{-1}\left(\dfrac{k^2}{d^2+k^2}\right)} \quad (3)$$

where t_j is the thickness of a material of each detecting PID350 layer with corresponding total absorption coefficient μ_j, g is the distance between the layers, k is half the length of the rectangular layer side and α is a parameter evaluated experimentally. The sum runs over all materials of the i^{th} layer.

The first term of the above equation reflects the absorption by the front layers of the detector. The second term is the ratio of the solid angle subtended by the i^{th} rectangular detecting layer over the solid angle subtended by the first one. Experimental results for the determination of the distance (d) by using a ^{99m}Tc radioactive source are presented in Figure 11. It can be noticed that the 3-layer PID350 stacked prototype system is capable of evaluating the distance of a gamma ray source with good accuracy in the distance range from 30 cm up to 100 cm.

Additionally, the complete geometry of the stacked PID350 detecting system has been simulated using the GEANT4 package and the estimated distance using the simulated data is

depicted in Figure 11 for the case of a 140.4KeV radioactive point-like source (^{99m}Tc). The solid line represents the case of the ideal source-to-detector distance estimation.

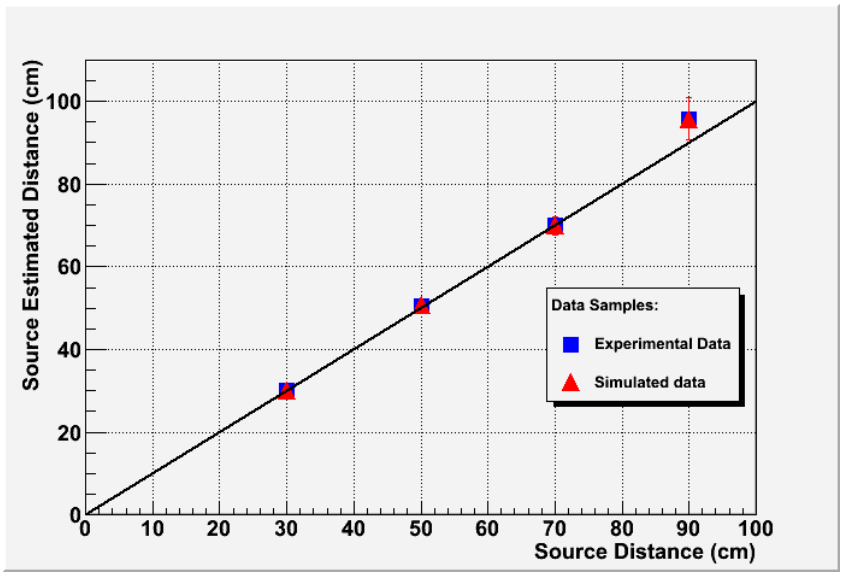

Figure 11. Estimated distance vs. real distance of a ^{99m}Tc radioactive source using both real and simulated data.

SUMMARY

We have developed a prototype stacked system consisting of three PID350 pixelated detectors.

In order to reduce the data loss in case of a high flux of photons, we have developed a data acquisition system with data transfer speed of 120 frames/s.

Furthermore, we have developed a data analysis framework that transforms the raw data collected by the PID350 detectors into useable frames and performs a software energy calibration for each pixel of the detector independently. The achieved energy resolution ranges from 1.73 keV to 2.15 keV (FWHM) at 59.5keV.

Spectroscopic measurements show that the stacked system is able to accurately evaluate the distance of a ^{99m}Tc radioactive source from its first detecting layer, in a broad range of source-to-detector distances from 30cm to 1m.

REFERENCES

[1] AJAT, http://www.ajat.fi/index.php?option=com_content&view=article&id=37
[2] ROOT Data Analysis Framework, http://root.cern.ch
[3] Zoglauer, R. Andritschke, F. Schopper: “MEGAlib-The Medium Energy Gamma-ray Astronomy Library”, New *Astronomy Reviews*, Volume 50, Issues 7-8, Pages 629-632, October 2006
[4] GEANT4-A toolkit for the simulation of the passage of particles through matter, http://geant4.web.cern.ch/geant4/
[5] Shin Watanabe et al. “Stacked CdTe gamma-ray detector and its application to a range finder”. Nuclear Instruments & Methods in Physics Research A 505(2003)118-121

Carbon Nanotubes: Fabrication, properties and applications

A.P. Markopoulos[a], V.N. Stavrou[b], G.P. Veropoulos[b] and G. Boumpoukiotis[a]

[a]*Division of Academic Studies, Hellenic Navy Petty Officers Academy, 12400 Skaramagkas, Greece*
[b]*Division of Physics, Hellenic Naval Academy, 185 39 Hadjikyriakou, Piraeus, Greece*

Abstract. Carbon nanotubes are in the forefront of nanomaterials research since their discovery last decade. These carbon molecules are tiny tubes with diameters down to 0.4 nm, while their lengths can grow up to a million times their diameter. In this paper the most common fabrication methods for Carbon Nanotubes are explained and their remarkable properties are portrayed, namely mechanical, electrical and electronic properties. Finally, some applications of Carbon Nanotubes based on the aforementioned properties are discussed.

Keywords: Nanotubes, Electric arc discharge, Laser ablation, Chemical vapour deposition, phonons.

PACS: 78.67.Ch, 61.46.-w, 65.80.-g, 72.10.Di, 74.25.Kc.

1. INTRODUCTION

In the past few years nanostructured materials, with dimensions of grain size, layer thickness or shapes, below 100 nm, are of special interest. This wide group of materials enables access to new ranges of electronic, magnetic, mechanical or optical properties. Polycrystalline materials with grain sizes less than a few nanometres possess properties different from classic materials, because they are relatively highly affected by the grain boundaries. For example they appear to be very strong and highly wear resistant coatings are being developed out of these materials. Furthermore, researchers at IBM used magnetic nanoparticles within several ultra-thin layers to develop advanced data storage devices. Sensors for disk-drives have been developed with many times the sensitivity of previous devices, allowing more bits to be packed on the surface of each disk. Nanoscale structures can potentially store trillions of bits of data per square inch, giving them a capacity 10 to 100 times greater than that of present memory devices.

Nanotubes belong to the promising group of nanostructured materials. Although nanotubes based on boron nitride and molybdenum are reported, Carbon Nanotubes (CNTs) are by far the most important group. These tubes contain one or several concentric graphite layers with diameters in the range of 0.4 nm up to tens of nanometres.

The discovery of the “buckyball”, i.e. a football shaped C60 molecule, reported by Kroto et al. in 1985 [1], had a strong impact and marked the beginning of a new era in carbon material science. In 1991, Iijima discovered the carbon nanotube [2]. In the soot at the negative electrode of an arc discharge little tubes mixed with a large amount of other forms of carbon were found. Such multi-walled carbon nanotube (MWNT) contained 2 to 50 concentric cylindrical graphite sheets with a diameter of 3-10 nm and a length of up to 1 μm. This initial work led many groups throughout the world to produce and purify nanotubes. Soon it became clear that nanotubes have unique electronic and mechanical properties that are expected to lead to breaking industrial applications. Later on, single-walled carbon nanotubes (SWNT) were developed. Because of adhesive forces nanotubes often bunch to form ropes. The tubes can either be open-ended or have caps formed from half a C60 molecule at either end, see Fig. 1.

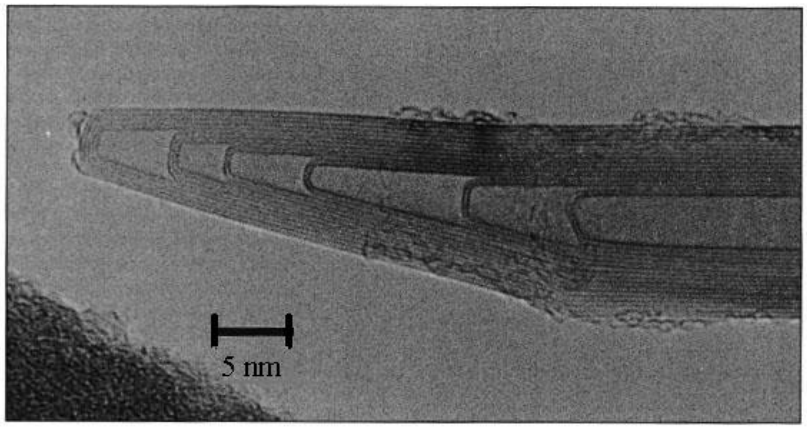

FIGURE 1. High resolution TEM image of the end of a typical nanotube showing several concentric layers with caps at the end.

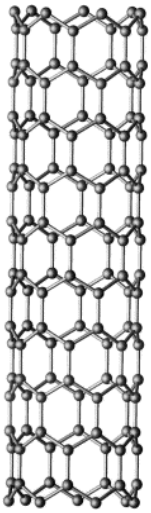

FIGURE 2. Ball-stick model of a nanotube; the balls represent the carbon atoms and the sticks their bonds [3].

To explain the carbon structure in nanotubes, the difference between diamond structure and that of graphite may be considered, see Figs. 2 and 3. In diamond, each carbon atom is attached with four others in a three dimensional lattice, which gives diamond its strength. On the other hand, in graphite, each carbon atom is attached to three others in a plane and form a hexagonal lattice, whilst the remaining bond is used to hold the planes above and below. The bonds in the plane are stronger than in diamond, but the interplanar bonds are relatively weak, and provide to the planes the possibility to slide. Therefore, whereas diamond is isotropic, graphite is anisotropic.

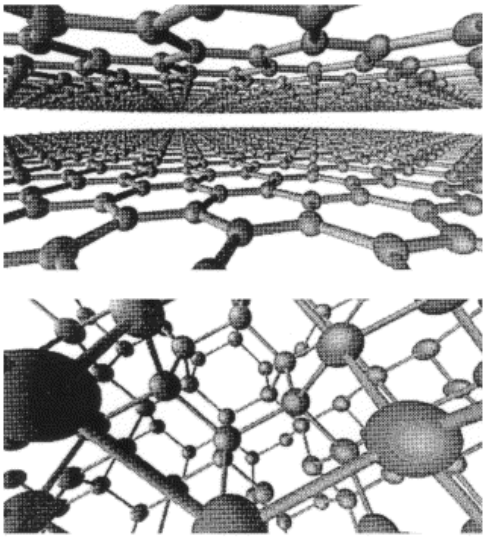

FIGURE 3. Differences between graphite (top) and diamond lattice (bottom) [3].

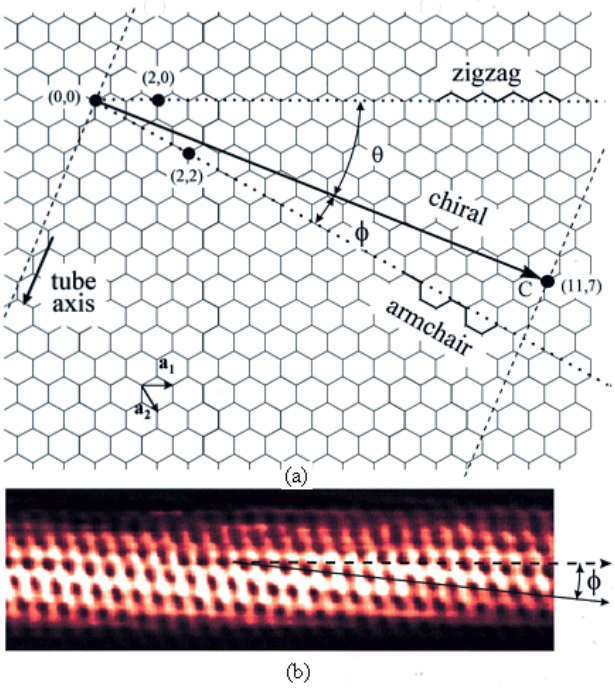

FIGURE 4. (a) The carbon lattice and the ways it can be rolled up to form a zigzag, an armchair or a chiral tube, depicted with its chiral angle; the atom at position (11,7) is projected on (0,0) like all the other atoms on the dotted line to form a tube. (b) STM image of the (11,7) chiral tube [5].

The structure of a nanotube is similar to that of graphite, with the difference that the sheets are closed to form a tube. In the ideal case, a CNT consists of either one cylindrical graphite sheet (single-walled nanotube) or several nested cylinders (multi-walled nanotube) with an interlayer spacing of 0.34-0.36 nm that is close to the typical spacing of graphite. The C-C bonds have a length of 0.14 nm, which is indeed shorter than the bonds in diamond, indicating that the material is even stronger than diamond [4]. Assuming that the a CNT is produced by the rolling of the hexagonal lattice, a few options exist. The sheet can be rolled-up along one of the symmetry axis, subsequently, either a zigzag tube or an armchair tube can be fabricated, see Fig. 4. It is also possible to roll-up the sheet in a direction that differs from a symmetry axis, therefore a chiral nanotube can be obtained. Besides the chiral angle, the circumference of the cylinder can also vary. By considering the rolling-up of the sheet as the “placement” of the atom at (0,0) on the atom at (n,m), tubes can be classified using this pair of integers, see Fig. 4; the roll-up vector (n,m) specifies the oriented width, recording the number of steps along the a and b directions.

2. CNTS FABRICATION

When heated, carbon atoms recombine in soot, some in amorphous blobs, but others in football-shaped spheres or in long cylindrical capsules. A notable progress has been made in the synthesis of these carbon nanotubes. In general, there are three ways to make soot that contains a reasonably high yield of nanotubes: electric arc discharge (EAD), laser ablation (LA) and chemical vapour deposition (CVD).

2.1 Electric arc discharge

The first identified nanotubes were fabricated by a direct current electric arc discharge (EAD) between carbon electrodes within a noble gas, like argon or helium [1, 6]. In this process, the carbon electrodes are placed a few millimetres apart and the current of approximately 100 A vaporises the carbon into hot plasma, some of which recondenses in the form of CNTs. Note that, the nanotubes form only where the current flows, i.e. on the larger negative electrode. The voltage of about 20 V, maintains a high temperature of 2000-3000 °C [7].

The typical yield of nanotubes is up to 30% by weight. The tubes have diameters between 2 and 20 nm and tend to be short, i.e. 50 μm or less, deposited in random sizes and directions; the typical rate of deposit is about 1 mm/min. It is to be noted that, an addition of a small amount of transition-metal powder, like cobalt, nickel or iron to the rods, favours the growth of single-walled nanotubes. The metal serves as a catalyst, preventing the growing tubular structures from wrapping around and closing into a smaller fullerene cage. The presence of a catalyst also allows for reducing the temperature. Without such cooling, the arc is too hot, and the nanotubes coalesce and merge rapidly into disorder; to minimise this effect a water-cooled cathode may be used [8].

2.2 Laser ablation

Single walled nanotubes (SWNT) can be efficiently produced by laser ablation (LA) of a graphite rod. These highly uniform tubes have a greater tendency to form aligned bundles than those prepared using arc-evaporation. With this method, SWNTs were generated consisting of CNTs, mostly of the armchair type, over 70% of the volume of material, bundled together into crystalline ropes of metallic character [9]. These ordered nanotubes are prepared by the laser

vaporisation of a carbon target in a furnace at 1100-1200 °C, a much lower temperature than was previously necessary for fabricating CNTs. A cobalt-nickel catalyst assists the growth of the CNTs, presumably because it prevents the ends from being “capped” during synthesis. By using two laser pulses, growth conditions can be maintained over a larger volume and for a longer time. This scheme provides more uniform vaporisation and better control of the growth conditions. The diameter range of the tubes can be controlled by varying the reaction temperature. Flowing argon or nitrogen gas sweeps the nanotubes from the furnace to a water-cooled copper collector placed just outside of the furnace. A disadvantage of this method is that it requires expensive lasers.

2.3 Chemical vapour deposition

Despite the described progress of synthetic techniques for nanotubes, there still remained two major problems in their synthesis, i.e. large scale and ordered synthesis. But, in 1996 a chemical vapour deposition (CVD) method emerged as a new candidate for nanotube synthesis [10]. The method was used to produce a 50 μm thick film of CNTs that were highly aligned perpendicular to the surface. This method is capable of controlling growth direction on a substrate and synthesising a large quantity of nanotubes. In this process a mixture of hydrocarbon gas, acetylene, methane or ethylene and nitrogen is introduced into the reaction chamber. During the reaction, nanotubes are formed on the substrate by the decomposition of hydrocarbon at temperatures 700-900°C at atmospheric pressure [11]. The process has two main advantages: the nanotubes are obtained at much lower temperature, although this is at the cost of lower quality, and the catalyst can be grown on a substrate, which allows for the formation of novel structures.

2.4 Purification of CNTs

The three different methods of the production of nanotubes suffer some serious limitations; all produce mixtures of nanotubes and nanoparticles sticking together in larger lumps. The tubes have a wide range of lengths, many defects and a variety of twists to them. Therefore, the main concern is how to separate them of the worthless soot and how to purify the tubes. Various post-growth treatments have been developed to purify the tubes and also to eliminate the defects in the tubes. The material can be treated in an ultrasonic bath to free many tubes from the particles that are originally stuck together [6]. The larger contaminants can be easily removed due to their relatively high weight, for example by dispersing the powder in a solvent and subsequent centrifugation. The smaller particles are more difficult to eliminate. One possibility for MWNTs is to perform an oxidative treatment, either by heating the powder in air at 650 °C or by a liquid phase treatment in acidic environment. For SWNTs, standard methods to eliminate catalyst particles and amorphous carbon involve re-fluxing the raw material in acid followed by centrifugation or cross-flow filtration.

Another possibility for purification is to employ physical methods that do not damage the tubes, but separate the objects as a function of their size. For MWNTs, a purification method that uses the properties of colloidal suspensions has been developed. Smaller objects remain dispersed while larger particles form aggregates that are deposited as sediment after a few hours. A related method, the size-exclusion chromatography, was successfully used for the purification and size selection for MWNTs. Purification procedures for SWNTs without any acidic treatment have also been reported and involve microfiltration or size-exclusion chromatography [4].

A method to eliminate the defects in CNTs is by annealing at high temperatures, up to 3000 K; during this process, impurities and defects in the tubes are eliminated.

3. CNTS PROPERTIES

CNTs exhibit properties that can find several uses and applications. Their mechanical, electrical and electronic properties will be hereafter discussed.

3.1 Mechanical properties

The mechanical properties of CNTs are difficult to be measured due to their small dimensions. However, different methods have been used. The Young's modulus of elasticity was estimated after measuring the thermal vibrations of nanotubes; a very high average value of 1.8 TPa was found [12]. Wong et al. [13] used a scanning force microscope to bend nanotubes that were mechanically fixed at one end. By measuring vibrations of nanotubes in an electrical field, Poncharal et al. [14] found a value below 1 TPa. This is true both for multi-walled and single-wall nanotubes because the modulus is mainly determined by the carbon-carbon bonds within the individual layers.

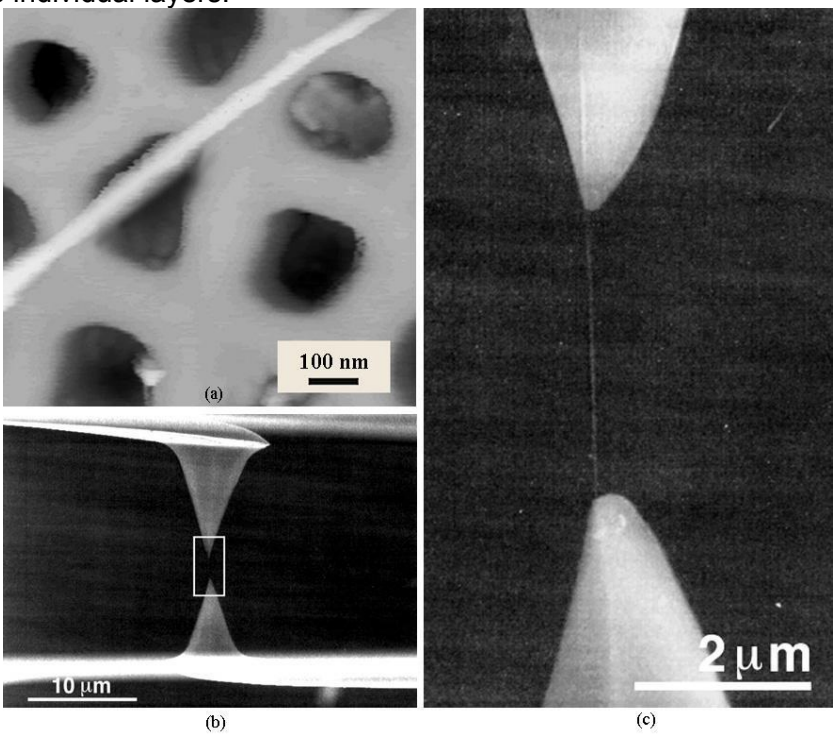

FIGURE 5. (a) An AFM microscope of a multi-walled nanotube across a pore to measure its Young's modulus by bending it with an AFM tip (b) and (c) SEM images of a multi-walled nanotube held between two AFM tips to measure its tensile strength.

Salvetat et al. [15] found that multi-walled nanotubes grown by arc discharge had a modulus of about 1 TPa, whereas those grown by the catalytic decomposition of hydrocarbons had a modulus that was smaller by one to two orders of magnitude. The nanotubes were placed across "nanopores" and an atomic force microscope was used to bend them in the middle. These results demonstrate that only highly ordered and well-graphitised nanotubes have a stiffness comparable to graphite, whereas those grown by catalytic decomposition are weaker because of their defects, see Fig. 5 (a) [15]. Further insights into the mechanical properties of multi-walled nanotubes are reported in Ref. [16]. The ends of a multi-walled nanotube were attached to a pair of AFM tips and stretched it until it broke, see Fig. 5 (b) and (c). The tips of the tubes were attached on the AFM tips by electron beam deposition of carbonaceous material. A

tensile strength of the nanotubes, ranged from 11 to 63 GPa was obtained; for comparison, high strength steel alloys break at about 2 GPa. The Young's modulus ranged from 270 to 950 GPa [16]. In this process, the AFM tips only make contact with the outside of the CNTs, so the outermost layer carries most of the load. The outermost tube ruptures at the tensile limit and slides over the inner tubes in the so-called "sword-in-sheath" failure. There are relatively weak Van der Waals interactions between the layers whilst the shear strength between the layers is small. This property is very interesting for applications like nano-bearings.

When nanotubes are compressed, they show remarkable properties. They bend over to surprisingly large angles, before they start to ripple and buckle, and then, finally kinks are developed. Note that all these deformations of the carbon nanotubes are elastic, all disappearing completely when the load is removed [16]. Note that the density of bundled CNTs is 1.33 to 1.40 gr/cm3; a very low value as compared to aluminium, possessing a density of 2.7 g/cm^3 [8].

3.2 Electrical properties

Graphite is one of the rare materials known as a semimetal and CNTs emerge as interesting conductors. Because electron waves can reinforce or cancel one another, an electron spreading around the circumference of a nanotube can completely cancel itself out; therefore, only electrons with the right wavelength remain. From all the possible electron wavelengths, or quantum states, available in a flat graphite sheet, only a tiny subset is allowed when that sheet is rolled into a nanotube. That subset depends on the circumference of the nanotube, as well as on the chirality (twist) of the nanotube.

In a graphite sheet, one particular electron state, designated as the Fermi point, provides to the graphite almost its whole conductivity; none of the electrons in other states are free to move about. All armchair tubes and one out of three zigzag and chiral tubes combine the right diameter and degree of twist to include this special Fermi point in their subset of allowed states. These nanotubes are truly conducting metallic nanowires. The remaining two thirds of nanotubes are semiconductors. For example, if n-m the roll-up factor, see Fig. 4, is three times an integer, the carbon nanotube has an extremely small gap, and at room temperature, it shows a metallic behaviour. For n=m, the tubes are metallic whilst for other values of n-m, the tubes behave as semiconductors with a band gap [5], indicating that, like silicon, they do not pass current easily without an additional amount of energy.

CNTs do not possess the same band gap, because for every circumference there is a unique set of allowed valences and conducting states; band gaps of 0.4-1 eV can be expected for SWNTs, corresponding to diameters between 0.6 and 1.6 nm [4]. As nanotube diameters increase, more and more states are allowed and the spacing between them reduces. In this way, different-size nanotubes can have band gaps as low as zero (like metal), as high as the band gap of silicon, and almost anywhere in between. No other known material can be so easily tuned. Note, however that, the growth of nanotubes currently provides a wide range of different geometries, and researchers are seeking improvements so that the specific types of nanotubes can be guaranteed.

Thick multi-walled nanotubes may display complex behaviour, because each layer of the tube has a slightly different geometry. By tailoring their composition individually, multi-walled tubes that are self-insulating or carry multiple signals at once, like nanoscopic coaxial cables, may be fabricated. However, the understanding and control of nanotube growth still falls short of these goals.

The fact that metallic nanowires are really good conductors is underlined by comparing them with copper. A bundle of nanotubes, could conduct about one billion A/cm2 whilst copper wires about one million A/cm^2 [8].

3.3 Electronic properties

The electronic properties of single-walled carbon nanotubes are shown to be extremely sensitive to the chemical environment [17]. Exposure to air or oxygen dramatically affects the nanotubes resistance and other electronic properties. These parameters can be reversibly "tuned" by surprisingly small concentrations of adsorbed gases, and an apparently semiconducting CNT can be converted into an apparent metal through such exposure. Hence, the electronic properties of a given nanotube are not specified only by the diameter and chirality of the nanotube, but also depend critically on the gas exposure history.

Another very interesting electronic property of CNTs, is their field emission; they emit electrons from their tips, when they are placed in an electrical field, see Fig. 6 [18]. Because they are sharp, the nanotubes emit electrons at lower voltages than electrodes made from most other materials, and their strong carbon bonds allow nanotubes to operate for longer periods without damage.

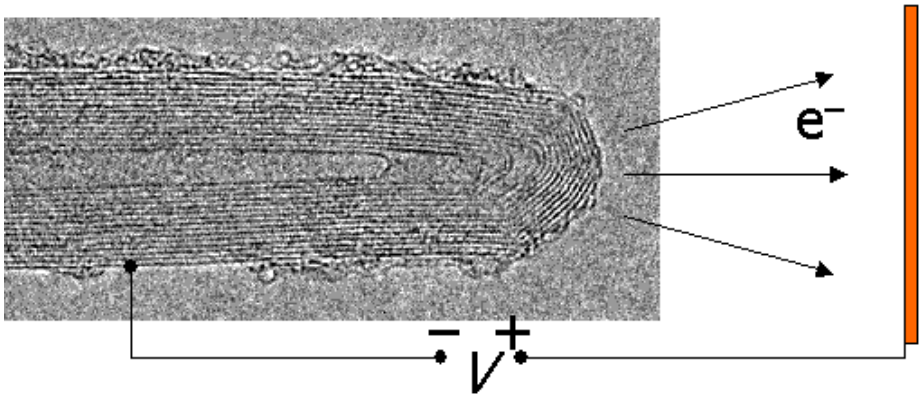

FIGURE 6. A schematic diagram of field emission of a nanotube.

3.4 Phonons and carriers in carbon nanotubes

The decoherence effects in low dimensional structures (e.g. CNTS) can be studied using the decoherence channels due to the Coulomb interaction to the background charge fluctuation and due to electron-phonon interaction [19]. The description of phonon modes are of special importance for estimating the *relaxation* and *dephasing* rates. Several models have been employed to calculate the phonon modes within CNTS like simple tight-binding model and the density-functional-based non-orthogonal tight-binding model among others [20]. On the other hand, the calculation of the carrier wavefunctions and the energy levels is subject of the numerical solution of Dirac equation.

Here, we briefly describe a semiclassical model of the dephasing mechanism. Neglecting the inhomogeneous broadening [21], the dephasing time (T_2) in terms of the excited-state lifetime T_1 and the pure-dephasing time T_2^* can be given by

$$\frac{1}{T_2} = \frac{1}{T_1} + \frac{1}{T_2^*}$$

The time T_2^* is related to the fluctuations in the carrier energy levels due to the interactions between the carriers and the phonons among others [19]. The corresponding dephasing and pure-dephasing time are a few tens of *fs*, while the relaxation time is a few tens of *ps* [21].

These kinds of calculations are very important for the quantum computer architecture and quantum optics research.

4 CNTS APPLICATIONS

The fact that nanotubes are very good conductors and that they also can appear as semiconductors or even insulators, makes them very useful for minuscule electronic devices like logic circuits built up out of several transistors. The making of tiny circuits might be promising for the semiconductor industry. This industry is focussed to make computer chips smaller every year, but also has to make them as cheap as possible.

Essential devices like field-effect transistors (FET) have been developed. They use a single semiconducting nanotube between two metal electrodes as the channel through which electrons flow. The current in this channel can be switched on or off by applying voltages to a nearby third “gate” electrode. It is found that this electrode can change the conductivity of the nanotube channel by a factor of one million or more, compared to silicon FETs. Because of its tiny size, however, the CNT-FET should switch reliably using much less power than a silicon-based device. It is predicted that, such a nanoscale device could run at clock speeds of one THz or more.

The fabrication of a CNT-FET starts with placing a tube on the insulating SiO2 layer, by spincoating of a suspension, with pre-arranged conducting pads. These pads are connected with the tube by metal leads, lithographically deposited across the tube. This technique is designated as the four-probe technique [22]. The silicon layer below the silicon dioxide is used as the back gate. The first nanotube-based devices operated at very low temperatures, but in 1998 the first transistor was reported that worked at room temperature, with electrical characteristics remarkably similar to silicon devices, see Fig. 7 [23].

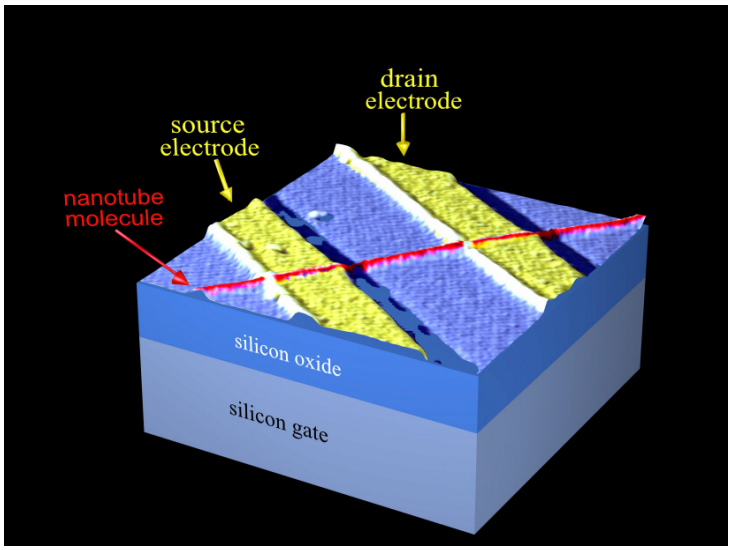

FIGURE 7. A single-molecule transistor that operates at room temperature, consisting of an individual semiconducting nanotube on two metal nanoelectrodes with the substrate as a gate electrode.

Metal-metal junctions lead to an improved version of a single electron transistor (SET). It has been proposed even as the future alternative to conventional silicon electronic components, but their practical use has been limited by the fact that they only operate at very low temperatures. However, recently the first single electron transistor operating at room temperature was reported

[24]. The device is similar to the FET described above, but with a short nanotube section of about 20 nm, that was manipulated by an atomic force microscope to create a Coulomb island. SETs consist of such a conducting island connected by tunnel barriers to two metallic leads. Strong bends (“buckles”) within the metallic carbon nanotubes are constructed using an AFM tip, and act as nanometre sized tunnel barriers for electron transport. The created resistance is in the order of 0.5 MΩ. For temperatures and bias voltages, that are low, relative to a characteristic energy required to add an electron to the island, electric transport through the device is blocked. Conduction or “Coulomb charging” is observed at room temperature, with an additional energy of 120 meV, by tuning a voltage on a close-by gate.

The next step in assessing the suitability of these devices for computer electronics involves the integration of individual CNT-FETs to form logic gates. To build such logic circuits, nanotube devices, that use electrons (n-type FET) and holes (p-type) as the carriers of electricity, are needed. The problem was that all CNT-FETs showed p-type characteristics, meaning that they were ON for negative gate bias [23]. Therefore, the first n-type CNT-FET had a great impact; it was made by direct doping of the tube with an electropositive element such as potassium. Potassium atoms (K atoms evaporated from an alkaline metal dispenser) are adsorbed onto the surface of the nanotube, donating electrons to convert the nanotube from p- to n-type. By covering half of the nanotube with PMMA, p-n junctions were produced [25]. Note, however, that, not only by doping, but also by annealing in a vacuum, their electrical character can be changed from p-type into n-type. Using vacuum annealing or doping to make n-type CNT-FETs, p- and n-CNT-FETs on the same substrate can be fabricated. These complementary CNT-FETs are assembled to form the first intermolecular logic gates. At first, a "NOT" gate or voltage inverter was demonstrated, see Fig. 8.

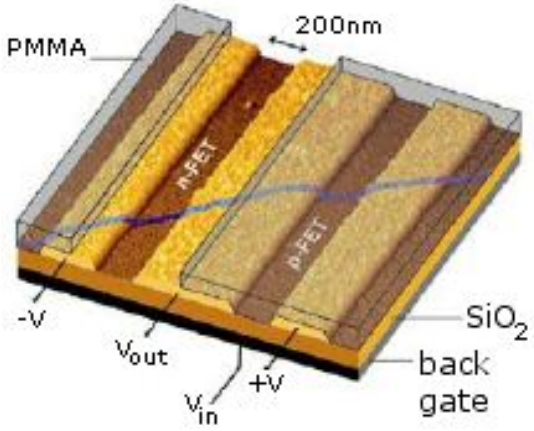

FIGURE 8. An AFM showing the design of an intramolecular logic gate consisting of a single nanotube bundle, positioned over the gold electrodes to produce two p-type CNT-FETs in series. The device is covered by PMMA, a window is opened by electron-beam lithography to expose part of the nanotube, and subsequently, potassium is evaporated through this window to produce an n-CNT-FET, while the other CNT-FET remains p-type [26].

Carbon fibre is already used to strengthen a wide range of materials, and the special properties of CNTS mean that they could be the ultimate high-strength fibre, which has a tensile strength 20 times, and a strength-to-weight ratio of 100 times that of steel. Nanotubes have already been used for reinforcement of nanostructural composite materials, polymers and concrete.

Incorporation of conducting carbon nanotubes in construction materials, such as concrete or structural plastics, provides opportunities for real time monitoring of material integrity and quality.

Open-ended nanostraws could penetrate into a cellular structure for chemical probing or could be used as ultrasmall pipettes to inject molecules into living cells. With the aid of computer simulations it was shown that water molecules will quickly enter and flow through a CNT of 8 nm in diameter. A separate set of simulations shows that certain organic molecules also will course through such nanotubes. The nanotubes conduct water at a rate similar to that of certain channels in the kidneys. These unusual transport properties of CNTs might be used in biomedical applications, such as highly targeted drug delivery.

The small size and sensitivity of nanotubes make the assembly of extremely powerful sensors possible. Semiconducting nanotubes change their electrical resistance dramatically when exposed to alkalis, halogens and other gasses at room temperature. For example, semiconducting CNTs have been used to detect gas molecules [27], whilst semiconductor nanowires have been used as detectors for a wide range of biological compounds. Also, nanowired field-effect transistors have been converted into sensors by modifying their surfaces with molecular receptors.

Kim and Lieber fabricated nanotube nanotweezers, by depositing free-standing electrically independent electrodes onto tapered glass micropipettes, which can be routinely made with end diameters of 100 nm [28]. The arms of the tweezers were about 4 μm long. The size of the nanotweezers was limited only by the optical microscope resolution used to monitor the attachment process.

5 CONCLUSIONS

In order to synthesise nanotubes there are three different methods, namely arc discharge, laser ablation, and CVD. For large-scale synthesis, the CVD method is most promising. The substrates can be recycled and the process works at lower temperatures (500–1000^{o} C), which makes the process suitable for direct growth on several devices. Nanoparticles of a metal catalyst are applied to create nanotubes of better quality. Also the structure of the substrate is very important. It is shown that aligned pores in silicon and alumina are most suitable to create neatly aligned nanotubes. The deposition of the metal catalyst on the substrate deserves special attention, because it enables manipulated growth.

The strength (around 40 GPa) and stiffness (elastic modulus around 1 TPa) of nanotubes makes them suitable for reinforcing materials and ropes, which can bear high deformations, and extremely high tensile forces. The theoretical understanding of the electronic structure and related properties of nanotubes and their outstanding field emission properties have made them preferable for use in electronics.

Several applications of nanotubes have been proposed such as scanning probe tips, nanotweezers and even nanobearings and nanosprings. Nanotubes are commonly found in laboratories today, and research is stimulated by large amounts of money invested in it. Some companies are already specializing in the production of carbon nanotubes, and give research a boost.

REFERENCES

1. Kroto HW, Heath JR, O'Brien SC, Curl RL and Smalley RE, Nature, 1985; 318; 162.
2. Iijima S, Helical microtubules of graphitic carbon, Nature, 1991; 354; 56-58.
3. Cohen ML, Nanotubes, Nanoscience, and Nanotechnology, Materials Science and Engineering: C, 2001; 15, Issues 1-2; 1-11.

4. Bonard JM, Kind H, Stöckli T and Nilsson LO, Field emission from carbon nanotubes: the first five years, Solid-State Electronics, 2001; 45 (6); 893-914.
5. Wildöer JWG, Venema LC, Rinzler AG, Smalley RE and Dekker C, Nature, 1998; 391; 59.
6. Ebbesen TW and Ajayan PM, Large scale synthesis of carbon nanotubes, Nature, 1992; 358; 220-222.
7. Yakobson BI and Smalley RE, Fullerene nanotubes: C1.000.000 and beyond, American Scientist, 1997; 85; 324-337.
8. Collins PG and Avouris P, Nanotubes for electronics, Scientific American, December 2000; 38-45.
9. Thess A, Lee R, Nikolaev P, Dai H, Petit P, Robert J, Xu C, Lee YH, Kim SG, Rinzler AG, Colbert DT, Scuseria GE, Tománek D, Fischer JE and Smalley RE, Crystalline Ropes of Metallic Carbon Nanotubes, Science, 1996; 273; 483-487.
10. Li WZ, Xie SS, Qian LX, Chang BH, Zou BS, Zhou WY, Zhao RA and G. Wang, Large-Scale Synthesis of Aligned Carbon Nanotubes, Science, 1996; 274; 1701-1703.
11. Xie S, Li W, Pan Z, Chang B and Sun L, Carbon nanotube arrays, Materials Science and Engineering A, 2000; 286 (1); 11-15.
12. Treacy MMJ, Ebbesen TW and Gibson JM, Exceptionally high Young's modulus observed for individual carbon nanotubes, Nature, 1996; 381; 678-680.
13. Wong EW, Sheehan PE, Lieber CM, Nanobeam mechanics: Elasticity, strength, and toughness of nanorods and nanotubes, Science, 1997; 277; 1971-1974.
14. Poncharal P, Wang ZL, Ugarte D, De Heer WA, Electrostatic deflections and electromechanical resonances of carbon nanotubes, Science, 1999; 283; 1513-1516.
15. Salvetat JP, Andrew G, Briggs D, Bonard JM, Basca RR and Kulik AJ, Elastic and shear moduli of single-walled carbon nanotube ropes, Phys Rev Lett, 1999; 82; 944.
16. Yu MF, Lourie O, Dyer MJ, Moloni K, Kelly TF and Ruoff RS, Strength and breaking mechanism of multiwalled carbon nanotubes under Tensile Load, Science, 2000; 287; 637-640.
17. Collins PG, Bradley K, Ishigami M and Zettl A, Extreme Oxygen Sensitivity of Electronic Properties of Carbon Nanotubes, Science, 2000; 287; 1801-1804.
18. Rinzler AG, Hafner JH, Nicolaev P, Lou L, Kim SG, Tomanek D, Nordlander P, Colbert DT, Smalley RE, Unraveling nanotubes: field emission from an atomic wire, Science, 1995; 269 ; 1550-1553.
19. V.N. Stavrou and G.P. Veropoulos (2011), *Advances in Mechanical Engineering Research*, Vol. 1, edited by E. Malach.
20. V.N. Popov and P. Lambin, Nano Res. 2010, 3(11):822-829.
21. Mukamel, S. (1995). *Principles of Nonlinear Optical Spectroscopy* (Oxford University Press, New York); S. V. Kilina and B.F. Habenicht, (2009). *Excitonic and Vibrational Dynamics in Nanotechnology, Quantum Dots Vs. Nanotubes*. (Pan Stanford Publishing)
22. Ebbesen TW, Lezec HJ, Hiura H, Bennett JW, Ghaemi HF and Thio T, Electrical conductivity of individual carbon nanotubes, Nature, 1996; 382; 54-56.
23. Tans SJ, Verschueren ARM, Dekker C, Room-temperature transistor based on a single carbon nanotube, Nature, 1998; 393; 49-52.
24. Postma HWC, Teepen T, Yao Z, Grifoni M and Dekker C, Carbon Nanotube Single-Electron Transistors at Room Temperature, Science, 2001; 293; 76-79.
25. Zhou C, Kong J, Yenilmez E, Dai H, Modulated chemical doping of individual carbon nanotubes, Science, 2000; 290; 1552-1555.
26. Derycke V, Martel R, Appenzeller J and Avouris P, Carbon nanotube inter- and intramolecular logic gates, Nano Letters 1, 2001; 453
27. Dai H, Hafner JH, Rinzler AG, Colbert DT and Smalley RE (1996), Nanotube as nanoprobes in scanning probe microscopy, Nature, 1996; 384; 147-150.
28. Kim P and Lieber CM, Nanotube Nanotweezers, Science, 1999; 286; 2148-2150.

Deviations from Exponential Decay Law in the Time Evolution of Quantum Resonant States Described by Lorentzian Line Shape Spectral Distributions

Theodosios G. Douvropoulos

Hellenic Naval Academy, Physics Department, Hatzikyriakou Ave. Piraeus, Greece 18539,
email: douvrotheo@snd.edu.gr douvrotheo@yahoo.com

Abstract. This paper investigates the deviations from exponential decay law for quantum resonant states which can be approximately described by Lorentzian line shape spectral distributions. We point the significance of the Lorentzian distribution in both classical and quantum theory of resonances and its close relevance to the exponential decay law. Using quite general physical arguments, such as the finite expectation value of the energy and the kinematical dependence of the distribution, we investigate the appearance of these deviations for short and long times respectively. We construct an analogous to the continuity equation describing the correlation between exponential and non exponential decay. When a measuring perturbation cancelling the terms in the second part of the equation is possible, interesting questions arise as is for example whether the quantum Zeno effect, in the limit of very short times, does really appear. It is found that besides the homogeneity of the proposed continuity equation, other factors, such as the energy dependence of the resonance's complex energy shift, play an important role in the observability of the non exponential decay.

Keywords: resonance, decay width, energy shift, survival amplitude,non exponential decay, spectral distribution, continuity equation, exponential source term, Langevin equation, observability, quantum measurement, quantum Zeno effect.

PACS : *03.65.-w, 47.10.ab, 05.40.Jc, 03.65.Xp*

1. INTRODUCTION

Resonances in quantum mechanics correspond to the unstable quantum states, and acquire a complex energy spectrum. The latter seems to contradict with the structure of quantum mechanics which is built in terms of eigenvectors in Hilbert space supporting a real energy spectrum. However the unstable quantum state is an important example of irreversible phenomena in nature and has a distinct role in quantum mechanics, ranging from excited atomic states to short-lived elementary particles.

The resonant states interact and finally decay into continuum spectra. Their spectrum turns to be complex since the imaginary part of each pole, equal to Γ/2, is directly related to the mean lifetime of the corresponding state via the $\tau = \mathrm{h}/\Gamma$, and expresses half the energy width of the resonance. The real part is constituted by both the energy value of the unperturbed state and the energy shift due to the interaction with the continuum, giving the energy position of the

resonance E_r, (or resonance mass in the relativistic case).The study of the decay of an unstable quantum state began with Gamow's theory [1] of alpha decay of atomic nuclei and Dirac's theory [2] of spontaneous emission of radiation by excited atoms, while a general treatment of decaying systems was given by Weisskopf and Wigner [3] and by Breit and Wigner [4]. Siegert [5] was the first to associate the complex poles in the S-matrix of Wheeler [6] to quantum resonances.

The signature of a resonant state is its spectral distribution. During the ages many models have been proposed for the choice of the spectral distribution, see for example **[7-12]** and references therein. Real and complex spectral distributions construct propagator functions with substantially different properties and conseque-nces on the system's time evolution. One of them seems to be the different type of non exponential decay for both regions of short and long times. The term non exponential decay is used for the description of the deviation from the exponential decay law, related to the evolution of the survival probability during an irreversible process. Although the exponential decay law is the universal hallmark of unstable states, deviations from it often prove to be more consistent with quantum mechanics. The dimensionless ratio

$$2E_r/\Gamma \equiv \beta \tag{1}$$

which is defined as twice the ratio of the energy position to the energy width of the resonance, is proved to be a very crucial and important quantity related to the appearance of such deviations, [13]. Deviations from the exponential law are present at times very close to the initial preparation time *t* = 0 and at very late times, while at "intermediate" times the exponential law represents a very good approximation. The intermediate – time region alone satisfies the simple composition law of probabi-lities $P(t_1)P(t_2) = P(t_1 + t_2)$. In this domain, therefore, a classical probability law operates, and the results for the two – step measurement are the same as for the one step measurement. At late times the decay law follows a power-law, which is however very difficult to observe experimentally because it occurs at times for which the survival probability is already vanishingly small. On the other hand, the deviations at small times occur within a very short time scale, for instance 10^{-15}s for the electromagnetic decays of an excited hydrogen atom [14] and even shorter for hadronic decays [15]. Beyond the theoretical prediction of such deviations there is much clear evidence for their experimental observation as well. The above may take place in many different branches of natural sciences, such as Nuclear Physics and Radioactivity, [16,17], Quantum field theory, [18], Atomic and Molecular Physics, [19,20], Charge transport, [21], Fluid dynamics, [22], Magnetism and spin dynamics, [16,23,24], Optics, [25], Chemical reactivity, [26], Biology, [27], Acoustics, [28], Geophysics, [24],Stochastic differential equations, [29], and may correspond to the presence of an unusual property in the system's dynamics, [30,31]. The above appear to be only a part of the extensive literature related to this subject.

This work studies the deviations from exponential decay law, in the framework of Lorentzian line shape spectral distributions. For this we first show the way the Lorentzian distribution appears in both quantum and classical mechanics. In quantum theory it is the work of Breit and Wigner [4], who studied the behavior of unstable particles, that revealed the Lorentzian distribution as the expression of the averaged phase shift of a wave in a scattering process. In classical mechanics the Lorentzian distribution describes the mean amount of energy absorbed per unit time, which is twice the mean value of the dissipative function, of a harmonically driven, harmonic oscillator with friction. It corresponds to a kind of dependence which is called dispersion-type frequency dependence of the absorption, [32]. We distinguish two types of spectral distributions, the Lorentzian with a semibounded spectrum, which we call truncated

Lorentzian distribution, and the generated complex Lorentzian distribution which occurs when keeping only the physical appropriate energy pole.

Next, we explore the appearance of the deviations from exponential decay in the limit of both short and long times. We use general arguments to show, that at short times the non decay probability falls off less rapidly than would be expected on the basis of the exponential decay law. The central point is that the time derivative of the survival amplitude at *t=0* is both finite and purely imaginary. In the limit of long times we use kinematical arguments to show that the decay has a time power law.

In the last part of the paper, we study the observability of the non exponential decay in the limit of very short times. For this we develop a model for the study of the correlation between exponential and non exponential decay, by constructing an analogous to the continuity equation. The homogeneity of this equation is achieved through the process of a measuring perturbation and is related to the observability of the non exponential decay. We discuss the possibility of the appearance of the quantum Zeno effect, in terms of a measuring process. Since the energy dependence of the resonance complex energy shift turns to be quite important, we explore these topics for various strengths of the above mentioned dependence.

2. LORENTZ LINE SHAPE DISTRIBUTION IN CLASSICAL AND QUANTUM MECHANICS

The fingerprints of a resonance reflect on its spectral distribution. The latter depends on the background and kinematical factors, and so we can only recover the centre of the resonance peak, which is the energy position of the resonance, and its width, defined as the energy distance between the points of half maximum of the distribution. However it is desirable to extract naturally the above mentioned quantities, as some kind of spectral information. This is done in absolute degree by the Lorentzian distribution, based on the Breit Wigner approximation,[4]. Breit and Wigner put the origins of the theory of quantum resonances by studying the behavior of unstable particles. They postulated that if an ustable particle at energy E_o decays according to the exponential decay law then the energy density should be approximately distributed according to the Breit-Wigner distribution which is Lorentzian line shape. This was done in the mathematical content of a scattering experiment which is captured by the scattering matrix and expressions derived from it. One of them, the scattering phase, measures the averaged phase shift which a wave experiences while passing through the scatterer, and according to the Breit-Wigner theory, should have an expression similar to the Lorentzian distribution. The Lorentzian spectral distribution is mathematically given by the following expression

$$f(E) = \frac{1}{\pi}\frac{\Gamma/2}{\left(E-E_r\right)^2+\Gamma^2/4} \tag{2}$$

where $E_r = E_o + \Delta$ is the energy position of the resonance and Γ is the width. In this formalism E_o corresponds to the energy of the unperturbed state in which the system is initially prepared at *t=0* and Δ is the energy shift due to interaction with the continuum. It is easy to see that the Lorenzian distribution is the Fourier transform of the exponential factor of the form $e^{-iE_r t-\Gamma|t|/2}$, where we have used the atomic system of units $\hbar = 1$,with contributions from both the negative and positive time. Indeed we obtain for $-\infty < E < \infty$

$$f(E) \equiv \frac{1}{2\pi}\int_{-\infty}^{+\infty} dt e^{-iE_r t-\Gamma|t|/2} e^{iEt} = \frac{1}{2\pi}\frac{1}{\Gamma/2+i\left(E-E_r\right)} + \frac{1}{2\pi}\frac{1}{\Gamma/2-i\left(E-E_r\right)}$$
$$= \frac{1}{\pi}\frac{\Gamma/2}{\left(E-E_r\right)^2+\Gamma^2/4}$$

(3)

We recognize two isolated poles at $E = E_r \pm i\Gamma/2$, that dominate the two pieces of the analytic Fourier transform. The one piece varies as $e^{-\Gamma t/2}$ for positive time and zero for negative time, while the other piece varies as $e^{\Gamma t/2}$ for negative time and zero for positive time. However neither piece corresponds to a compact autonomous state, since the state appears to be either created at *t=0*, or destroyed at *t=0*.

In classical mechanics the Lorentz line shape arises in the problem of a harmonically driven, harmonic oscillator with friction. The differential equation describing its motion is the following

$$\ddot{x} + \gamma\dot{x} + \omega_o{}^2 x = \frac{f}{m}e^{-i\omega t} \tag{4}$$

where *γ* stands for the damping constant, ω_o is the frequency of the unperturbed problem, *f* is the amplitude of the force, *m* is the mass of the system, and *ω* is the driving frequency. It is to be understood that we take in account only the real part of the right-hand side. It is easy to see that a particular solution of the above equation has the form

$$x(t) = \frac{f/m}{\omega_o{}^2 - \omega^2 - i\omega\gamma}e^{-i\omega t} \tag{5}$$

It is then interesting to calculate the two point correlation function coming as

$$\left\langle x^*(0)x(t)\right\rangle \equiv \frac{1}{2\pi}\int_{-\infty}^{+\infty} d\omega \frac{f^*/m}{\omega_o{}^2-\omega^2+i\omega\gamma}\cdot\frac{f/m}{\omega_o{}^2-\omega^2-i\omega\gamma}e^{-i\omega t} \tag{6}$$

The correlation function may be evaluated by complex contour integration yielding

for positive and negative times,

$$\left\langle x^*(0)x(t)\right\rangle = \begin{Bmatrix} \left|\frac{f}{m}\right|^2\left\{\frac{e^{-\gamma t/2}e^{-i\Omega t}}{2\Omega\gamma\left(2\Omega-i\gamma\right)}+\frac{e^{-\gamma t/2}e^{i\Omega t}}{2\Omega\gamma\left(2\Omega+i\gamma\right)}\right\} & for\ t>0 \\ \left|\frac{f}{m}\right|^2\left\{\frac{e^{\gamma t/2}e^{-i\Omega t}}{2\Omega\gamma\left(2\Omega+i\gamma\right)}+\frac{e^{\gamma t/2}e^{i\Omega t}}{2\Omega\gamma\left(2\Omega-i\gamma\right)}\right\} & for\ t<0 \end{Bmatrix} \tag{7}$$

or

$$\left\langle x^*(0)x(t)\right\rangle = \begin{Bmatrix} \left|\frac{f}{m}\right|^2\left\{\frac{2e^{-\gamma t/2}}{\gamma\left(4\Omega^2+\gamma^2\right)}\cos\Omega t+\frac{e^{-\gamma t/2}}{\Omega\left(4\Omega^2+\gamma^2\right)}\sin\Omega t\right\} & for\ t>0 \\ \left|\frac{f}{m}\right|^2\left\{\frac{2e^{\gamma t/2}}{\gamma\left(4\Omega^2+\gamma^2\right)}cos\Omega t+\frac{e^{\gamma t/2}}{\Omega\left(4\Omega^2+\gamma^2\right)}\sin\Omega t\right\} & for\ t<0 \end{Bmatrix} \tag{8}$$

where we have defined the frequency $\Omega = \sqrt{\omega_o{}^2 - \gamma^2/4}$. If the approximation

$\omega_o >> \gamma$ is used then the above formulae take the much simpler form

$$\left\langle x^*(0)x(t)\right\rangle \cong \left|\frac{f}{m}\right|^2 \frac{e^{-\gamma|t|/2}}{2\gamma\omega_o{}^2}\cos\omega_o t \tag{9}$$

We see that the temporal behavior of the correlation function is exponentially damped for both positive and negative time and thus directly related to the Lorentzian spectral distribution as we have seen earlier.

We can attack to the problem in a different way. Let us write $\frac{f/m}{\omega_o{}^2 - \omega^2 - i\omega\gamma} = \rho e^{i\vartheta}$ and find $\rho(\omega,\gamma) = \frac{f}{m}\frac{1}{\sqrt{\left(\omega_o{}^2 - \omega^2\right)^2 + \omega^2\gamma^2}}$ and $\tan\vartheta = \frac{\omega\gamma}{\omega_o{}^2 - \omega^2}$. In this way a particular integral of equation (4) is given by $x(t) = \rho e^{i(\vartheta - \omega t)}$. The general solution of (4) with zero on the right –hand side is given by

$$x(t) = ce^{-\gamma t/2}e^{i\Omega t} + de^{-\gamma t/2}e^{-i\Omega t} = ae^{-\gamma t/2}\cos(\Omega t + \varphi) \tag{10}$$

In this way the solution of (4) is the sum

$$x(t) = ae^{-\gamma t/2}\cos(\Omega t + \varphi) + \rho(\omega,\gamma)\cos(\omega t - \vartheta) \tag{11}$$

Since the first term decreases exponentially with time, after a sufficient time only the second term survives. In fact the first term describes the transient behavior of the system. In contrast with a resonance without damping, the amplitude of oscillation, quantity $\rho(\omega,\gamma)$, depends on the frequency of the driving force, and acquires its maximum value when $\omega = \sqrt{\omega_o{}^2 - \gamma^2/2}$. However this maximum is not infinite as for the case of the resonance without friction. If the damping constant is small enough then the range of resonance is very close to ω_o. Let us again assume that $\omega_o >> \gamma$, and write $\omega = \omega_o + \delta\omega$, with $\delta\omega$ very small. We will then find that

$$\rho(\omega,\gamma) = \frac{f}{m}\frac{1}{2\omega_o\sqrt{\delta\omega^2 + \gamma^2/4}} \tag{12}$$

During the oscillation the system continuously absorbs energy from the source of the external force, which in turn dissipates to the environment. The mean amount of energy absorbed per unit time is given as twice the mean value of the dissipative function, [33]. The latter is in generally a quadratic function of the $\dot{x}_i$ for a system with many degrees of freedom, and in our case is given by $F = \frac{1}{2}\gamma m\dot{x}^2$. It is easy to see that

$$F=\frac{1}{2}\gamma m\rho^2(\omega,\gamma)\sin^2(\omega t-\vartheta)\omega^2 \Rightarrow \overline{F}=\frac{1}{4}\gamma m\omega^2\left(\frac{f}{m}\right)^2\frac{1}{4\omega_o{}^2\left(\delta\omega^2+\gamma^2/4\right)}\Rightarrow$$
$$\overline{F}\cong\frac{f^2}{4m}\frac{\gamma/4}{\left(\delta\omega^2+\gamma^2/4\right)} \quad (13)$$

Clearly we have reached to the Lorentzian line shape for the energy absorption, and this kind of dependence is called dispersion-type frequency dependence of the absorption, **[32]**. Thus, classical and quantum physics include phenomena that they are supported by the Lorentzian line shape distribution.

3. DEVIATIONS FROM EXPONENTIAL DECAY LAW IN THE LIMIT OF SHORT AND LONG TIMES.

In the previous section we used the correlation function discussing resonances in classical mechanics. The quantum analogous of the two point correlation function is the survival amplitude, defined as

$$a(t) \equiv \left\langle \Phi_o \left| e^{-iHt} \right| \Phi_o \right\rangle = \left\langle \Phi_o \left| \Phi(t) \right\rangle \right. \quad (14)$$

Here $\left|\Phi_o\right\rangle$ represents the initial state of the system, meaning the state in which it has been prepared at $t=0$ and H is the system's Hamiltonian. The latter is assumed to be exactly known and usually corresponding to the unperturbed problem where no interaction to the continuum is possible. It can be described by a localized wave packet whose energy E_o is inside the continuous spectrum. In this way $\left|\Phi(t)\right\rangle$ represents the time evolution of the initial state at arbitrary times. We can now insert the unit operator $\hat{I}$ constructed by the complete set of states of the Hamiltonian

$$\hat{\mathrm{I}}=\int dE\left|E\right\rangle\left\langle E\right| \quad (15)$$

which obviously satisfy the Schrödinger equation $H\left|E\right\rangle = E\left|E\right\rangle$, and get

$$a(t)=\left\langle \Phi_o \left| \mathrm{e}^{-iHt} \right| \Phi_o \right\rangle \Rightarrow a(t)=\left\langle \Phi_o \left| \int dE\left|E\right\rangle\left\langle E\right| \mathrm{e}^{-iHt} \right| \Phi_o \right\rangle \Rightarrow$$
$$a(t)=\left\langle \Phi_o \left| \int dE\left|E\right\rangle\left\langle E\right| \mathrm{e}^{-iEt} \right| \Phi_o \right\rangle = \int dE\,\mathrm{e}^{-iEt}\left|\left\langle \Phi_o \left| E \right\rangle\right|^2 \quad (16)$$

where again we use the atomic system of units where $\hbar=1$. The last term of the above equation defines the spectral distribution in terms of the Hamiltonian states and the initial state as well, through the $\rho(E)=\left|\left\langle \Phi_o \left| E \right\rangle\right|^2$. It demonstrates the physical meaning of the spectral distribution as the weight function for contribution of each of the energy states of the Hamiltonian to the construction of the survival amplitude. In other words the following quantity

$$\int_E^{E+dE}\rho(\varepsilon)d\varepsilon \quad (17)$$

is the probability that the energy of the state lies in the interval [*E,E+dE*]. It is clear from (16) that the Fourier transform of the spectral distribution is equal to the survival amplitude.The survival probability is given by

$$P(t) = \left|\left\langle \Psi_o \left| \Phi(t) \right\rangle\right|^2 = \left|a(t)\right|^2 \tag{18}$$

and must satisfy the following two conditions: $P(0) = 1$, and $P(\infty) = 0$, due to preparation and non stationarity respectively. In order to compute the survival amplitude $a(t)$,we must know $\left|\Phi(t)\right\rangle$, which is the solution of the time dependent Schrödinger equation. This is not trivial at all since it demands the knowledge of all of the interactions in a generally complicated problem. Alternatively we can assume a specific form for the spectral distribution of the system, based on certain properties and conditions that have to be fulfilled, and then calculate the survival amplitude through Fourier or Laplace transforms, [7-10,13], (and references therein). Among the various types of spectral distributions the Lorentzian, although still an approxima-tion is rather the most popular since not only occurs in many branches of physics and different phenomena: deexcitation of atomic levels, alpha decay, resonant scattering, but also because it constitutes the generator of many other types of distributions or extensions thereof, [13,35-43]. More than this it has been seen that the Lorentzian spectral distribution can be directly related to Gamow vectors and exponential time evolution without violating causality, [35]. However an issue to be discussed has to do with the violation of its spectrum boundedness. In other words the Lorentzian spectral distribution violates the spectral condition to obtain a strict exponential decay. This happens because we admit states with arbitrarily large negative energies. This violation would also violate the second law of thermodynamics, [34] and the uncertainty principle as well. For the first case we can imagine suitable interactions to take arbitrarily large amounts of energy from the system. The first law of thermodynamics can be satisfied and yet the available energy from the system is arbitrarily large. This must not be possible and so the unbounded spectrum by itself should not occur. For the second case we have to think that the infinite negative potential energy, would confine a particle in a very small area, for example an electron near the nucleus. In this way both *δx* and *δp* tend to zero which is a contradiction to the uncertainty principle. So, since the distribution should actually be truncated to positive *E*, corresponding to the threshold of the continuum spectrum, we equivalently set $\rho(E) = 0$ for $E \le 0$. The $\rho(E)$ is called *Truncated Lorentzian Distribution TLD,* and its general form is the:

$$\begin{aligned} \rho^{TLD}(E) &= N \frac{\Gamma(E)/2}{\left(E - E_o - \Delta(E)\right)^2 + \Gamma(E)^2/4} \text{ for } E > 0 \\ &= 0 \text{ for } E < 0 \end{aligned}, \tag{19}$$

where $\Delta(E)$ is the energy shift, $\Gamma(E)$ is the energy width of the resonance and N is a normalization factor different from 1/π since the distribution is now semibounded. For the same reason both the energy shift and the energy width are now energy dependent. The distribution $\rho^{TLD}(E)$ is a real function of energy and must satisfy the following condition of normalization, since probability is conserved:

$$\int_0^\infty \rho^{TLD}(E)\, dE = 1 \tag{20}$$

which is equivalent to write $a(0) = a^*(0) = 1$. This equation determines the value of quantity *N* and gives:

$$N\left(\beta(E),\delta(E)\right) = \left\{\left[\delta(E) + \tan^{-1}\beta(E)\right]\right\}^{-1} \quad (21)$$

where quantity $\delta(E)$ represents an angle close but not equal to $\pi/2$ as a consequence of the energy dependence of both quantities $\Delta(E)$ and $\Gamma(E)$, analytically shown in **[13].** In fact the energy dependence of the angle **δ** makes the Lorentzian a better approximation. It is quite obvious from eq. (19) that the truncated Lorentzian distribution reveals two complex energy poles that come as the complex conjugates of each other:

$$z = \mathrm{E}_r(E) + i\Gamma(E)/2 \quad , \quad z^* = \mathrm{E}_r(E) - i\Gamma(E)/2 \quad (22)$$

However since the propagator function must properly describe the irreversible time evolution of the system, only the z^* pole should be chosen in order to give the correct exponential decay law of the form $P(t) \square e^{-\Gamma t/\hbar}$. Having this in mind some-one can propose instead a complex function of energy that intrinsically carries irreversibility and causality, and arises from $\rho^{TLD}(E)$ by keeping only the z^* pole, meaning the Complex Lorentzian Distribution *CLD*:

$$\rho^{CLD}(E) = \frac{\tilde{N}\left(\beta(E)\right)}{2} \frac{i}{E - E_r(E) + i\,\Gamma(E)/2} \quad (23)$$

leading to a time evolution of the form $\left|\Phi(t)\right\rangle = \theta(t)e^{-iE_r t-(1/2)\Gamma t}\left|\Phi_o\right\rangle$.

The Paley-Wiener theorem **[44]** states that if the spectrum is bounded from below, then the survival amplitude and hence the survival probability decreases to zero as time passes less rapidly than any exponential function, and thus deviates from expo-nential decay. In fact we can show that deviations from exponential decay in the limit of long times, arise from clearly kinematical arguments. As we have already pointed, the spectral distribution depends on the background and kinematical factors. For example we can separate the phase space factor *σ(E)* in the spectral distribution and write the latter as

$$\rho(\varepsilon) = f(\varepsilon)\cdot\sigma(\varepsilon) \quad (24)$$

where the form factor *f(ε)* expresses the energy distribution of the decay products, to whom the unstable state is finally distributed. As time grows the wave packet of the initial state spreads so that the decay products separate sufficiently far to be outside each other's influence, and the distribution becomes clearly kinematic. This means that the form factor is smoothly varying after some large but finite time, since the corresponding interactions between the decay products become negligible. The remaining phase space factor has the form

$$\sigma(E) = \frac{d}{dE}\left(\frac{4}{3}\pi k^3\right) = 4\pi k^2\frac{dk}{dE} \quad (25)$$

where k is the wave number associated to the remaining kinetic energy via the $E = \frac{k^2}{2m}$. In this way we have

$$\sigma(E) = 8m\pi E\cdot\sqrt{\frac{m}{2E}} = 4\sqrt{2}\pi m^{3/2}\sqrt{E} \quad (26)$$

Thus, the survival amplitude for large times behaves as

$$a(t)=\int_0^\infty dEe^{-iEt}\rho(E)\cong\int_0^\infty dEe^{-iEt}\sigma(E)=4\sqrt{2}\pi m^{3/2}\int_0^\infty dEe^{-iEt}\sqrt{E}$$
$$=\frac{1}{t}\frac{1}{\sqrt{t}}4\sqrt{2}\pi m^{3/2}\int_0^\infty dze^{-iz}\sqrt{z}:\ \ t^{-3/2} \tag{27}$$

where we have reached the same result as in **[13]** but in a different way.

We may now examine the behavior of the survival amplitude, in the limit of very short times. The spectrum of the Hamiltonian is semibounded and in addition we assume that the expectation value of the energy at t=0 is finite. The expectation value of the energy may be taken as $\left\langle \Phi_o \left| \hat{\mathrm{H}} \right| \Phi_o \right\rangle$ or alternatively via the use of the spectral distribution,

$$\left\langle E \right\rangle = \int_0^\infty \varepsilon\rho(\varepsilon)d\varepsilon \tag{28}$$

It is interesting to notice that the time derivative of the survival amplitude at *t=0* is connected to the expectation value of the energy since it is true that

$$\dot{\alpha}(t)=\int_0^\infty dE(-iE)e^{-iEt}\rho(E)\Rightarrow\left|\dot{\alpha}(0)\right|=\int_0^\infty E\rho(E)dE=\left\langle E\right\rangle \tag{29}$$

Writing down the survival probability we can actually write

$$P(t)=\alpha(t)\cdot\alpha^*(t)\Rightarrow\frac{dP(t)}{dt}=\dot{\alpha}(t)\cdot\alpha^*(t)+\alpha(t)\cdot\dot{\alpha}^*(t) \tag{30}$$

The time derivative of the survival amplitude is continuous since we have

$\left|\dot{\alpha}(t)\right|=\left|\int_0^\infty dE(-iE)e^{-iEt}\rho(E)\right|\le\int_0^\infty\left|E\right|\left|\rho(E)\right|dE<\infty$ and $\left\langle E\right\rangle$ is finite. It is easy to see that quantity $\dot{\alpha}(0)$ is a purely imaginary quantity equal to

$$\dot{\alpha}(0)=-i\left\langle E\right\rangle \tag{31}$$

If this is the case then the time derivate of the survival probability at t=0, is equal to

$$\left.\frac{dP(t)}{dt}\right|_{t=0}=\dot{\alpha}(0)\cdot\alpha^*(0)+\alpha(0)\cdot\dot{\alpha}^*(0)=\dot{\alpha}(0)\cdot1+1\cdot\left(-\dot{\alpha}(0)\right)=0 \tag{32}$$

The last result shows that the decay can not be exponential at very short times since then we should actually have, $\left.\frac{dP(t)}{dt}\right|_{t=0}=-\Gamma$. So at sufficient small time, the non decay probability falls off less rapidly than would be expected on the basis of the exponential decay law.

For each case of distribution, *TLD* or *CLD*, it was shown in **[13]** that the time evolution of an unstable system is constituted by two parts: the exponential decay part and the non exponential decay part. The exponential decay parts were exactly the same for the two distributions, while the non exponential decay parts had substantial in between differences. These differences had

mainly to do with the form of the non exponential survival amplitude. The real spectral distribution gave the following amplitude:

$$\mathrm{I}^{TLD}(\beta,\alpha) = N(\beta,\delta) \int_{\delta}^{\tan^{-1}\beta} \exp[i\alpha(\beta-\tan\theta)]\, d\theta \tag{33}$$

while the complex distribution gave:

$$I^{CLD}(\beta,\alpha) = \frac{N(\beta,\delta)}{2} \int_{\delta}^{\tan^{-1}\beta} \mathrm{d}\theta \exp\{i[\alpha(\tan\theta-\beta)-\theta]\}/\cos\theta \tag{34}$$

In the above relations we have used the following dimensionless quantities, $\alpha \equiv t/2\tau_d$ where τ_d is the mean lifetime of the resonant state and $\beta \equiv 2E_r/\Gamma$ as twice the ratio of the energy position to the decay width of the resonant state. In addition the non exponential amplitudes satisfy a different differential equation. Both of them come as a classical Langevin type of equation, [45], with quantity $\omega(\beta,\delta) \equiv (\beta - \tan\delta)$ (35)

corresponding to the frequency of the rapidly oscillating stochastic terms, and carrying information from the limits of the spectrum, [13,46].

4. CORRELATION BETWEEN EXPONENTIAL AND NON EXPONENTIAL AMPLITUDE.

The exponential part of the decay is totally determined by the width function $\Gamma(E)$ since the latter describes the rate of exponential decay of the system's survival probability. This quantity is produced through the interaction of the system with the continuum, and there exist many different methods for its calculation. For example it can be constructed through Fermi's golden rule, [47], where it is produced from the contribution of the matrix elements of the interaction potential, or alternatively through path integral methods, [48], and contributions of the classical action inside the potential barrier. The energy shift $\Delta(E)$ is also produced by the interaction terms and according to [48] is given as a function of the derivative of the classical action inside the potential barrier with respect to energy. It is clear from the above that both quantities $\Gamma(E)$ and $E_r(E)$ are similarly constructed and depend on the type and strength of the interaction with the continuum, and so does their ratio β.

Following Dirac's formalism we can define a vector whose energy wave function is a Lorentzian distribution, meaning the

$$|\phi\rangle = \int dE\,|E\rangle\langle E|\phi\rangle = \int dE\,|E\rangle\left(i\sqrt{\frac{\Gamma}{2\pi}}\frac{1}{E-(E_r-i\Gamma/2)}\right) \tag{36}$$

If we choose the boundaries of integration to be $-\infty \le E < \infty$, the length of this vector is given by

$$\langle\phi|\phi\rangle = \int_{-\infty}^{\infty} dE\,\langle\Psi^G|E\rangle\langle E|\Psi^G\rangle = \int_{-\infty}^{\infty} dE\,\frac{\Gamma}{2\pi}\frac{1}{(E-E_r)^2+\Gamma^2 4} = 1 \tag{37}$$

However if we choose the boundaries according to the rules of standard quantum mechanics, $0 \le E < \infty$, we get

$$\langle\phi|\phi\rangle = \int_0^\infty dE \left\langle \Psi^G \middle| E \right\rangle \left\langle E \middle| \Psi^G \right\rangle = \int_0^\infty dE \frac{\Gamma}{2\pi} \frac{1}{\left(E - E_r\right)^2 + \Gamma^2 4} =$$
$$\frac{1}{\pi} \int_{-\beta}^{\infty} dz \frac{1}{z^2+1} = 1 - \frac{1}{\pi}\left\{\beta^{-1} - \frac{\beta^{-3}}{3} + ..\right\} \tag{38}$$

The first length equals 1, and corresponds to the pure exponential decay law as we have already seen in eq. (3). The second length is less than 1, and corresponds to the mixed propagation, exponential and non exponential, given as a function of the ratio β. It was shown in [13] and can be established once more from the above relations, that in the limit where β tends to infinity the exponential decay becomes the only contribution in the system's time evolution, (the results of equations 37 and 38 coincide). On the contrary when β takes values close to 1 the exponential decay part becomes much less significant. For intermediate values of the ratio β we get an interplay between exponential and non exponential decay and this is reflected on the values of the length of eq. (38). It is easily seen that equation (38) describes an increasing function of β. So there is an one by one correspondence between the strength of the exponential decay and the values of the ratio β. In this way the correlation between the exponential and the non exponential decay generates translations in the β parameter and we may think of it as the generator of the one dimensional space introduced by β. Inside this generalized space, the non exponential part of the decay will classically flow, while the space points may act as secondary either destructive or constructive sources. The study of this kind of behaviour is expected to extract information about the correlation between the two types of evolution.

The continuity equation expresses the fact that inside a finite volume "mass" or "charge" is conserved in the absence of external sources and this makes the equation homogeneous. As a first step in the mathematical analysis that follows a generalized density and current must be properly introduced. Classical intuition is related to probabilities which are the directly observed quantities. But probabilities do not propagate. Propagation is for the amplitude. Thinking so, the generalized density is defined by the non exponential amplitude itself, meaning $\mathrm{A} = \mathrm{I}^{TLD}(\beta,\alpha)$ or $\mathrm{I}^{CLD}(\beta,\alpha)$ and depends on both space, (meaning $\beta \equiv 2E_r/\Gamma$) and time, (meaning $\alpha \equiv t/2\tau_d$). The corresponding current comes then naturally as

$$J \equiv \beta \frac{\partial \mathrm{A}(\beta,\alpha)}{\partial \alpha} \tag{39}$$

The continuity equation comes as [49],

$$\frac{\partial \rho}{\partial t} + div\, \vec{J} = 0 \tag{40}$$

and takes the following form for the case of the non exponential amplitudes:

$$\frac{\partial \mathrm{A}(\beta,\alpha)}{\partial \alpha} + \frac{\partial}{\partial \beta}\left(\beta \frac{\partial \mathrm{A}(\beta,\alpha)}{\partial \alpha}\right) = 0 \tag{41}$$

In the following paragraphs the specific form of eq. (41) is investigated for the cases of real and complex spectral distributions that were previously mentioned. It is easy to see after a little piece of algebra, that the conservation law takes the following form:

$$\frac{\partial \mathrm{I}^{TLD\ or\ CLD}(\beta,\alpha)}{\partial\alpha} + \frac{\partial}{\partial\beta}\left(\beta\frac{\partial \mathrm{I}^{TLD}(\beta,\alpha)}{\partial\alpha}\right) = \left[\frac{\mathrm{sech}(\ln\beta)}{4N(\beta,\delta)} - 1\right]\times$$

$$\frac{iN(\beta,\delta)}{\tau_d}\int_{\delta}^{\tan^{-1}\beta}\left[(\beta\ or\ 0.5) - (1\ or\ 0.5i)\tan\theta\right]\exp[i\alpha(\tan\theta-\beta)]\,d\theta \quad (42)$$

It is obvious that the continuity equation is inhomogeneous since an additional term in the right hand of the equation appears and which we define as the exponential source term, (*est*). However the lack of homogeneity has important consequences in terms of physics. Due to the first term of the left hand side of eq. (42), the *est* corresponds to a first time derivative of an amplitude and can be cancelled if a suitable measuring perturbation is applied. In the limit of short times this cancellation would make the non exponential decay uncorrelated to the exponential one, and consequently observable. So the question is whether these terms can be cancelled at this regime of time. This can be achieved only if the *est* takes finite values which in turn ensures that we can actually follow the system through its evolution. We are interested in the limit of short times not only because it is the regime of time where the non exponential decay becomes important but also because we may want to discuss some interesting and peculiar phenomena such as the quantum Zeno effect.

The *est* term comes as a function of quantities α and β, and of the resonance's lifetime τ_d and corresponds to the correlation between exponential and non-exponential decay during the system's time evolution. The first thing to notice is the fact that the continuity equation becomes homogeneous when the following condition is satisfied:

$$4N(\beta_o,\pi/2) = \mathrm{sech}(\ln\beta_o) \quad (43)$$

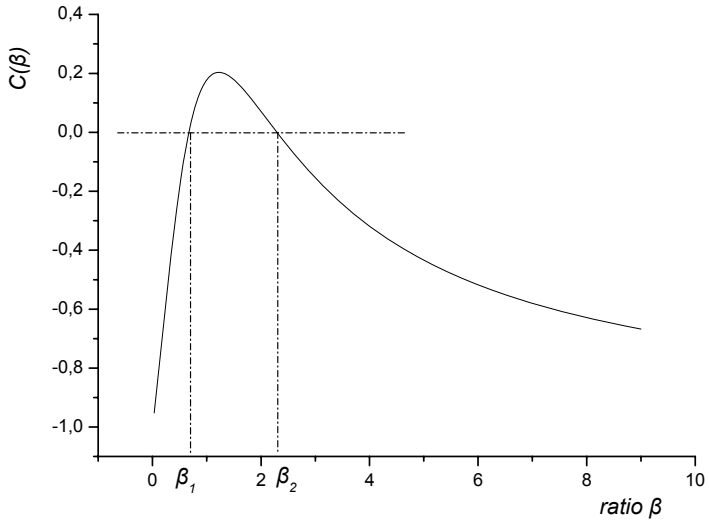

FIGURE 1. The variation of quantity *C(β)* with *β*. Its Lorentzian shape shows a maximum at *β=1.25*, and approaches -1 for both $\beta \to 0, \infty$.

For a given system, the different possible values of quantity β correspond to different kind and strength of interactions with the continuum.By solving numerically the

transcendental equation (43) we find two solutions namely $\beta_1 \cong 0.67$ and $\beta_2 \cong 2.29$. These answer directly to the question of how close to unit must ratio *β* be in order for the non-exponential decay to dominate the evolution. On the other hand and since *β* also appears in the limit of integration in the right term of (42), as $\beta \to \infty$ the flow disappears and the same of course happens with the correlation between the two kinds of evolution. In fact we can draw in Figure 1 that follows quantity *C(β)* as a function of *β* defined by

$$\mathrm{C}(\beta)=[\frac{\mathrm{sech}(\ln\beta)}{4N(\beta,\pi/2)}-1] \tag{44}$$

For both regions of $\beta \to 0$ and $\beta \to \infty$,*C(β)* approaches -1. It is interesting to notice that *C(β)* has itself a Lorentzian-like shape. When condition (43) is satisfied, the non exponential part of the decay is conserved and the interaction between the two different types of propagation is negligible.

However we are interested for other values of the ratio β as well. For this we exa-mine in more details the behavior of the *est* term, in the lines that follow. Concernig the real spectral distribution, we first treat the case where the interaction with the continuum, through a potential barrier for example, changes both *δ(E)* and *β(E)*in a way that the following relation holds

$$\beta(E) \cong \tan\delta(E) \tag{45}$$

This would correspond to the situation where the complex energy shift is strongly energy dependent. This makes *δ(E)* also strongly energy dependent and reflects on the magnitude of its derivative. We can then approximate *est* $^{\mathrm{R}}$ and after a little piece of algebra find that

$$est^{R}{}_{\left|\frac{d\delta}{dE}\right|>>} \cong i\frac{N(\beta,\delta)}{1+\beta^2}\left[\frac{\mathrm{sech}(\ln\beta)}{4N(\beta,\delta)}-1\right](\tan\delta-\beta)^2 \tag{46}$$

It is interesting to notice that there is no time dependence of the *est* $^{\mathrm{R}}$, to be discussed in the next section. For all the other types of smooth dependent complex energy shifts we can approximate *est* $^{\mathrm{R}}$ as follows

$$\begin{aligned} est^{R}{}_{t>} \cong{}& \frac{i}{2\tau_d}\left[N(\beta,\delta)-\frac{\mathrm{sech}(\ln\beta)}{4}\right]\mathrm{x} \\ &\left\{\begin{aligned} &-i\omega(\beta,\delta)\exp\left(i\omega(\beta,\delta)t\right)\sum_{n=0}^{\infty}\frac{n!}{(t/\tau_d)^{n+1}}\left(\frac{1}{(i\tan\delta+1)^{n+1}}-\frac{1}{(i\tan\delta-1)^{n+1}}\right)+ \\ &\exp\left(i\omega(\beta,\delta)t\right)\sum_{n=0}^{\infty}\frac{(n+1)!}{(t/\tau_d)^{n+2}}\left(\frac{1}{(i\tan\delta-1)^{n+1}}-\frac{1}{(i\tan\delta+1)^{n+1}}\right)+ \\ &\sum_{n=0}^{\infty}\frac{(n+1)!}{(t/\tau_d)^{n+2}}\left(\frac{1}{(i\beta+1)^{n+1}}-\frac{1}{(i\beta-1)^{n+1}}\right) \end{aligned}\right\} \end{aligned} \tag{47}$$

where the above formula stands for times beyond the short time regime. In the region of very short times it is easy to approximate *est* $^{\mathrm{R}}$ according to the following formula

$$est^{R}{}_{t<<} \cong \frac{1}{\tau_d}\left[\frac{\mathrm{sech}(\ln\beta)}{4} - N(\beta,\delta)\right]\mathrm{x}$$
$$\left\{ i\left[\beta\left(\tan^{-1}\beta - \delta\right) + \ln\frac{\cos\tan^{-1}\beta}{\cos\delta}\right] - \right.$$
$$\left. \frac{t}{2\tau_d}\left[\left(\tan^{-1}\beta - \delta\right)\left(1-\beta^2\right) - 2\beta\ln\frac{\cos\tan^{-1}\beta}{\cos\delta} + \tan\delta - \beta\right]\right\} \quad (48)$$

In the case of the complex spectral distribution a different type of *est* ^{C} is revealed, where c stands for the complex distribution. It is not difficult to find the following operator that connects the *est* for the two different types of spectral distribution

$$est^{C} \equiv \hat{C} \to R\ est^{R} = \frac{1}{2}\left(1 - i\beta - \frac{\partial}{\partial\alpha}\right)est^{R} \quad (49)$$

We may now focus on the short time regime and discuss the observability of the non exponential part of the decay. The case of long times can easily be handled, at least in a theoretical base, since the polynomial form of the non exponential propagation always dominates the exponential part after a certain number of lifetimes [13]. In the latter case the only problem to be solved experimentally has mostly to do with the very small magnitude of the propagation at these limits of time, while in the former case there exist other difficulties as well, related to the quantum nature of the resonant states, and the tunneling process, [13,46,48]. The angle δ that enters the calculations as the second limit of integration in the propagator integral equations, carries information from the limits of the energy spectrum at very short times and contributes significantly to the non exponential propagation. An earlier study of these contributions, [46], concerned the question of observability "of early time departures from Fermi's golden rule" where the issue of the non exponential propagation at $t = 0$ was discussed at length.

As we have already said *est* terms correspond to the first time derivative of a quantity with the same dimensions as those of the amplitude meaning a matrix element of the form $\left\langle \Phi_o \middle| \hat{\mu}(t) \middle| \Phi_o \right\rangle$, where $\hat{\mu}(t)$ stands for the perturbation effected by a measurement, and Φ_o stands for the initial state of the system at *t=0* with energy E_O as has been already mentioned. The evolution of the system is described by

$$i\hbar\frac{\partial}{\partial t}\left|\Phi(t)\right\rangle = \hat{H}\left|\Phi(t)\right\rangle \quad (50)$$

where $\hat{H}$ is the Hamiltonian operator and $\left|\Phi(0)\right\rangle = \Phi_O$. We assume that the measurement process at the limit of very short times permits interaction with the continuum. For example we may have a time dependent potential barrier that alters both the classical allowed and classical forbidden region of motion, and eventually quantities δ and β. This also changes the state of the system from Φ_O to $\left|\Phi(t)\right\rangle$, and makes quantity $\left\langle \Phi_o \middle| \Phi(t) \right\rangle = \left\langle \Phi_o \middle| \hat{\mu}(t) \middle| \Phi_o \right\rangle \equiv a(t)$ the survival amplitude. It follows directly from (50) that $i\hbar\dot{\alpha}(t) = \left\langle \Phi_o \middle| \hat{H} \middle| \Phi(t) \right\rangle$ and for *t=0* we have

$$i\hbar\dot{a}(0) = \left\langle \Phi_o \middle| \hat{H} \middle| \Phi_o \right\rangle = E_O \quad (51)$$

The above relation expresses the fact that in the limit of very short times quantity $\dot{\alpha}(0)$ must be purely imaginary. This is true for the real Lorentzian distribution, as can be easily proved from (48) where we get

$$\dot{a}(0) \cong i\frac{1}{\tau_d}\left[\frac{\operatorname{sech}(\ln\beta)}{4} - N(\beta)\right]\left[\beta\left(\tan^{-1}\beta - \delta\right) + \ln\frac{\cos\tan^{-1}\beta}{\cos\delta}\right] \tag{52}$$

This is not true however for the complex distribution due to relation (49) which makes $\dot{\alpha}(0)$ a complex and not purely imaginary quantity. This means that the complex spectral distribution does not provide a complete theory for the observability of the non exponential decay in the limit of very short times. Let us focus on the purely imaginary character of quantity $\dot{a}(0)$. Following the steps that lead to exponential decay, we assume that the system is prepared in state $|\Phi_o\rangle$ at a time t and that the probability of decay in a time interval is Γdt. Thus if the probability that the system was in state $|\Phi_o\rangle$ is $P(t)$ then the probability that the system will be in state $|\Phi_o\rangle$ at a time *t+dt* will be $P(t+dt) = P(t)(1-\Gamma dt)$ and this of course leads to exponential decay. If we now work with the survival amplitude we will take

$$P(t+dt) = |a(t+dt)|^2 = |a(t)+\dot{a}(t)dt)|^2 = |a(t)|^2\left|1+\frac{\dot{a}(t)}{a(t)}dt\right|^2 = P(t)\left|1+\frac{\dot{a}(t)}{a(t)}dt\right|^2 \tag{53}$$

Since $a(0)=1$ and $\dot{a}(0)=i\gamma$ we have for *t=0*, $P(dt) = 1+\gamma^2 dt^2$. The latter is greater than unit however this inconsistency is removed if we take in account all the remaining derivatives of the amplitude in the expansion of $a(t+dt)$. The case of exponential decay gives $P(dt) = 1-\Gamma dt$. If we look at $P(dt)$ as a polynomial of *dt* we note the absence of *dt* in the amplitude method. This is due to our mistake assumption in constructing the exponential dependence,that the survival probability changes entirely due to transitions out of the initial state where we have not taken in account transitions back to the initial state. The latter would cancel the $-\Gamma dt$ term.

On the other hand eq. (52) together with (31) serve as a tool for the calculation of the angle *δ(E)* that enters the Lorentzian distribution and takes in account the energy dependence of the complex energy shift. Indeed we get the transcendental equation

$$\frac{\langle E\rangle\tau_d}{C(\beta)} + \beta\tan^{-1}\beta + \ln\left(\cos\tan^{-1}\beta\right) \cong \beta\delta + \ln\cos\delta \tag{54}$$

We can now discuss the finiteness of the time derivative of the survival amplitude. In fact we can divide the physical systems in two categories: these where the expecta-tion value of the energy is finite and these where it tends to infinite. Concerning the first case, we have already shown that when the expectation value of the energy is finite then the decay rate approaches zero as $t \to 0$.The time derivative of the amplitude expresses the rate with which the measuring perturbation should change in time in order for the non exponential decay to be observed. Combining the above we are left with the conclusion that in this case we can follow the system at sufficie-ntly small time and observe deviations from exponential propagation. But deviations from exponential decay are equivalent to say that at *t=0* the decay rate tends to zero and not equal to *–Γ*. Thus, if the unstable system is monitored for its existence at sufficiently small intervals of time, it would appear to be longer lived than if it were monitored at intermediate intervals, where the decay law is exponential. These are the conditions for the quantum Zeno's

paradox to appear, which states that in the limit of continuous monitoring the system does not decay at all. The quantum Zeno effect was first understood by von Neumann, [50]. While analyzing the thermodyna-mic features of quantum ensembles von Neumann proved that any given state Φ_O of a quantum mechanical system can be "steered" into other state Ψ of the same Hilbert space, by performing a series of very frequent measurements. If Φ_O and Ψ coincide, the evolution is frozen, meaning that a quantum Zeno effect takes place. The classi-cal allusion to the sophist philosopher Zeno of Elea is due to Misra and Sudarshan [30], who were also the first to provide a consistent and rigorous mathematical framework. We can easily see that if the system is initially prepared in the unstable state $|\Phi_O\rangle$ and is monitored on its survival at the instants *0, t/n, 2t/n,….,(n-1)t/n, t* the probability for its survival is given by $P(t/n)^n$. In addition since the survival amplitude is differentiable and $\dot{P}(0)=0$, we can actually write for $n\to\infty$.

$$\{P(t/n)\}^n \cong \{P(0)+\dot{P}(0)(t/n)\}^n = 1 \tag{55}$$

independent of *t*. It is thus evident that the survival probability under discrete but frequent monitoring will be close to 1 provided that *t/n* is sufficiently small to observe departures from exponential decay law. The quantum Zeno effect is a direct consequence of general features of the Schrödinger equation that yield quadratic behavior of the survival probability at short times. Let *H* be the total Hamiltonian of a quantum system and Φ_O its initial state. The short time expansion of the survival probability yields a quadratic behavior of the form

$$P(t):\ 1-t^2/\tau_z^2 \qquad \text{where} \qquad 1/\tau_z^2 \equiv \langle\Phi_O|H^2|\Phi_O\rangle - \langle\Phi_O|H|\Phi_O\rangle^2 \tag{56}$$

and τ_z is the Zeno time, **[51]**. It is easy to see that $\{P(t/n)\}^n \cong \exp\left(-t^2/n\tau_z^2\right)\to 1\ (as\ \mathrm{n}\to\infty)$. If the Hamiltonian is divided into the unperturbed H_O and the interaction part H_{int} , the Zeno time reads

$$1/\tau_z^2 \equiv \langle\Phi_O|H_{\mathrm{int}}{}^2|\Phi_O\rangle = e\ddot{s}_{t<<}(0) \tag{57}$$

which in accordance to eq. (48) gives

$$1/\tau_z^2 \cong \frac{1}{2\tau_d^2}\left[\frac{\mathrm{sech}(\ln\beta)}{4}-N(\beta,\delta)\right]\mathrm{x}$$
$$\left[\left(\tan^{-1}\beta-\delta\right)\left(1-\beta^2\right)-2\beta\ln\frac{\cos\tan^{-1}\beta}{\cos\delta}+\tan\delta-\beta\right] \tag{58}$$

In this way we can estimate the Zeno time as

$$\tau_z \cong \frac{2\sqrt{2}\tau_d}{\sqrt{\mathrm{sech}(\ln\beta)-4N(\beta,\delta)}}\left[\left(\tan^{-1}\beta-\delta\right)\left(1-\beta^2\right)-2\beta\ln\frac{\cos\tan^{-1}\beta}{\cos\delta}+\tan\delta-\beta\right]^{-1/2} \tag{59}$$

Since the finiteness of the time derivative of the survival amplitude at *t=0* turns to be very important for the process of measurement, we may want to investigate its limits of accuracy as these are determined from eq. (52). Due to the structure of the *C(β)* coefficient $\dot{a}(0)$ is expected to have at least two roots, meaning the values of β_1 and β_2 that were previously revealed. This is important because these roots correspond to regions of quantity β where $\dot{a}(0)$ remains finite. We remind ourselves that these regions include resonant states where the non exponential

decay dominates over the exponential, and according to the above quantum Zeno's paradox may appear. On the other hand eq. (52) describes the rate with which the measurement matrix element should change in the limit of very short times in order for the non exponential decay to be observed, as a function of the angle *δ(E)*. When the latter is close to π/2 then the complex energy shift does not significantly depend on the energy and the spectral distribution is almost Lorentzian line shape. For this reason we examine $\dot{a}(0)$ for different values of *δ(E)* close and distant from π/2, from π/1.985 to π/1.500. The figures that follow describe $\dot{a}(0)$ with *β*, for the previously mentioned values of the angle *δ*, covering each time two different regions of values of *β*.

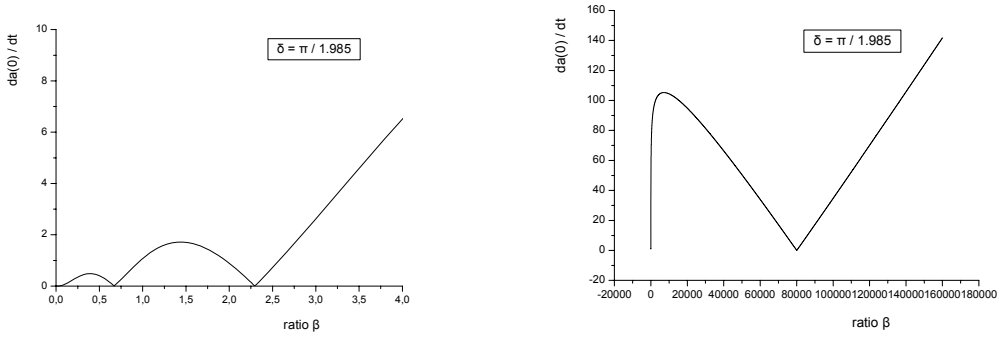

(a) (b)

FIGURE 2. The variation of $\dot{a}(0)$ with *β* for an angle *δ = π/1.985*. a) For small values of *β* we have the two minima generated by *C(β)*, b) a third minimum appears for a value of *β* equal to 80x10^3. For greater values of *β*, $\dot{a}(0)$ approaches ∞.

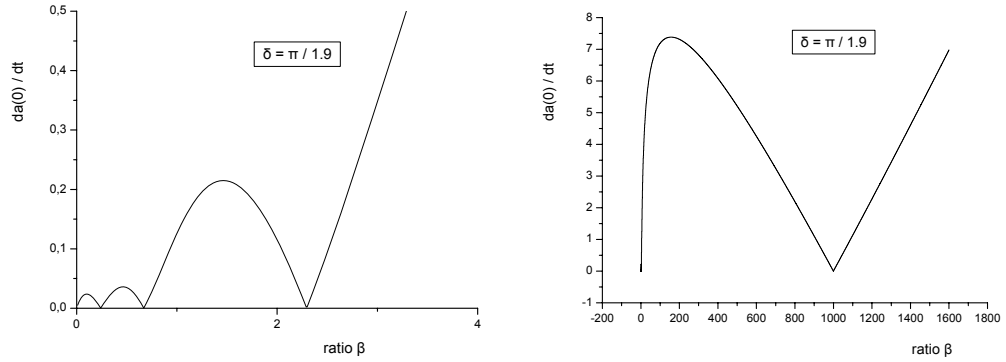

(a) (b)

FIGURE 3. The variation of $\dot{a}(0)$ with *β* for an angle *δ = π/1.9*. a) For small values of *β* we have three minima, b) a fourth minimum appears for a value of *β* equal to 10^3. For greater values of *β*, $\dot{a}(0)$ approaches ∞.

The existence of minima in the above figures, ensures the finiteness of the time derivative of the survival amplitude, and enables the observation of the non exponential decay and generally the delay of propagation out of the initial state. We can see that when the angle δ is close to π/2 minima appear not only due to the structure of $C(\beta)$ for small values of β, but for other values of β as well. This corresponds to the case where the Lorentzian line shape distribution provides a good approximation for the description of the unstable state. When δ further changes, there is no more space for other minima and $\dot{a}(0)$ approaches infinite as β grows. Thus the rate with which the measuring process varies tends to infinite even if the matrix element of the process is itself finite. In this way the variation of the measuring perturbation is discontinuous and we can not follow the system in this limit although the measurement might be in principle realizable.

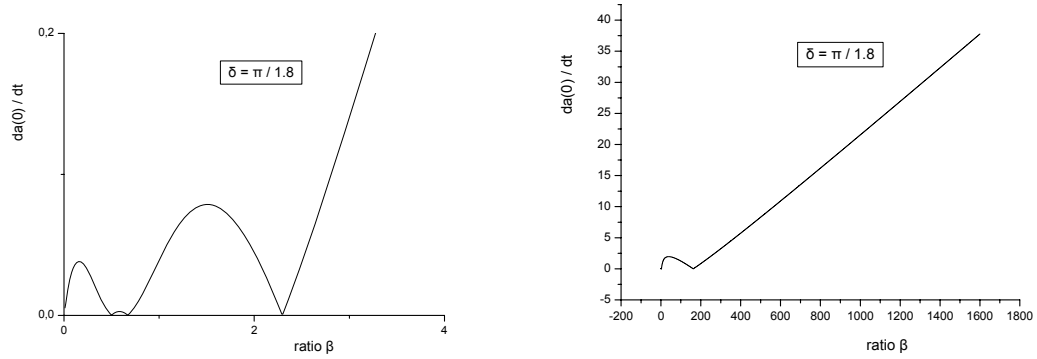

(a) (b)

FIGURE 4. The variation of $\dot{a}(0)$ with β for an angle $\delta = \pi/1.8$. a) For small values of β we have tho minima, since the third is getting absorbed b) a third minimum appears for a value of β equal to 180. For greater values of β, $\dot{a}(0)$ approaches ∞.

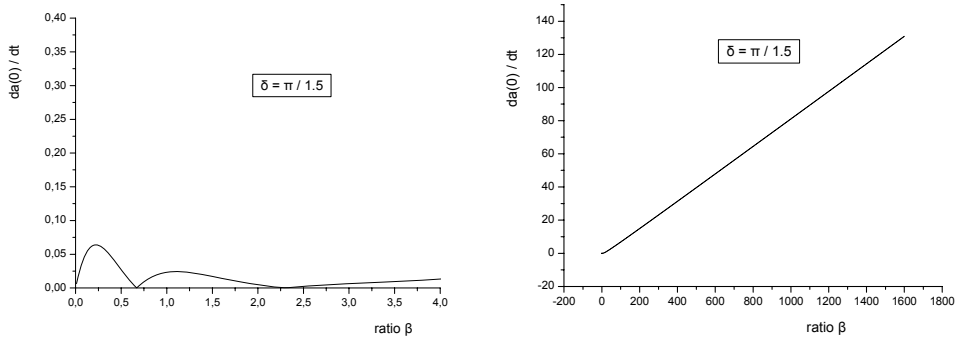

(a) (b)

FIGURE 5. The variation of $\dot{a}(0)$ with β for an angle $\delta = \pi/1.5$. a) For small values of β we have again the two minima generated by $C(\beta)$, b) no other minimum appears for greater va-lues of β since the previous corresponding minimum is absorbed, and $\dot{a}(0)$ linearly approaches ∞.

When we treat the case of a strongly energy dependent energy shift, we can see from (46) that the rate with which the measuring perturbation changes, remains very small in magnitude for all the moments in time and also purely imaginary. The small magnitude has to do with the

fact that in this case the non exponential decay domi-nates the propagation in the limits of very short times, due to the strong contribution of the angle *δ(E)*, [13,46], and so it is possible for the detector to follow the system and observe it. We have already seen that the *est* acquires a purely imaginary struc-ture for two reasons: $\mu(t)$ is the part of the Hamiltonian that causes the measuring perturbation of the system at *t=0* and in addition we can assume that the system can indeed be prepared in the state $|\Phi_o\rangle$ at that instant. Since the $est = \dot{a}(t)$ conserves this imaginary structure at later times also, it is clear that this is equivalent to say that we can repeatedly reset the system to its initial state. In this way we can in principle observe the non exponential decay and at the same time prevent decay by resetting the system back to Φ_o through repetitive observations, with a rate of change of the measuring process given by (46). Thinking so, (46) could serve as a definition for the frequency of observation needed, where for a wide class of systems, tests of nonde-cay repeated at arbitrarily small times would prevent the decay of an unstable state. Again this is not true for the complex spectral distribution for the same reasons explained in the previous paragraph.

Finally we may discuss the limit of very long times. As we have already mentioned the Paley-Wiener theorem [44], states that if the spectrum of the Hamiltonian is bounded below, so that $\rho(E) = 0 \text{ for } E < 0$, then the survival amplitude decreases to 0 as $t \to \infty$ less rapidly than any exponential function. This is essentially Khalfin's argument [8] proving the necessity of deviation from the exponential decay law at large time. Looking at eq. (47) it is easy to understand that all stochastic terms containing $\exp\left(i\omega(\beta,\delta)t\right)$ produce cancellations and so the dominant term for *n=0* takes the following form for the two distributions

$$EST^{R,C}{}_{t>} \cong \frac{iN(\beta)C(\beta)\tau_d}{(1+i\beta)[(i\beta,2)-1]} \cdot \frac{1}{t^2} \tag{56}$$

Both terms rapidly go to zero as time grows, which makes it quite easy for the non exponential decay to be observed in this region of time. However and as we have already mentioned at the beginning of this section, a serious problem to be solved experimentally has mostly to do with the very small magnitude of the propagation at this region of time.

5. CONCLUDING REMARKS

In this work we discussed the origin and some of the properties of the deviations from exponential decay law, related to quantum resonances that can be described by Lorentzian line shape distributions. For this reason we first demonstrated the appearance of the Lorentzian distribution in both classical and quantum theory of resonances, as the mean amount of energy absorbed per unit time and the scattering phase respectively. In our study we distinguished two types of distributions both generated by the Lorentzian, namely the real truncated Lorentzian which is the semibounded Lorentzian, and the complex Lorentzian distribution which emerges when keeping only the appropriate *t>0* energy pole of the Lorentzian.

Following very general principles arising from kinematical effects, we showed that for large times and due to the fact that the decay products to whom the initial unstable state is finally distributed become uncorrelated, the kinematical factors dominate the distribution, giving a non exponential time dependence of the form $t^{-3/2}$. In the limit of very short times it is important to notice that the magnitude of the survival amplitude approaches the energy expectation value and the amplitude itself is purely imaginary. Then both the semiboundness of the spectrum and the finiteness of the expectation value of the energy, ensure that the time derivative of the

survival probability approaches zero. Thus, at sufficient small time, the non decay probability falls off less rapidly than would be expected on the basis of the exponential decay law.

We constructed an analogous to the continuity equation in order to investigate the correlation between exponential and non exponential decay. We defined a spatial variable β, as twice the ratio of the energy position to the width function of the reso-nance and showed that there is an one by one correspondence between the strength of the exponential decay and this ratio. We can achieve the homogeneity of this equ-ation by applying a suitable measuring perturbation cancelling its second part, where the latter is defined as the exponential source term, *est*. The *est* expresses the corre-lation between exponential and non exponential decay and comes as the first time derivative of the previously mentioned measuring perturbation. For both types of distributions we found the same values of β close to 1 that zero the *est*, correspo-nding to the situation where the non exponential decay dominates the evolution. In the limit of short times we proved that the complex spectral distribution does not provide a complete theory for the observability of the non exponential decay, since it does not construct a purely imaginary survival amplitude as it should. Concerning the real distribution in the above limit, we produced the transcendental eq. (54) for the angle δ that describes the energy dependence of the complex energy shift as a function of the expectation value of the energy of the initial state. We also produced eq. (59) that gives the Zeno time as a function of the ratio β. We explored the finite-ness of the *est* term for other values of β as well, beyond those close to 1, since this permits someone to follow the system and observe the non exponential propagation, at least in principle. We showed that the finiteness is achieved only for specific valu-es of the angle δ close το π/2. For the case of a strongly energy dependent energy shift we found that the rate with which the measuring perturbation should change, is very small in magnitude for all the moments in time and also purely imaginary, conce-rning the real spectral distribution. The first characteristic was connected to the strong contribution of the non exponential decay while the second was connected to the potentiality to repeatedly reset the system to its initial state. In this way equation (46) provides information for the frequency needed for the repetition of the observa-tions. However this is not true for the complex spectral distribution, for the same reasons appeared in the short time regime.

In the limit of very long times both distributions produce *ests* whose dominant terms, meaning those beyond the stochastic terms that cancel each other, rapidly go to zero with time as $1/t^2$. This fact makes it quite easy for the non exponential decay to be observed. However the difficulty in this case has mostly to do with the very small magnitude of the propagation at this region of time.

REFERENCES

1. G. Gamow, *Z. Phys.* **51**, 204-212 (1928).
2. P.A.M. Dirac, *Proc. Roy. Soc. London* **114**, 243-265 (1927).
3. V.F. Weisskopf and E.P. Wigner, *Z. Phys.* **63**, 54-73 (1930).
4. G. Breit and E.P. Wigner, *Phys. Rev.* **49**, 519-531 (1936).
5. A.J.F. Siegert, *Phys. Rev.* **56,** 750-752 (1939).
6. J. Wheeler, *Phys. Rev.* **52,** 1107-1122 (1937).
7. M. L. Goldberger and K. M. Watson, *Collision Theory*, New York: Wiley, 1964, pp. 424-509.
8. L. A. Khalfin, *J Exp. Theor. Phys.* **6**, 1053-1063 (1958).
9. L. Fonda, G.C. Chirardi and A. Rimini, *Rep. Prog. Phys.* **41**, 587-631 (1978).
10. C. C. Tannoudji, J. D. Roc and G. Grynberg, *Atom-Photon Interactions,* New York: Wiley,1992, pp. 189-195
11. T. Petrosky and I. Prigogine, *Comp. Math. Appl.,* **34**, 1-44 (1997).
12. V. Wong and M. Gruebele, *Phys. Rev. A* **63**, 022502 1-9 (2001).
13. T. G. Douvropoulos and C. A. Nicolaides, *Phys. Rev. A* **64**, 032105 1-10 (2004).

14. P. Facchi and S. Pascazio, S., *Phys. Lett. A*, **241**, 139-144 (1998).
15. F. Giacosa and G. Pagliara, *Mod. Phys. Lett. A* **26** 2247-2259 (2011).
16. F.H.L. Coppens, et al., *Phys. Rev. Lett.*, **99**, 106803 1-4 (2007).
17. P.J. Aston, *Eur. Phys. Lett.*, **97**, 5201-6 (2012)
18. F. Giacosa, *Found. Phys.*, **42**, 1262-1299 (2012).
19. J.G. Muga, F. Delgado, A del Campo, et al., *Phys. Rev. A*, **73**, 052112 1-5 (2006).
20. J. Martorell ,J.G. Muga and D.W.L. Sprung, *Rev. A*, **77**, 042719 1-9 (2008).
21. Y. J. Wang, S. J. Xu, D. J. Zhao, et al, , *Opt. Express,* **14**, 13151-13157 (2006).
22. J. P. Boon and S. Yip, *Molecular Hydrodynamics*, New York: Dover, 1991, pp. 120-129.
23. K. Zhang, *J.Appl.Phys.*, **105**, 07D307 1-3, (2009).
24. E. Grunewald, R. Knight, *Geophysics*, **77**, EN1-EN9 (2011).
25. P. Ginzburg, A. Zayats, *Opt. Express.*, **20**, 6720-6727 (2012).
26. V. Uc. Hugo, J. P. Alvarez-Idaboy, A. Galano and A. Vivier-Bunge, *J. Phys. Chem. A*, **112**, 7608-7615 (2008).
27. G. Kalosakas, K. O. Rasmussen and A. R. Bishop, *Chem. Phys. Lett.*, **432**, 291-295 (2007).
28. B. Yegnanarayana, B. S. Ramaksrishna, *J. Acoust. Soc. Am.*, **58**, 853-857 (1975).
29. J. A. D. Appleby, A. Rodkina and H. Schurz, *Discrete Cont. Dyn.-B*, **6**, 667-696 (2006).
30. B. Misra and E. C. G. Sudarshan, *J. Math. Phys.*, **18**, 756-763 (1977).
31. C. B. Chiu, E. C. G. Sudarshan and B. Misra, *Phys. Rev. D*, **16**, 520-529 (1977).
32. L.D. Landau, E.M. Lifshitz and L.P. Pitaevskii, *Electrodynamics of Continuous Media*, 2nd edition, Oxford: Butterworth Heinemann,, 1984, pp. 428-432.
33. M. Razavy, *Classical and Quantum Dissipative Systems*, 4th edition, New York: World Scientific, 2002, pp. 544-545.
34. J. Mehra and E.C.G. Sudarshan, *Nuovo Cimento,* **11B**, 215- 256 (1972).
35. A. Bohm, N. L. Harshman and H. Walther, *Phys. Rev. A*, **66**, 012107 1-11 (2002).
36. B. Erman, *Biophys. J.*, 91, 3589-3599 (2006).
37. S. N. Shore, T. N. LaRosa, R. J. Chastain and L. Magnani, *Astron. Astrophys.,* 457, 197-206 (2006).
38. N. Rubab and G. Murtaza, *Phys. Scripta,* 74, 145-148 (2006).
39. K. K. Lehmann, *J. Chem..Phys.*, **126,** 024108 1-4 (2007).
40. J. Y. Jo et al., *Phys. Rev. Lett.*, 99, 267602 1-4 (2007).
41. B. Basu, *Phys. Plasmas*, **15,** 042108 1-17 (2008).
42. H. Blom and G. Bjork, *Appl. Optics,* **48,** 6050-6058 (2009).
43. L. F. Lafuerza, P. Colet and R. Toral, *Phys. Rev. Lett.*, 105, 084101 1-4 (2010).
44. R. Paley and N. Wiener, *Fourier transform in complex domain*,Rhode Island: American Mathematical Society, Providence, 1934, Theorem XII, pp. 18
45. F. Reif, *Fundamentals of Statistical and Thermal Physics*, London: McGraw-Hill, 1965, pp. 560-565
46. E. J. Robinson, *Phys. Rev. Lett.*, **52**, 2309-2312 (1984).
47. U. Fano, *Phys. Rev.,* **124**, 1866-1878 (1961).
48. T. G. Douvropoulos, *Int. J. Quantum Chem.,* **107**, 1673-1687 (2007).
49. L. D. Landau and E. M. Lifshitz, *Course of Theoretical Physics: Fluid Mechanics*, 2nd edition, Oxford: Butterworth Heinemann, 1998, pp. 1-2.
50. J.V. Neumann, *Mathematical Foundations of Quantum Mechanics,*Princeton New Jersey: Princeton University Press,1955 pp.366-367.
51. P. Facchi, V. Gorini, G. Marno, S. Pascazio and E.C.G. Sudarshan, *Phys. Lett. A,* **275**, 12-19 (2000)